Blessed Plots for the 2010 CC analysis

J. Evans, K. Lang and R. Nichol
for the CC Group

April 3, 2011
(minos-doc-7359-v21)

Introduction

This document contains the blessed plots package for the 2010 CC PRL result.

This result will supersede the currently-public Neutrino 2010 result as soon as the PRL is submitted to the journal and on the archive. **None of these plots will be public until that happens.**

The changes between the Neutrino 2010 result and this PRL result are summarized in DocDB-6862 (the file PostAthensUpdate.pdf); the main change is the addition of the rock and anti-fiducial events into the analysis.

Numbers

The best reference for numbers is the PRL itself: DocDB-7703. The provenance of all numbers contained in the PRL is summarized in DocDB-7674.

In the fiducial, antifiducial and rock samples together, we observe 4003 events compared to an unoscillated prediction of 4657 in Runs I–III of the LE and pHE beams.

The headline numbers are as follows:

Exposure: 7.25×10^{20} PoT (including pHE running)

Oscillation parameter measurement:

$|\Delta m^2| = 2.32^{+0.12}_{-0.08} \times 10^{-3}$ eV^2 (constrained to the physical region)

$\sin^2(2\theta) = 1.0$

$\sin^2(2\theta) > 0.90$ (90% C.L.)

$\sin^2(2\theta) > 0.94$ (68% C.L.)

Best fit systematics:

normalization $= 1.005$

neutral current background $= 1.053$

absolute shower energy $= -0.30\sigma$

muon track energy $= 0.08\sigma$

Pure neutrino decay is disfavoured at 7σ.

Pure neutrino decoherence is disfavoured at 9σ.

Beam and stability plots

minos-doc-6188

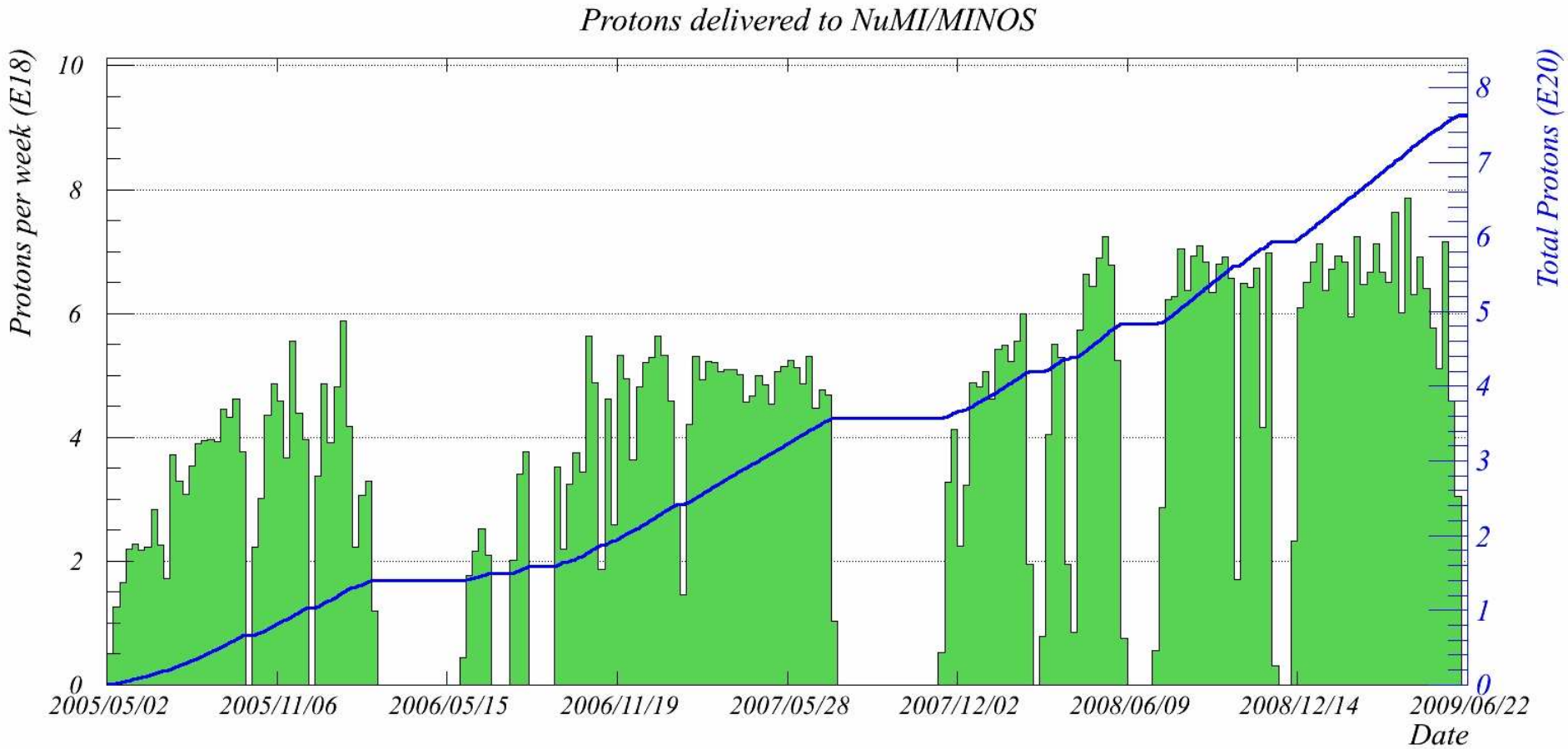

Figure 1: The protons delivered to the NuMI target are shown for Runs I-III. The protons delivered each week are shown in the green plot, and the total integrated protons delivered are shown by the blue line.

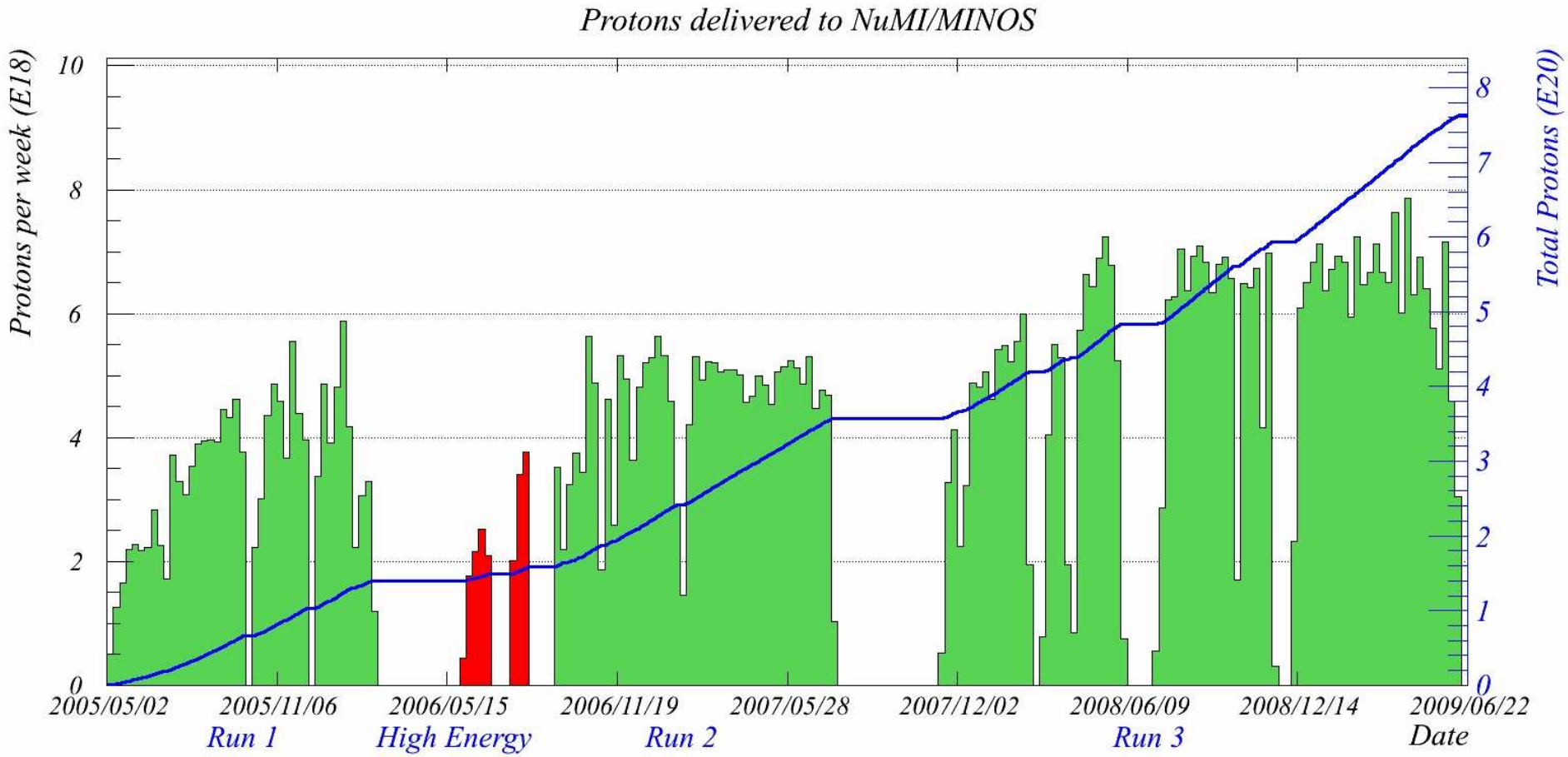

Figure 2: The protons delivered to the NuMI target are shown for Runs I-III. The protons delivered each week are shown in the green plot, and the total integrated protons delivered are shown by the blue line.

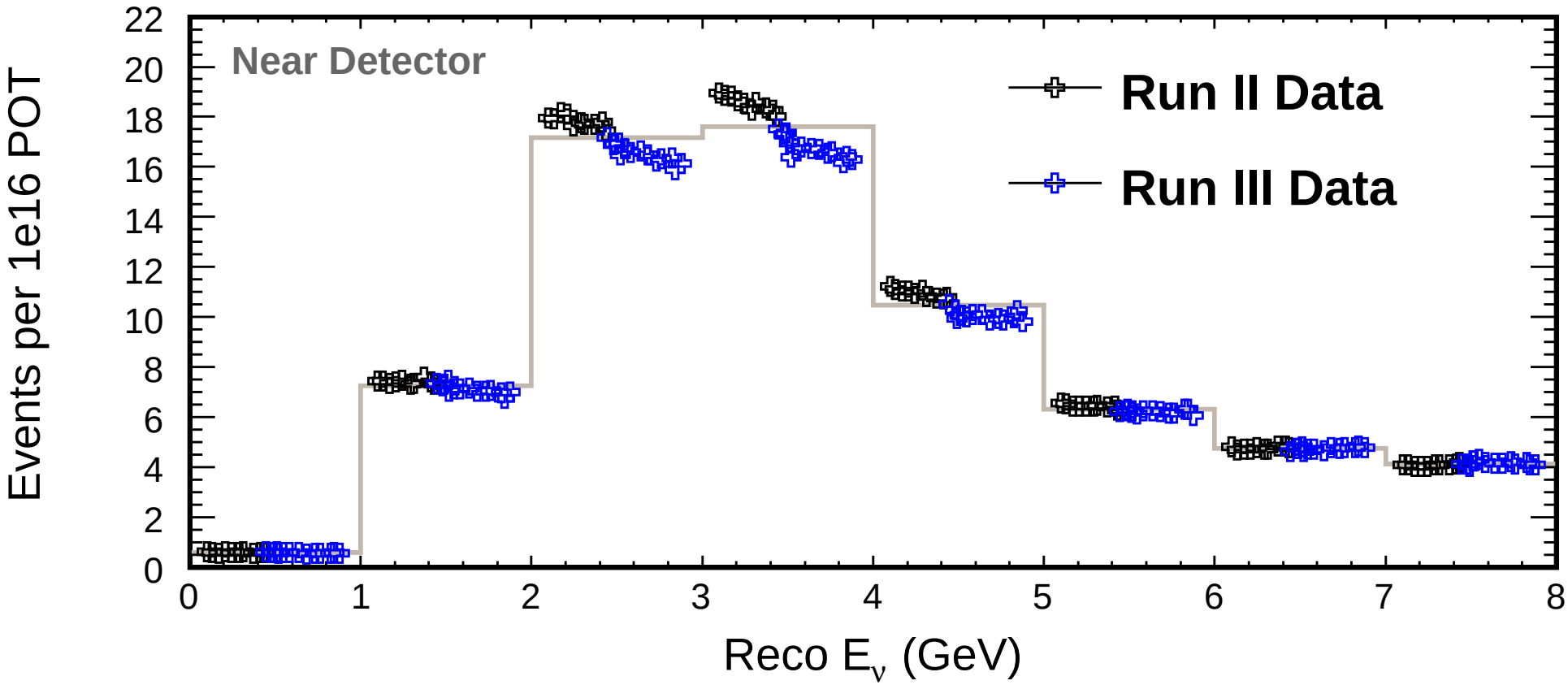

Figure 3: Reconstructed neutrino energy spectrum for data taken during Runs 2 (black) and 3 (blue). Each point corresponds to a specific period of data taking (see note for further details) and the points in each bin are plotted with a PoT-weighted spacing. the solid histogram shows the PoT-weighted average in each bin. It should be mentioned that some change is expected due to Helium in the decay pipe.

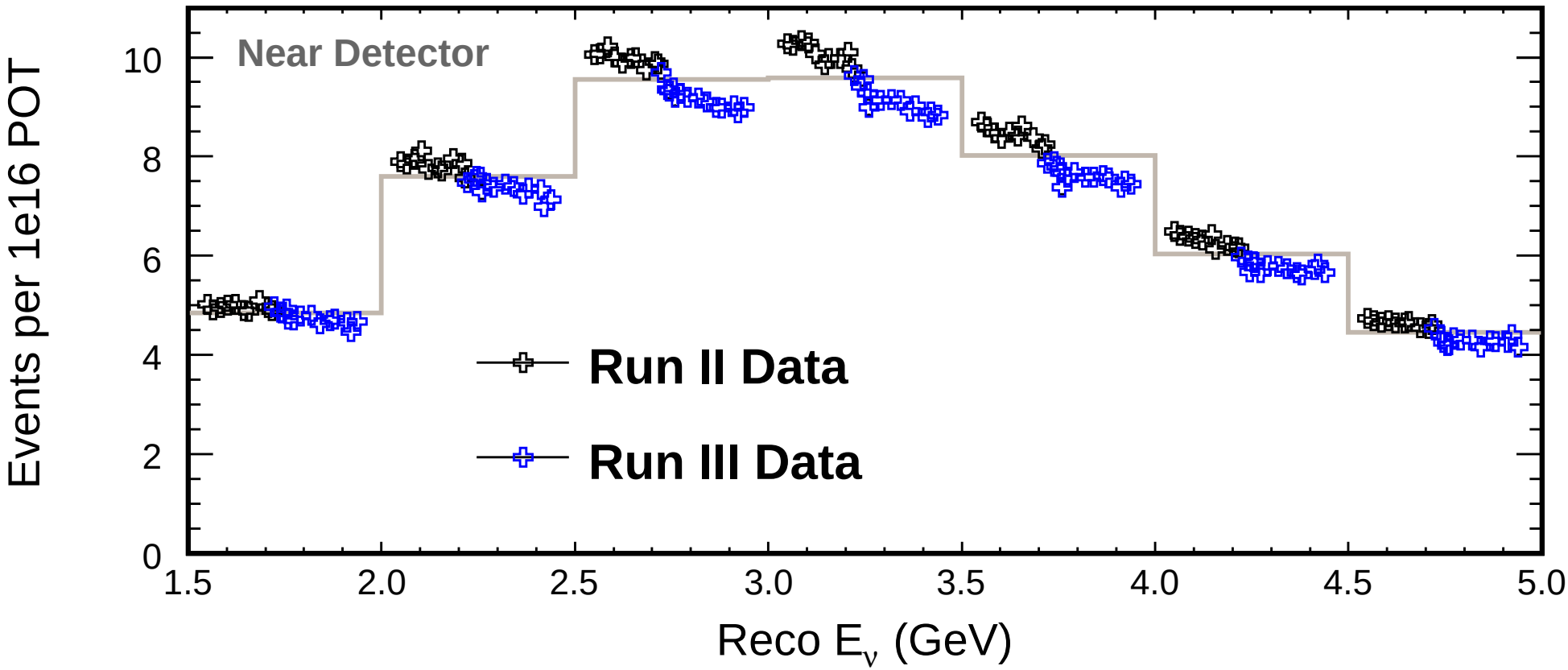

Figure 4: As the previous slide, but more finely binned and only showing the spectrum peak.

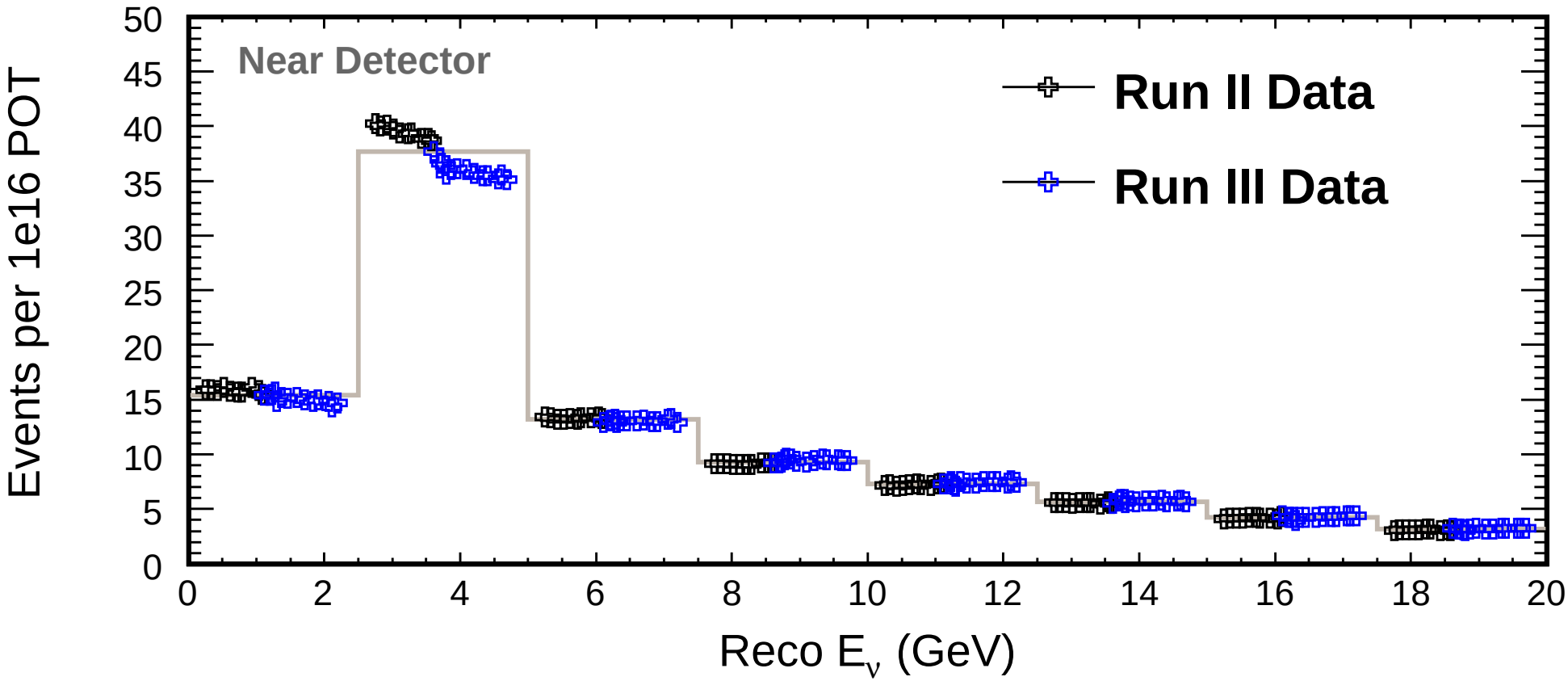

Figure 5: As the previous two slides, but more coarsely binned, and showing the spectrum up to 20 GeV.

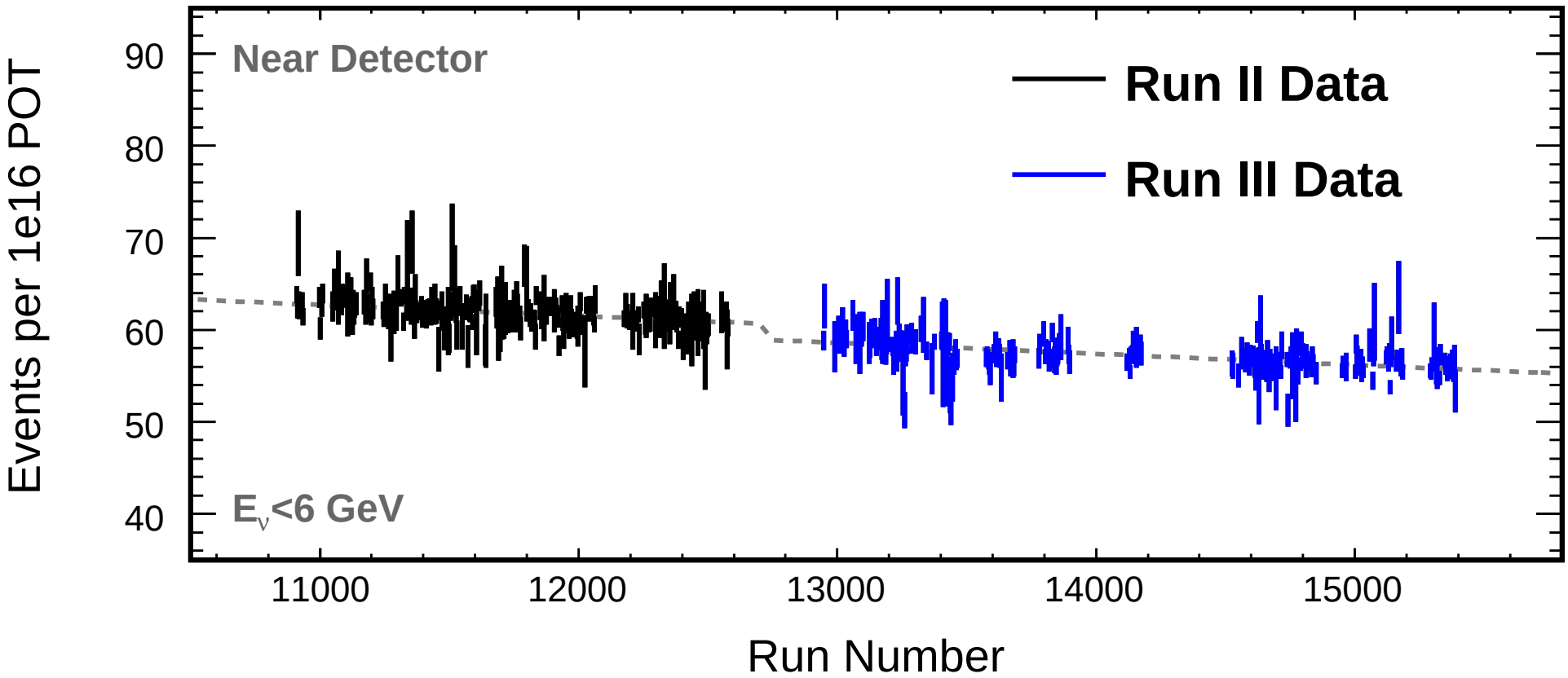

Figure 6: Numbers of reconstructed CC-like events per 1e16 PoT with reconstructed energy less than 6 GeV as a function of run number during runs 2 and 3. The dotted line shows a fit to a slope + step at the Run 2/3 boundary (due to the addition of helium to the decay pipe). For presentational purposes, only runs with $> 2.5 \times 10^{17}$ PoT (in total) are displayed on the figure.

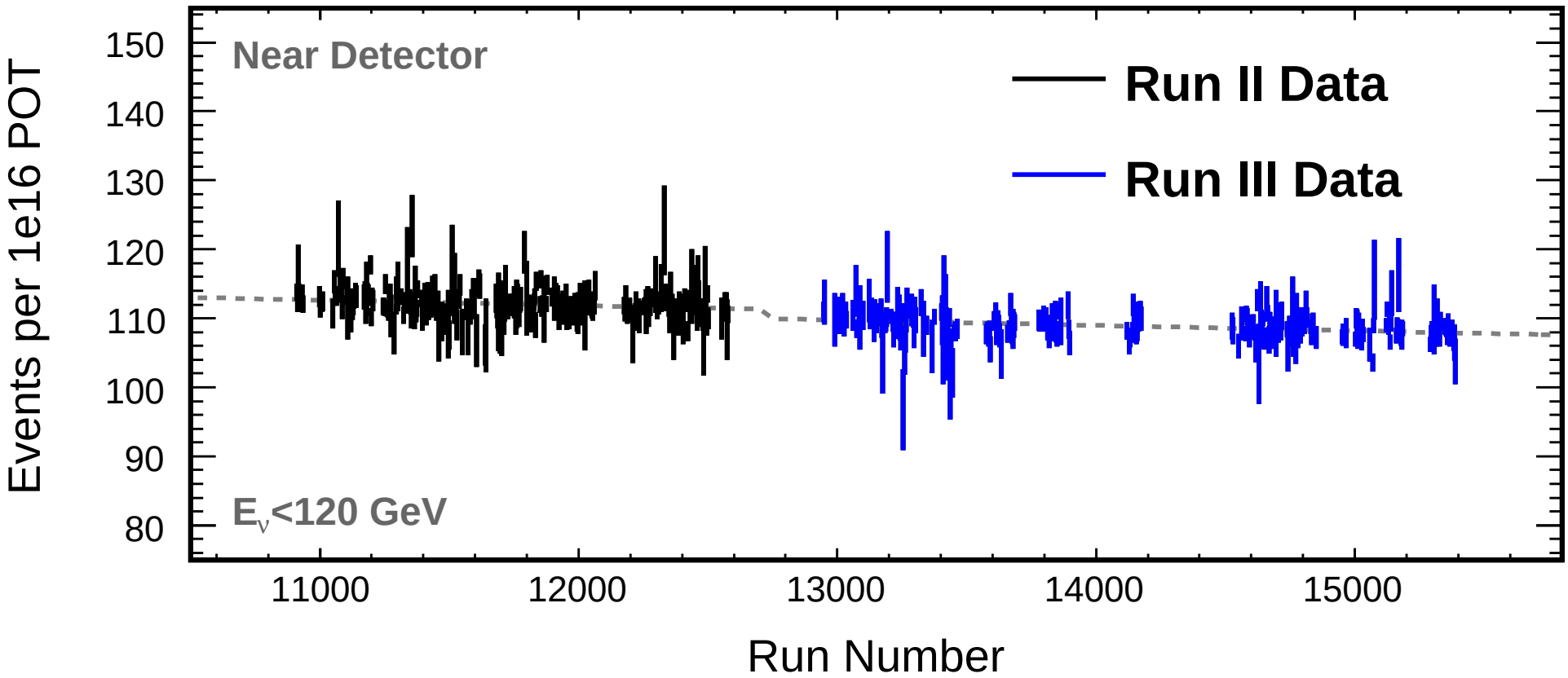

Figure 7: As the previous slide, but showing all events.

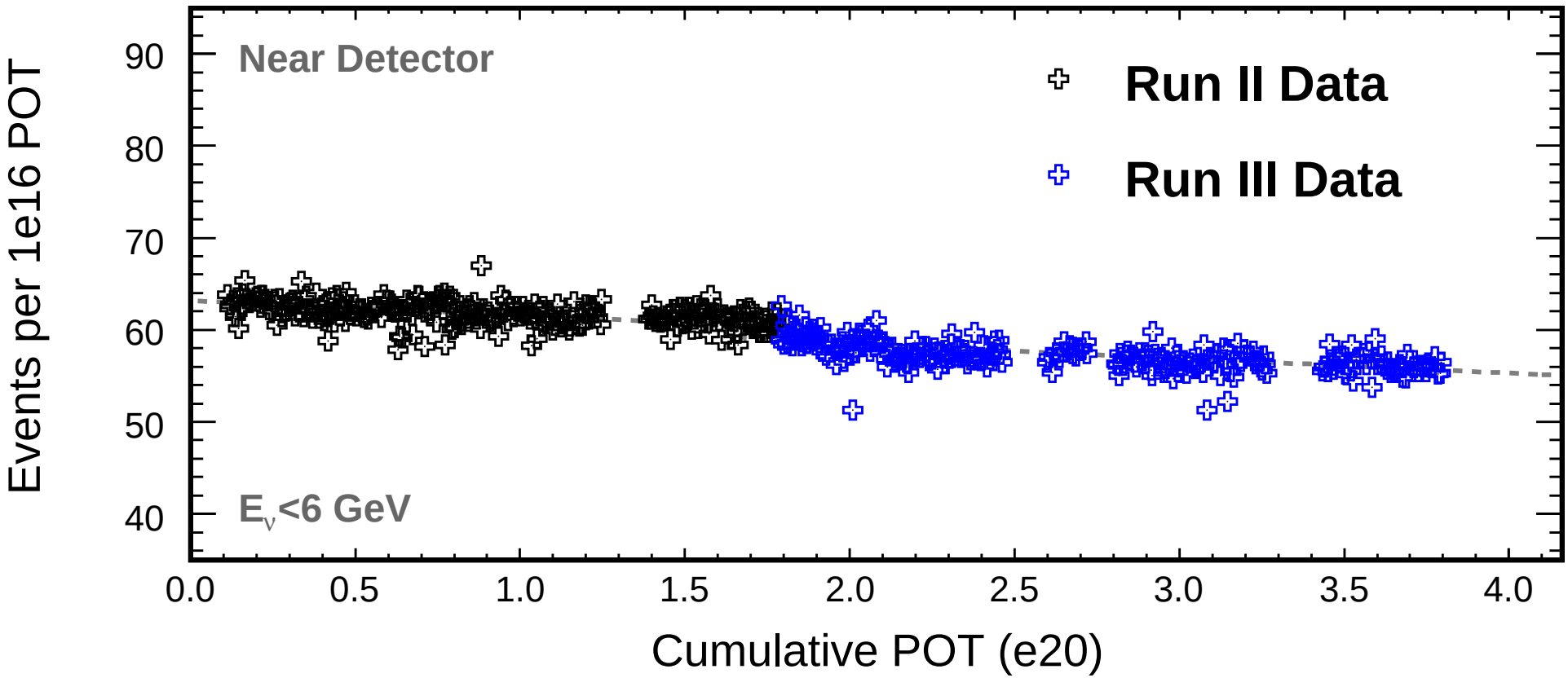

Figure 8: Numbers of reconstructed CC-like events per 1e16 PoT as a function of cumulative PoT during Runs 2 and 3 — this corresponds to data taken with NT02 up until the end of December 2008. The dotted line shows a fit to a slope + step at the Run 2/3 boundar. A point is plotted for each run containing a total of more than 1e18 PoT, although all runs are considered when calculating the cumulative PoT.

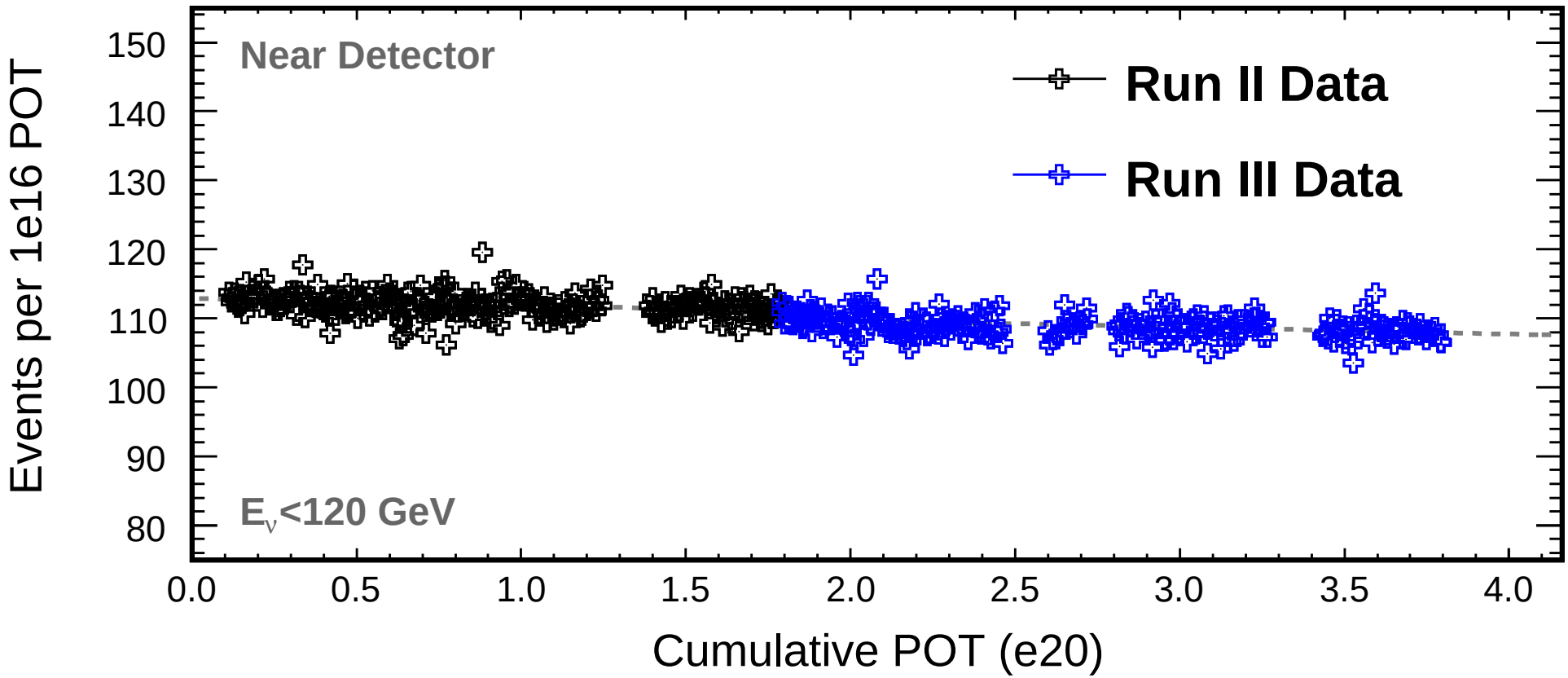

Figure 9: As previous slide, here showing events of all energies.

Fiducial sample — effi ciency and purity

minos-doc-7116

Efficiency and purity

At the far detector (unoscillated), integrated over all energies:

Efficiency: 88.7%
Purity: 98.3%

This compares to the numbers for the 2008 PID (run on dogwood):

Efficiency: 86.5% Purity: 98.8%

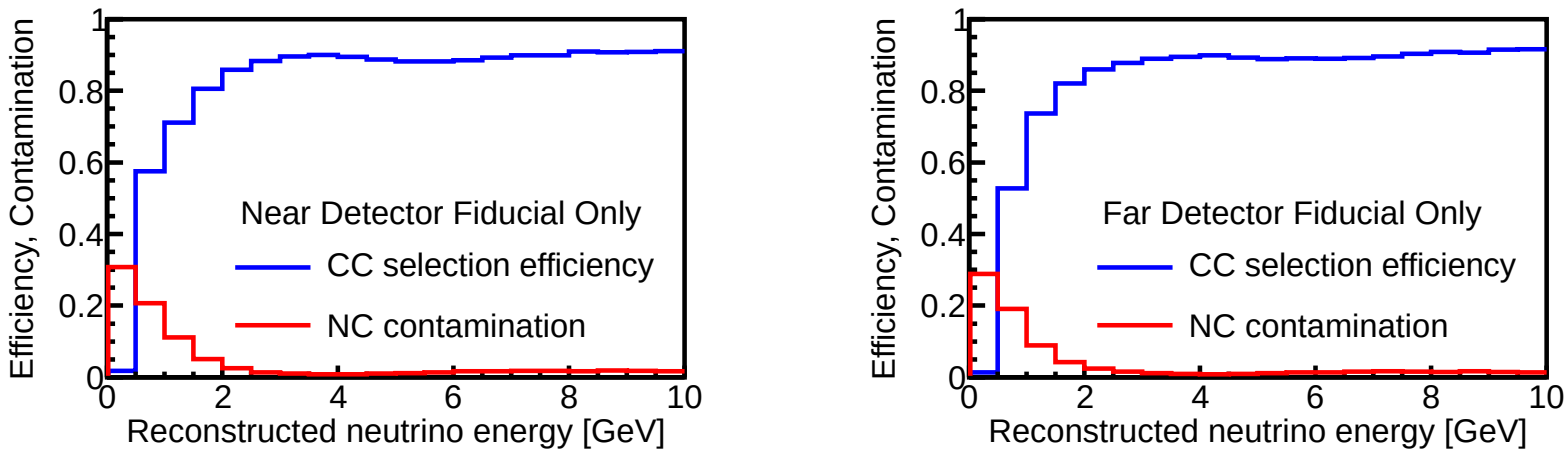

Figure 10: Efficiency and purity predicted by Monte Carlo at the MINOS Near (left) and Far (right) Detectors. The Far Detector case assumes no oscillations.

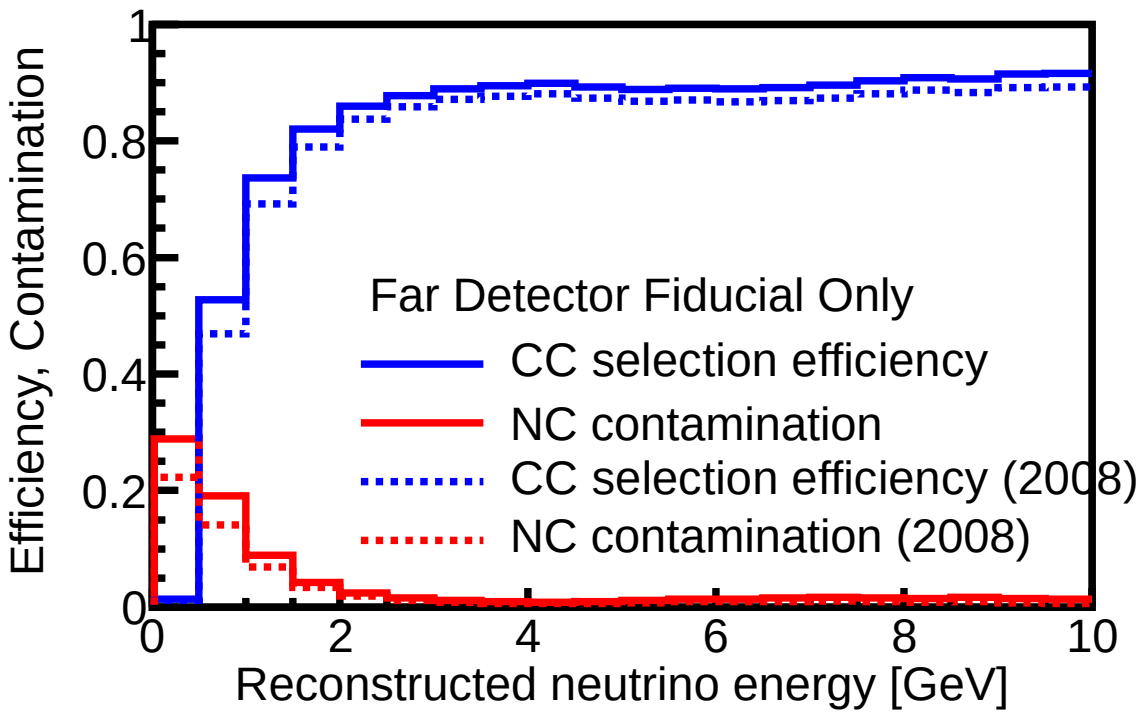

Figure 11: The Efficiency and Purity for the 2008 and 2010 selections using the same preselection

Near detector PID plots

minos-doc-7002

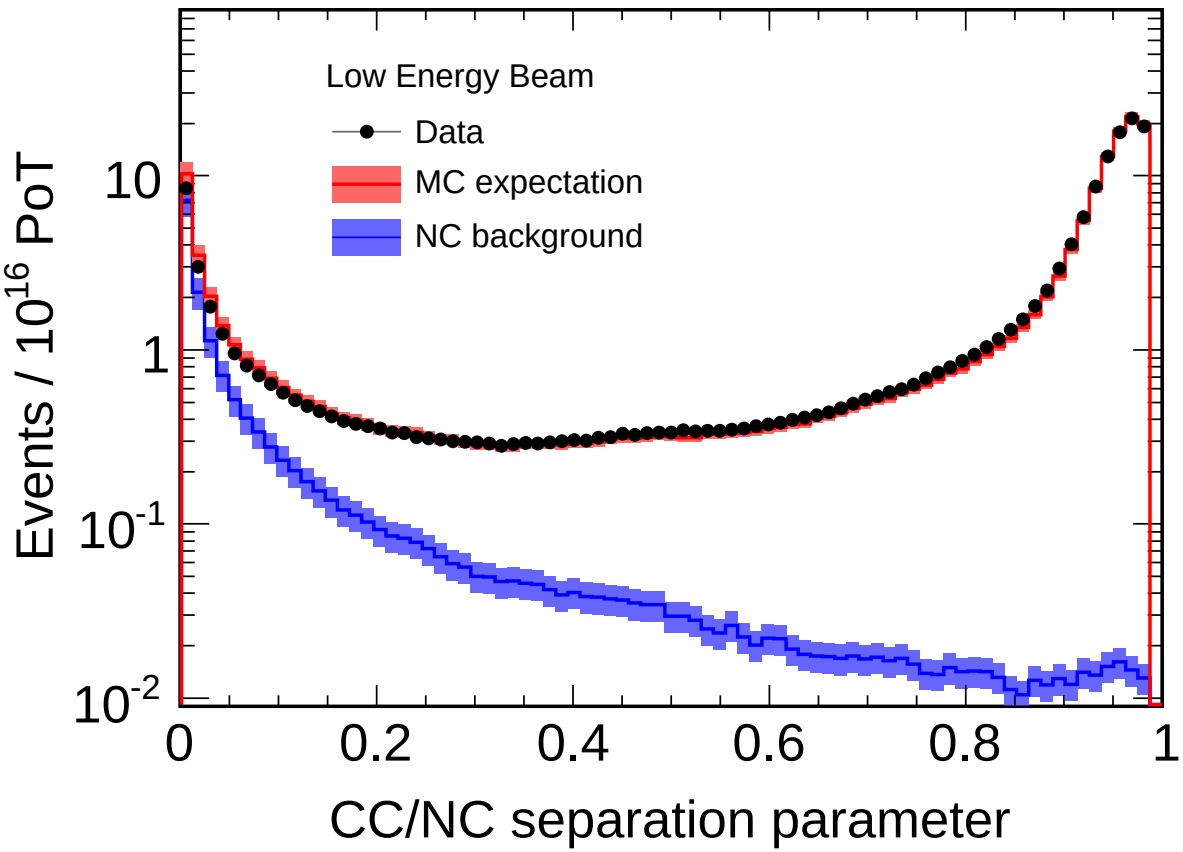

Figure 12: ND LE Data/MC Comparison: RO PID Variable.

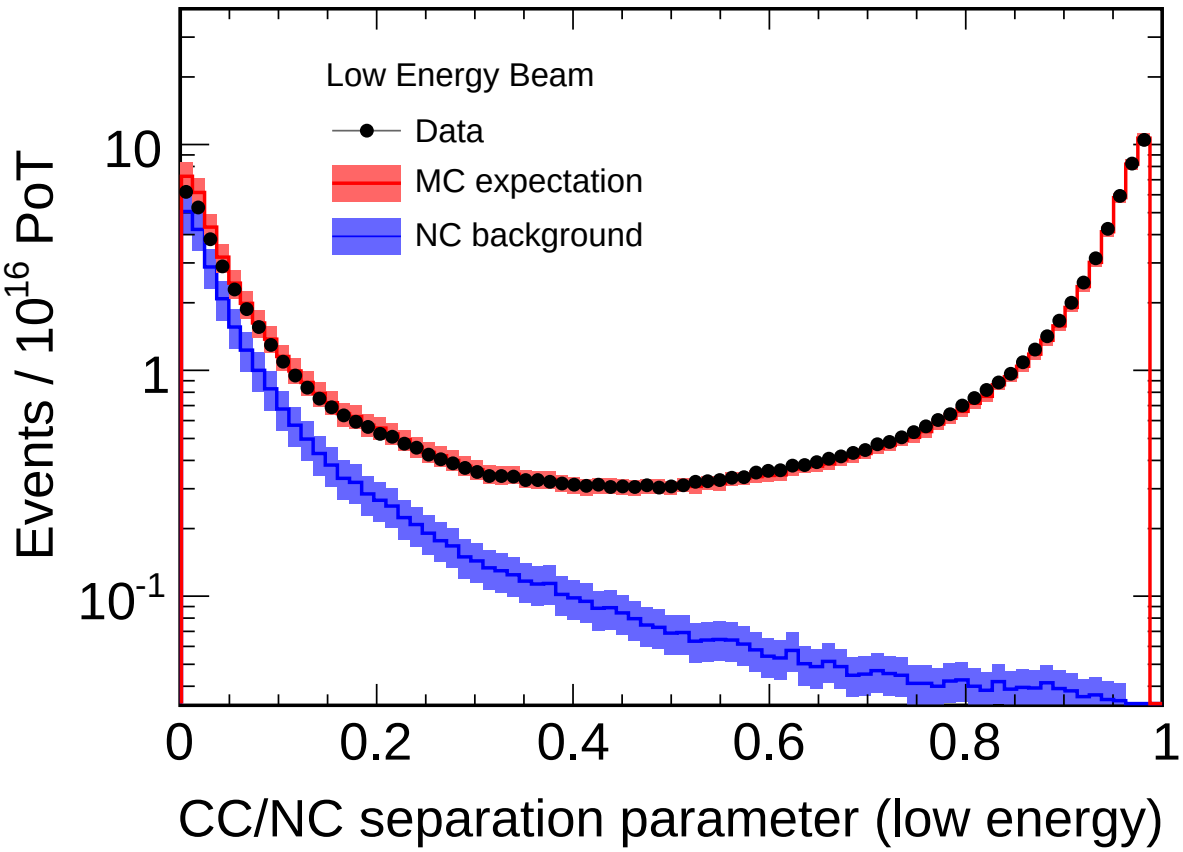

Figure 13: ND LE Data/MC Comparison: JM PID Variable.

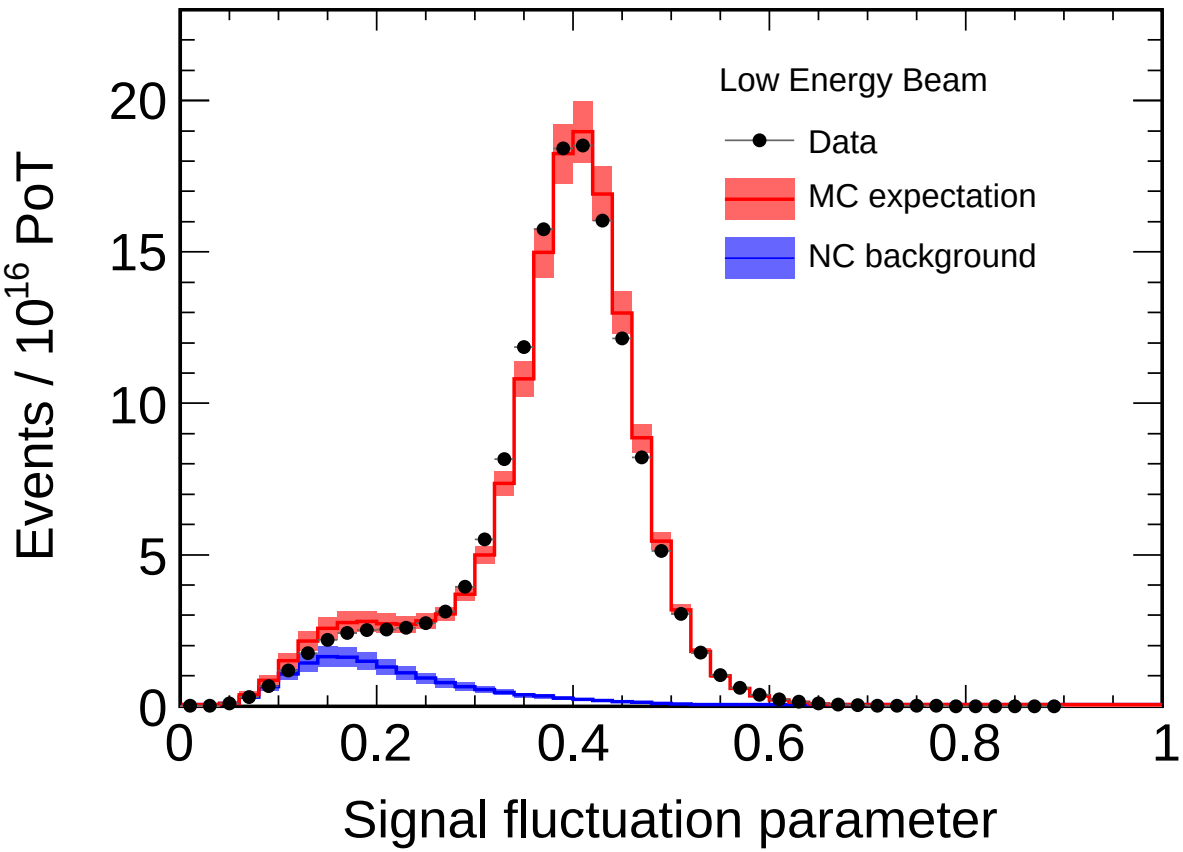

Figure 14: ND LE Data/MC Comparison: RO PID Input Variable, Signal Fluctuation Parameter.

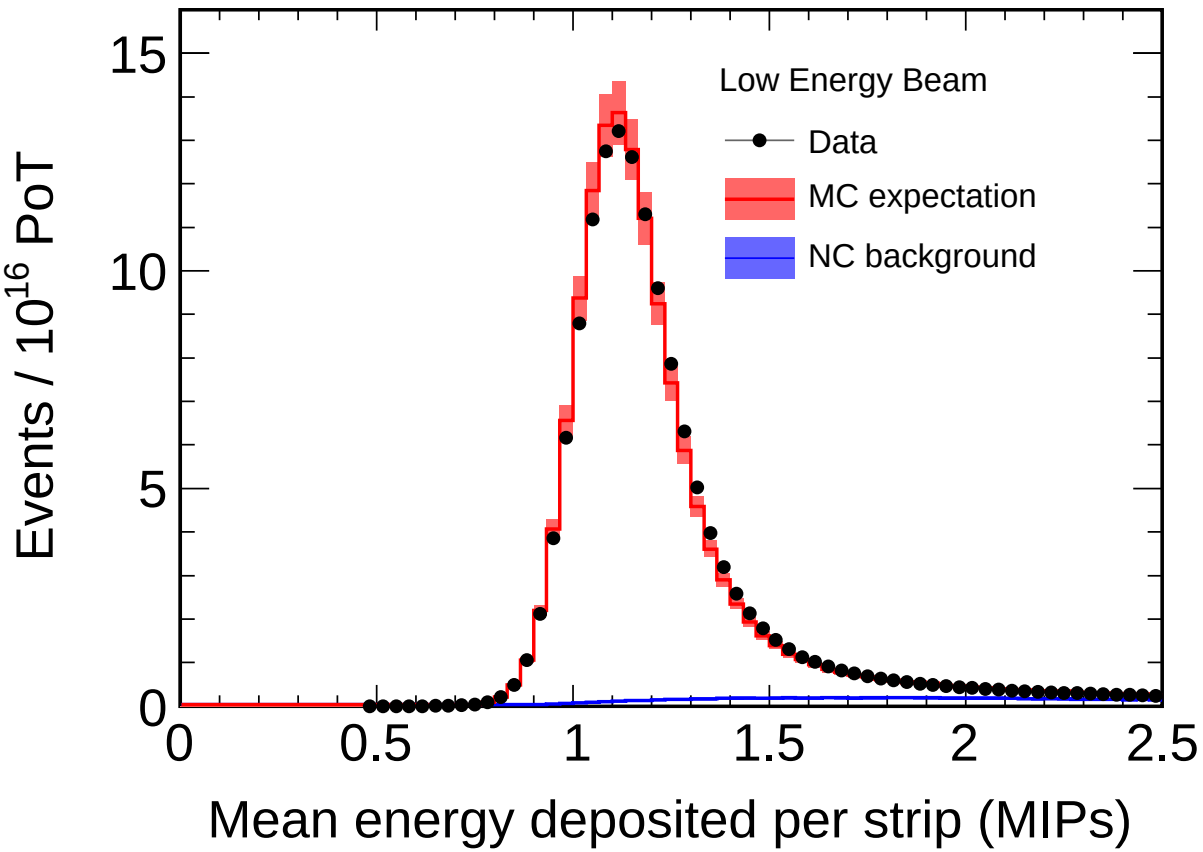

Figure 15: ND LE Data/MC Comparison: RO PID Input Variable, Mean Pulse Height.

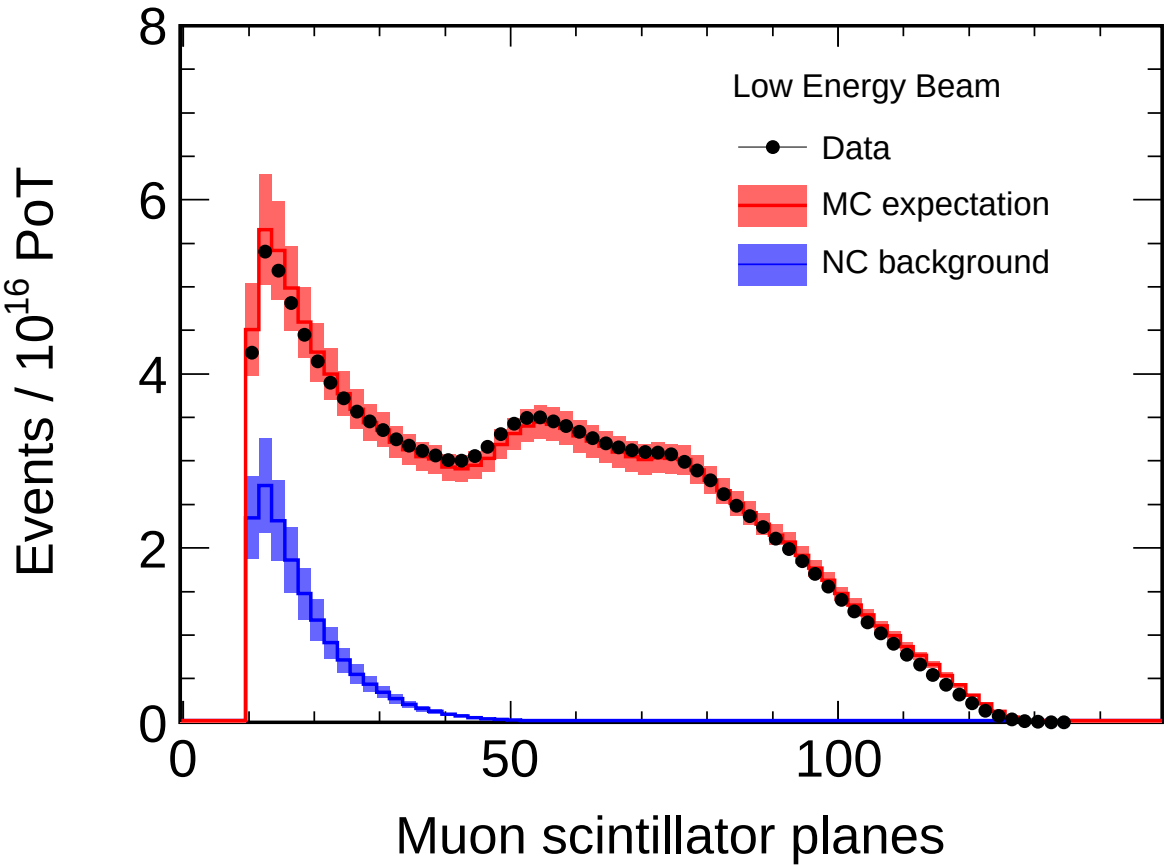

Figure 16: ND LE Data/MC Comparison: RO PID Input Variable, Scintillator Planes.

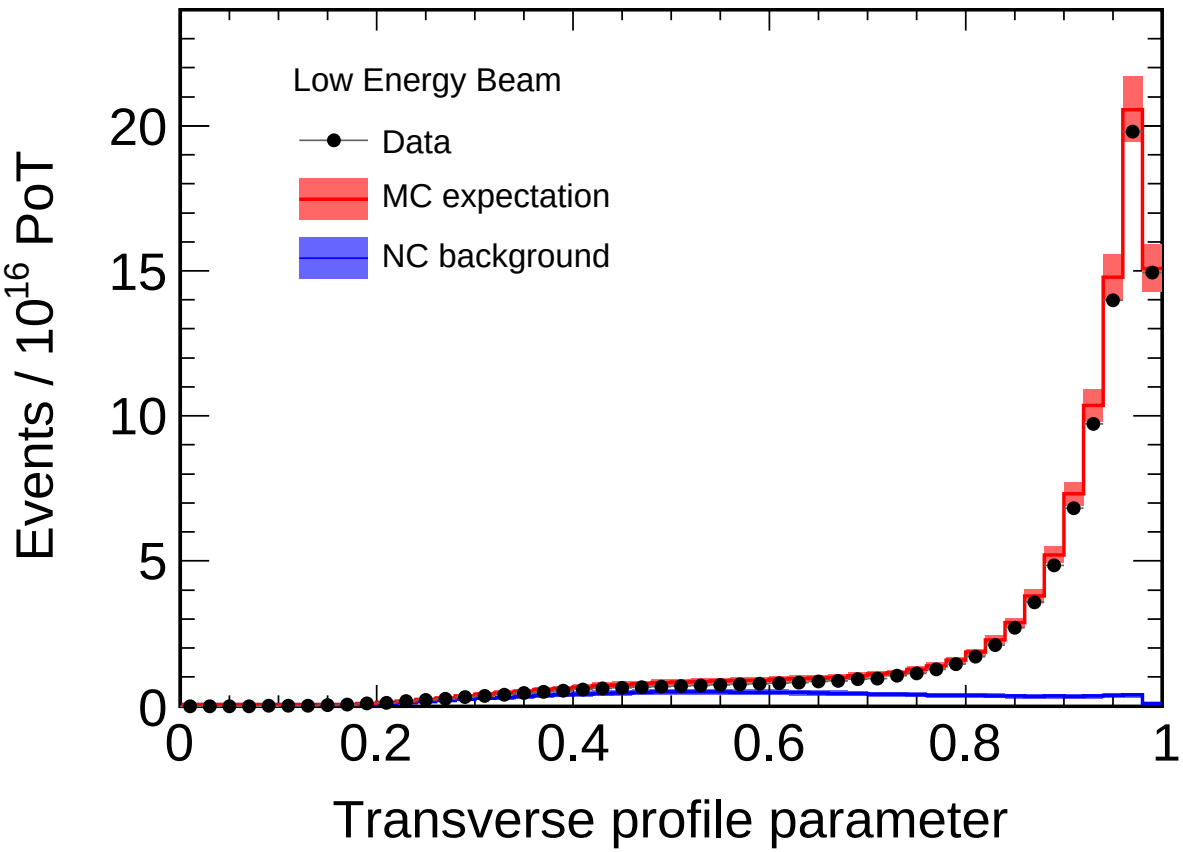

Figure 17: ND LE Data/MC Comparison: RO PID Input Variable, Transverse Profile Parameter.

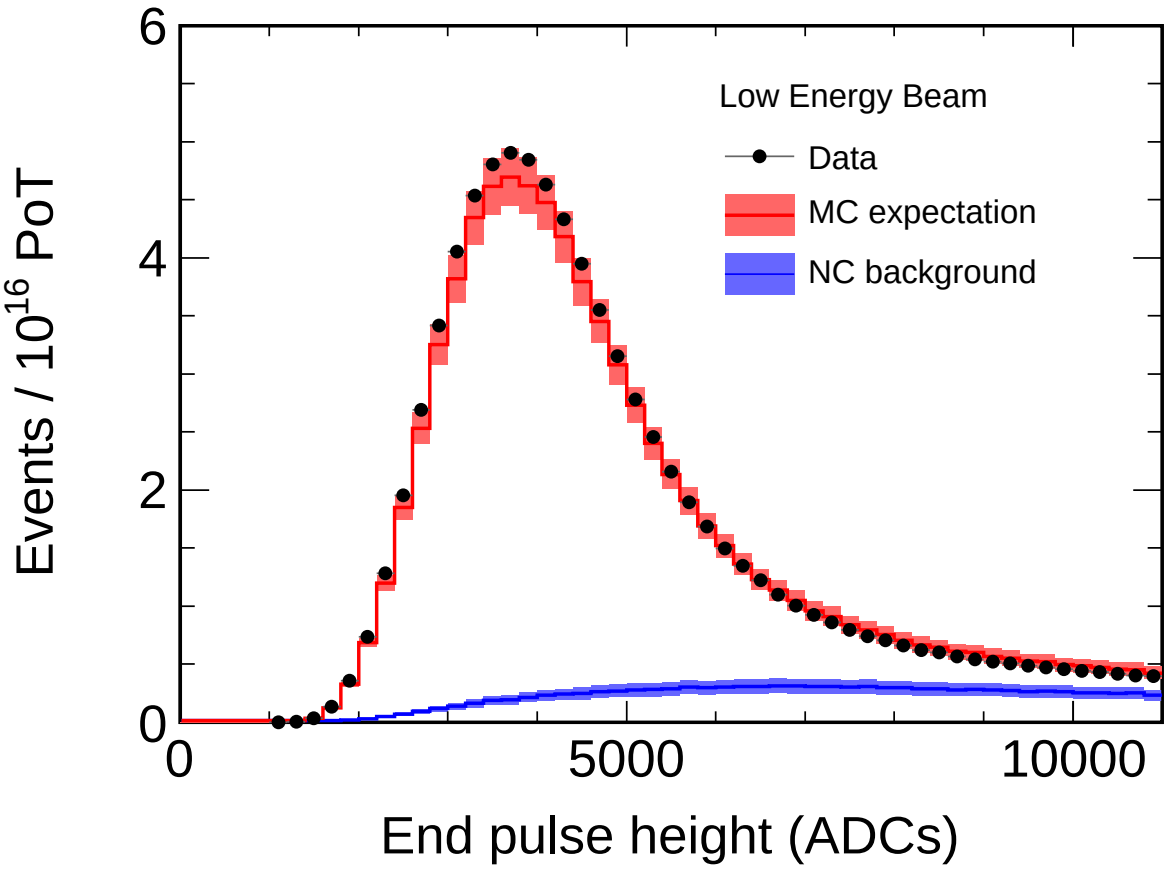

Figure 18: ND LE Data/MC Comparison: JM PID Input Variable, End Pulse Height.

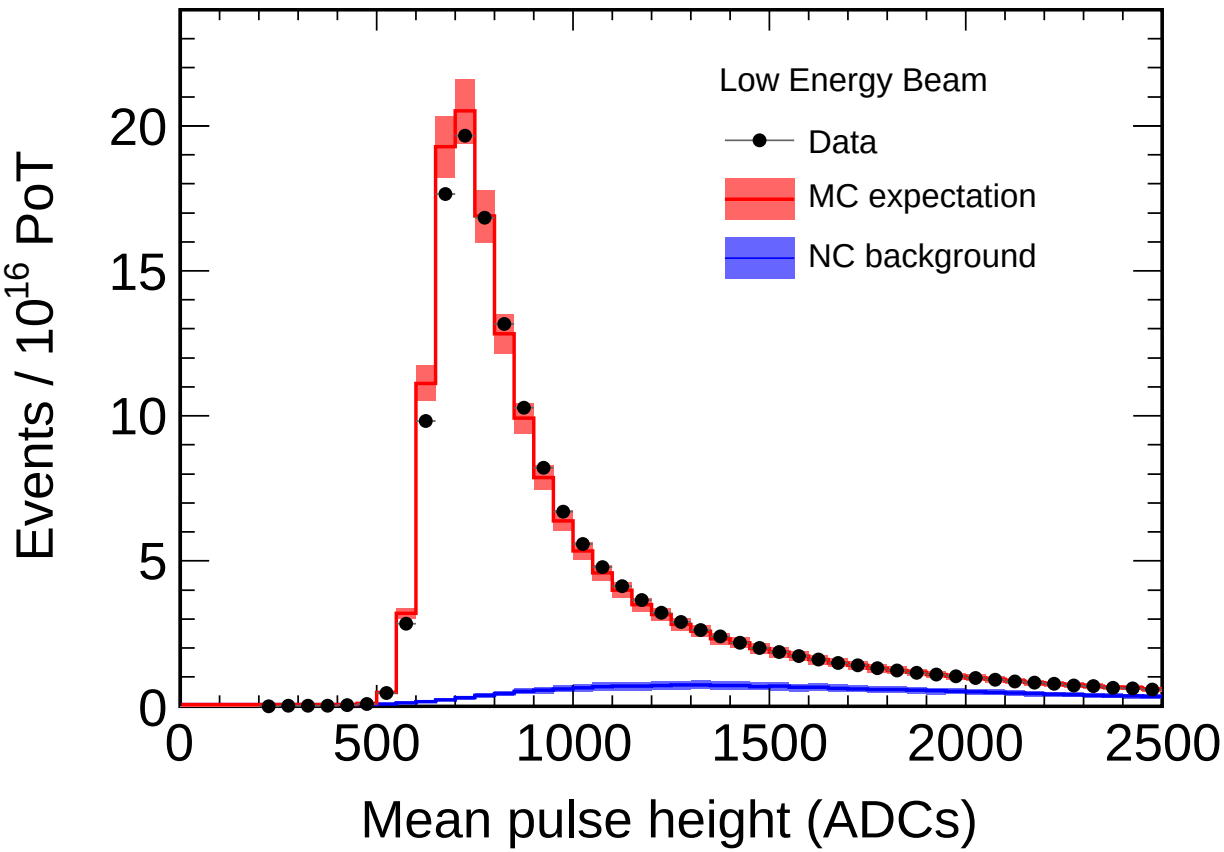

Figure 19: ND LE Data/MC Comparison: JM PID Input Variable, Mean Pulse Height.

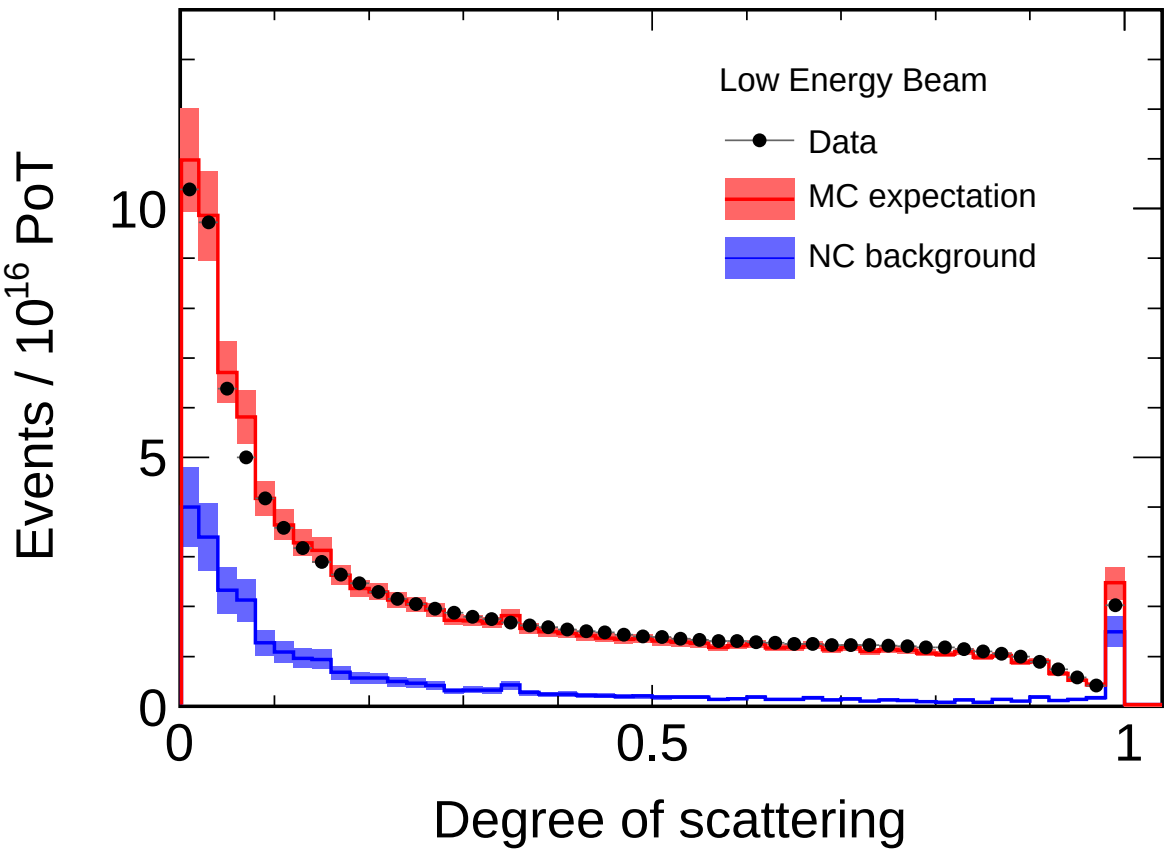

Figure 20: ND LE Data/MC Comparison: JM PID Input Variable, Degree of Scattering.

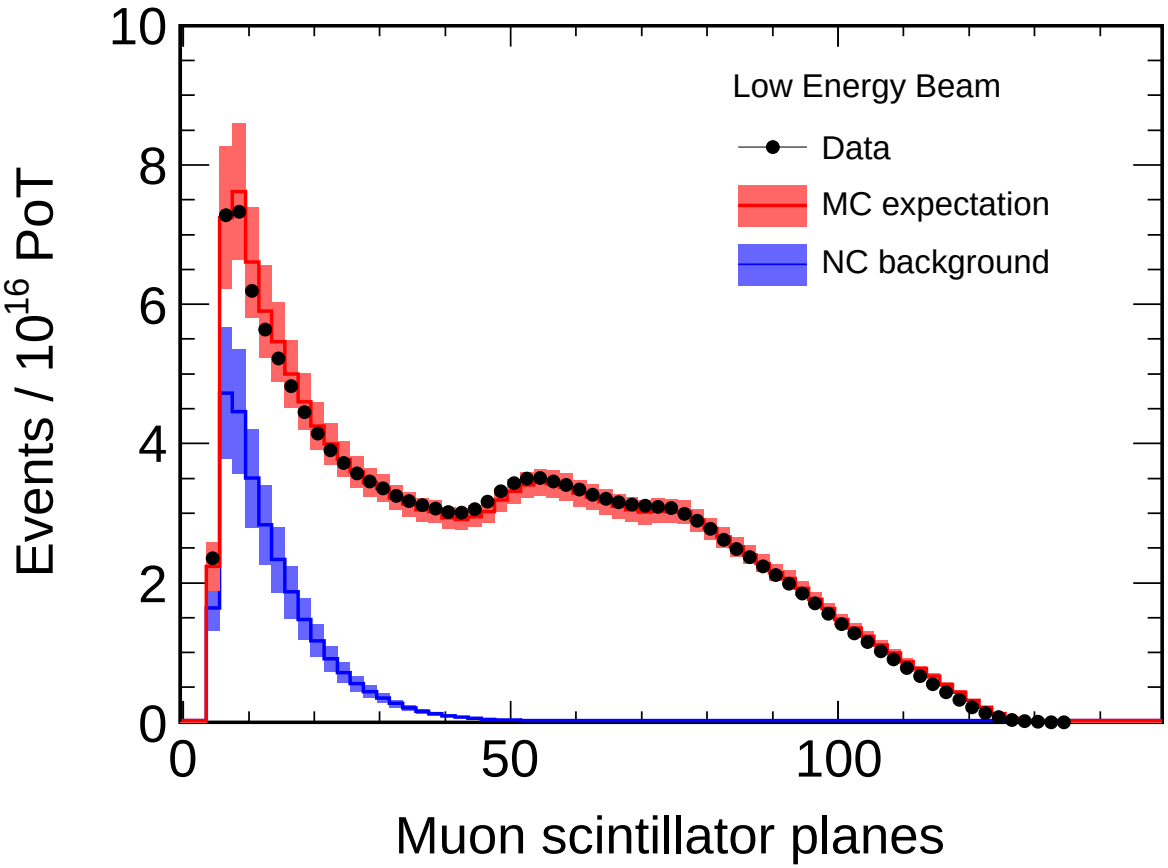

Figure 21: ND LE Data/MC Comparison: JM PID Input Variable, Scintillator Planes.

Far detector PID plots

minos-doc-6852

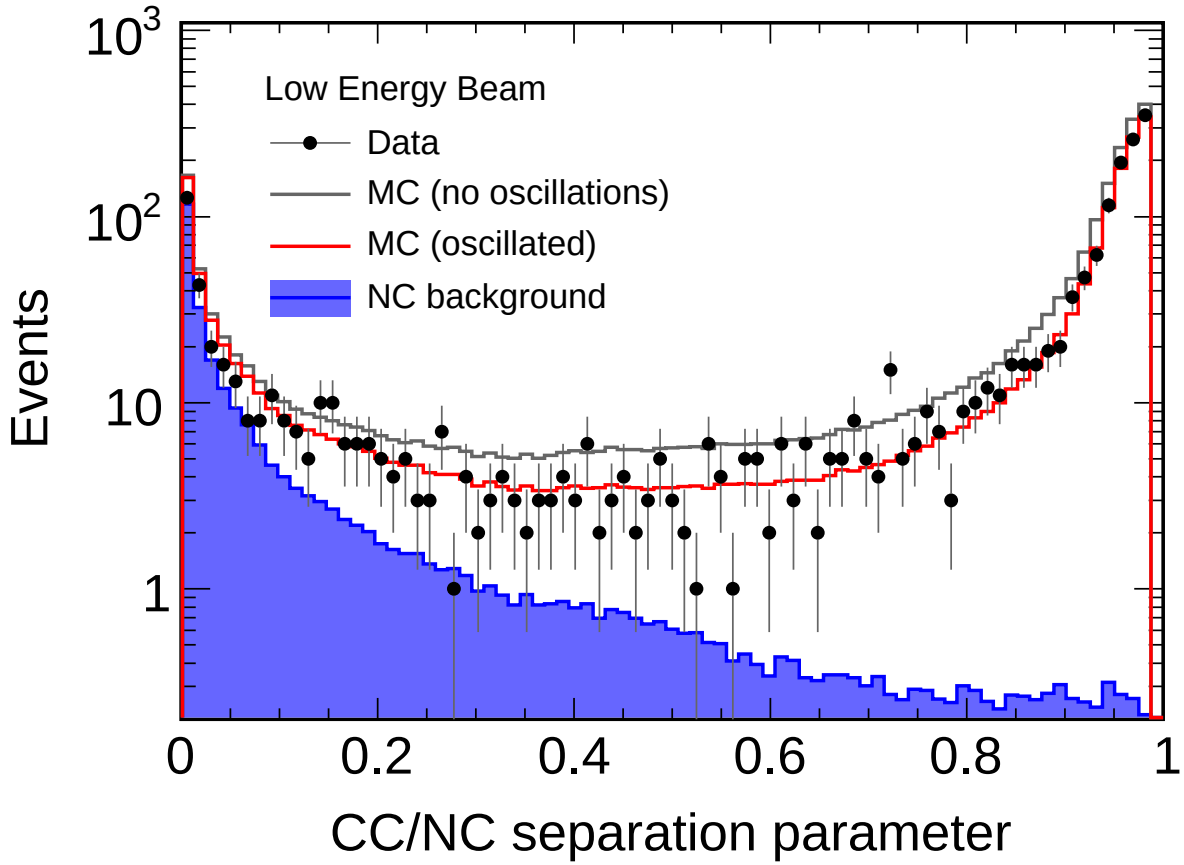

Figure 22: FD LE Data/MC Comparison: RO PID Variable.

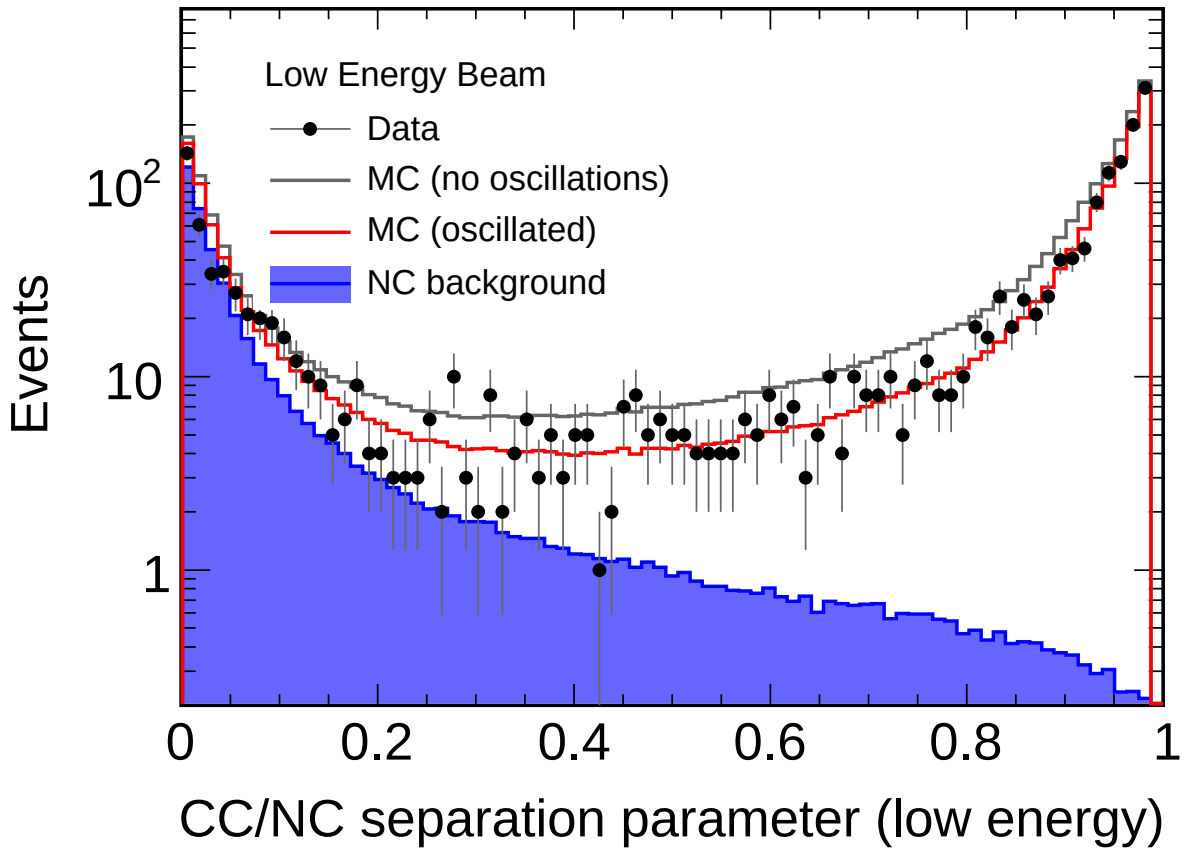

Figure 23: FD LE Data/MC Comparison: JM PID Variable.

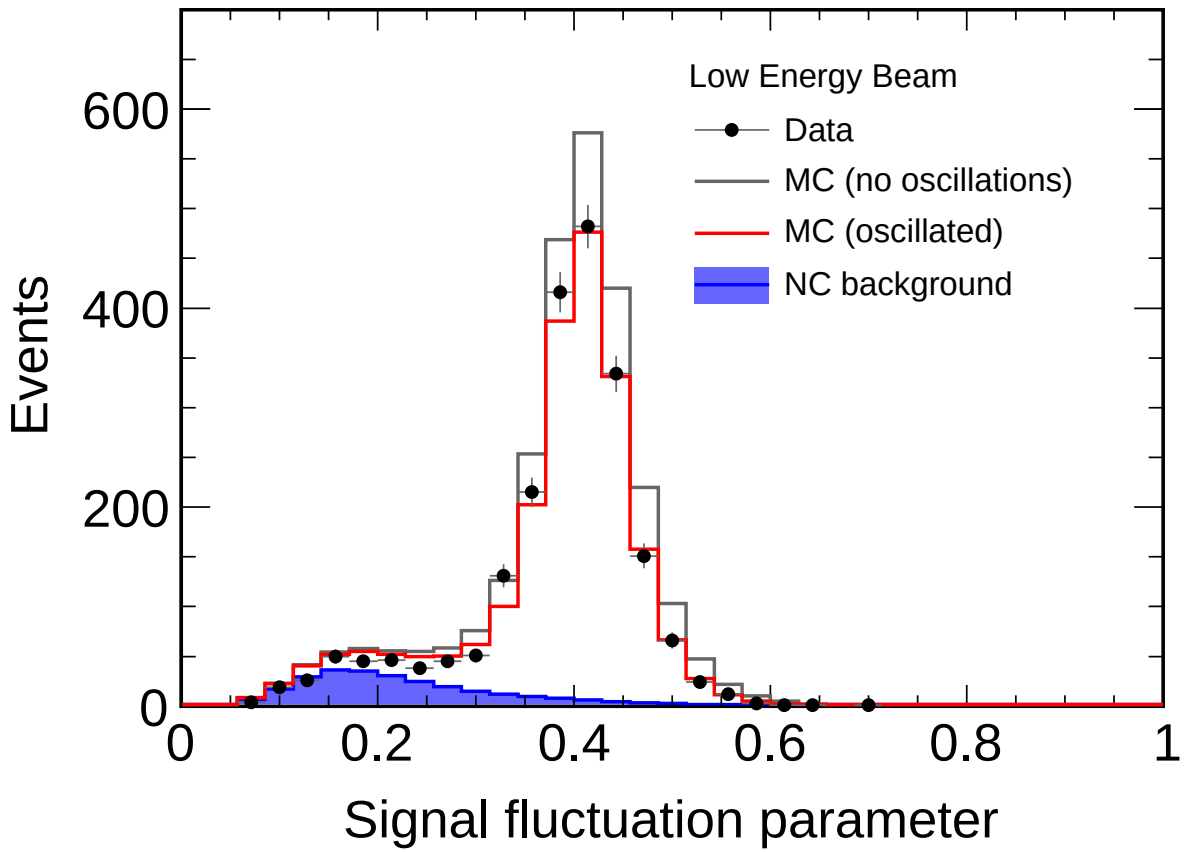

Figure 24: FD LE Data/MC Comparison: RO PID Input Variable, Signal Fluctuation Parameter.

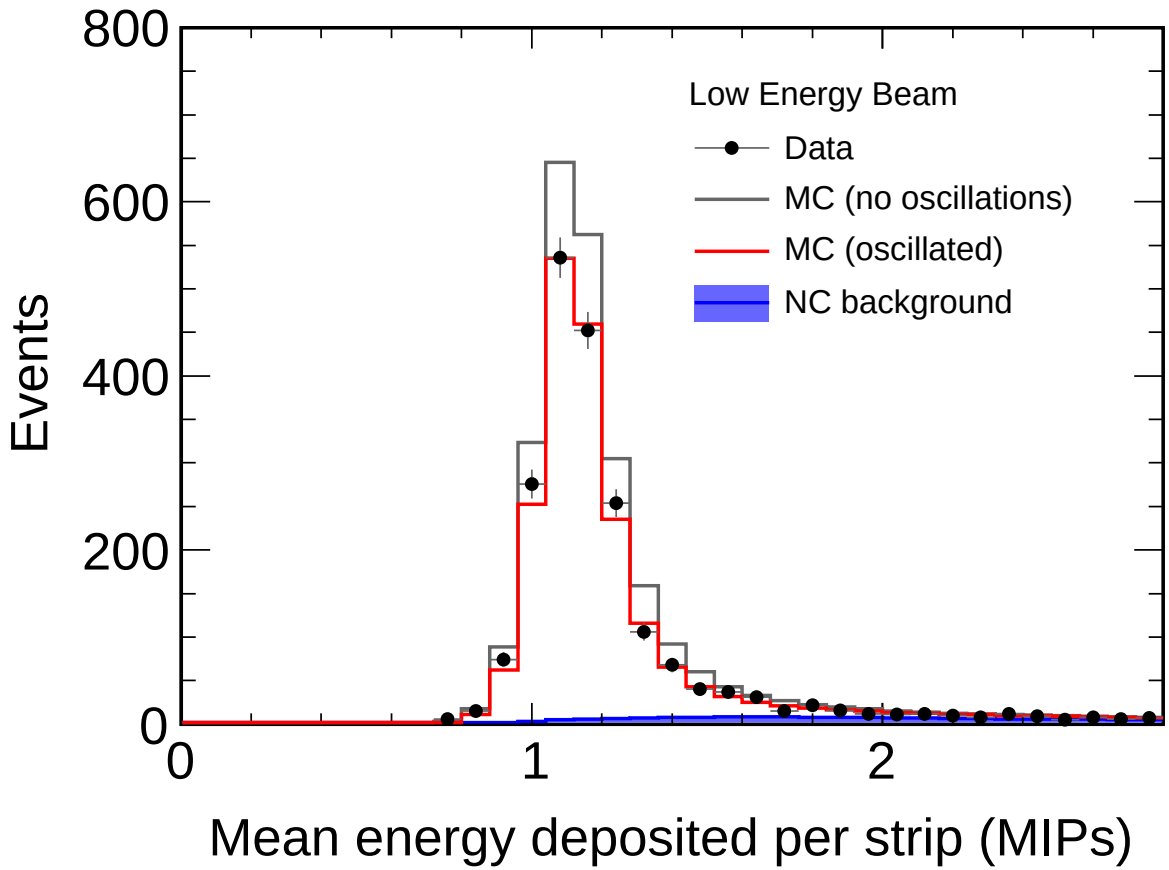

Figure 25: FD LE Data/MC Comparison: RO PID Input Variable, Mean Pulse Height.

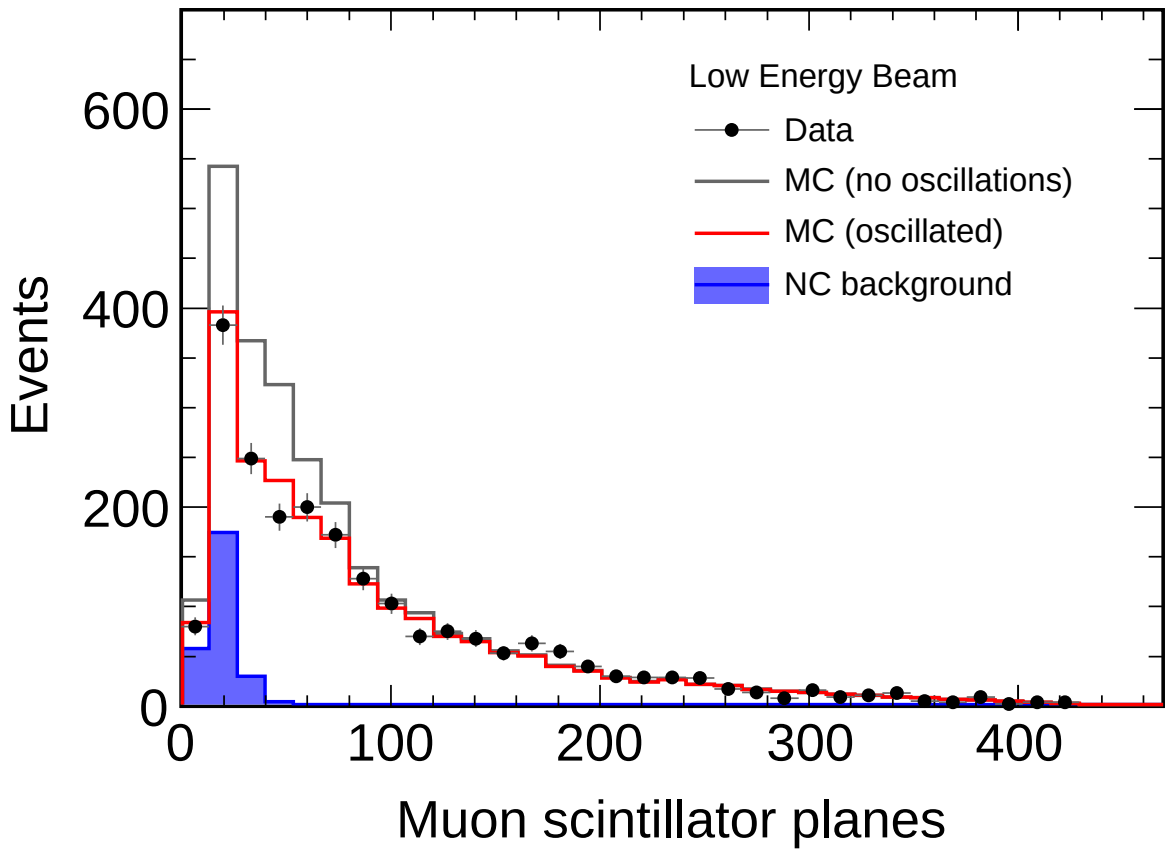

Figure 26: FD LE Data/MC Comparison: RO PID Input Variable, Scintillator Planes.

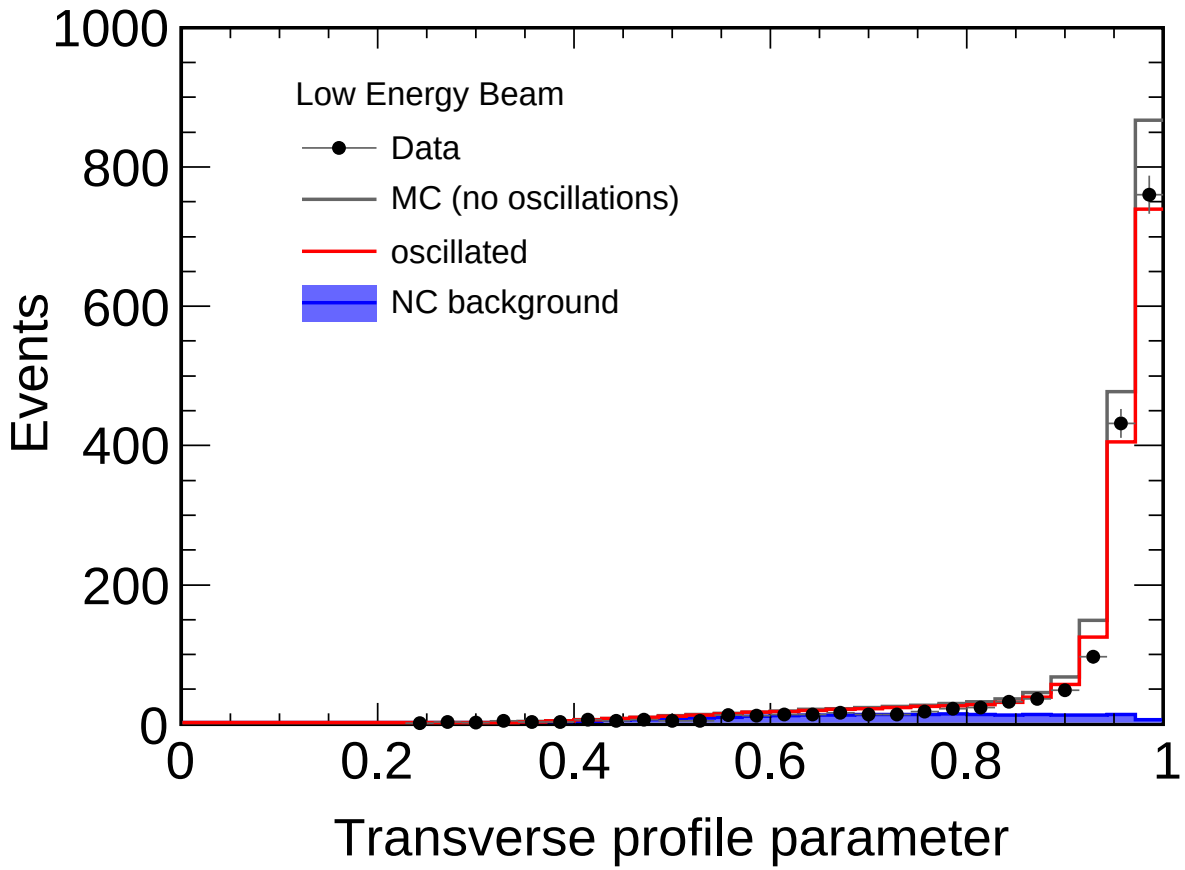

Figure 27: FD LE Data/MC Comparison: RO PID Input Variable, Transverse Profile Parameter.

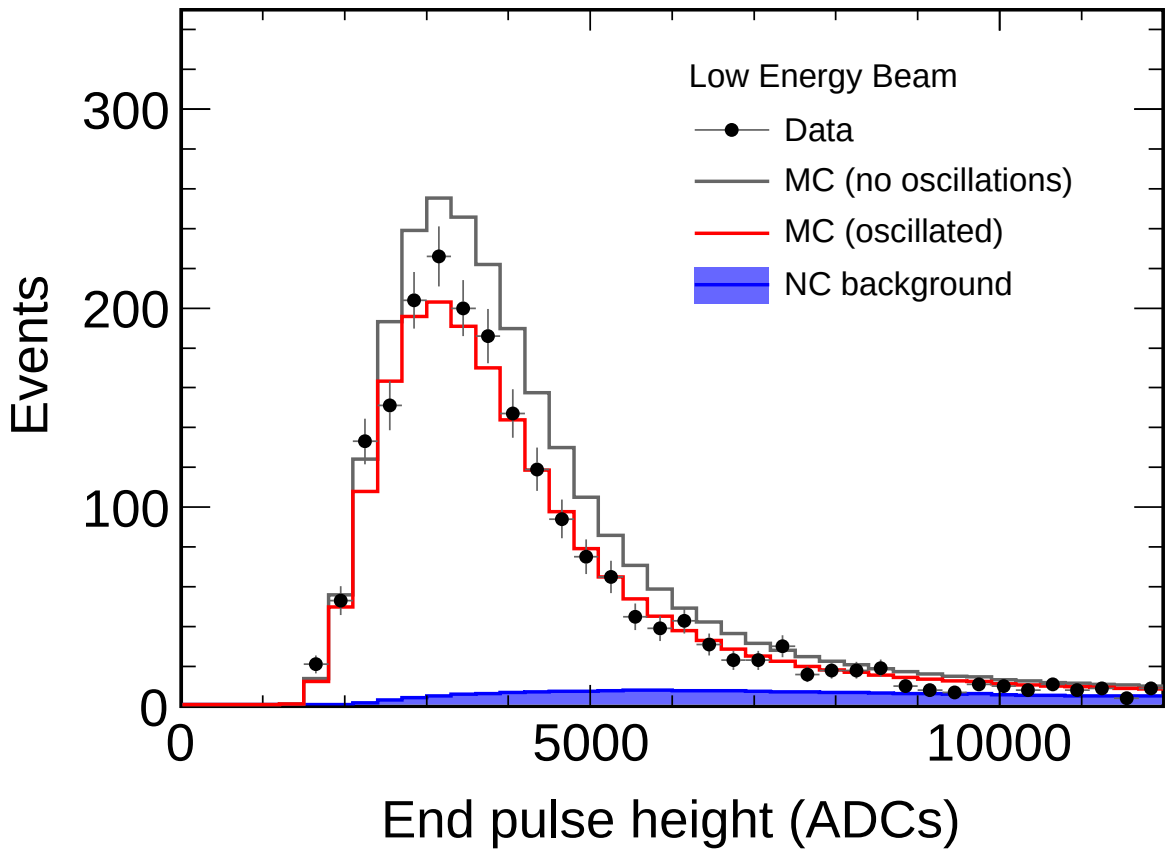

Figure 28: FD LE Data/MC Comparison: JM PID Input Variable, End Pulse Height.

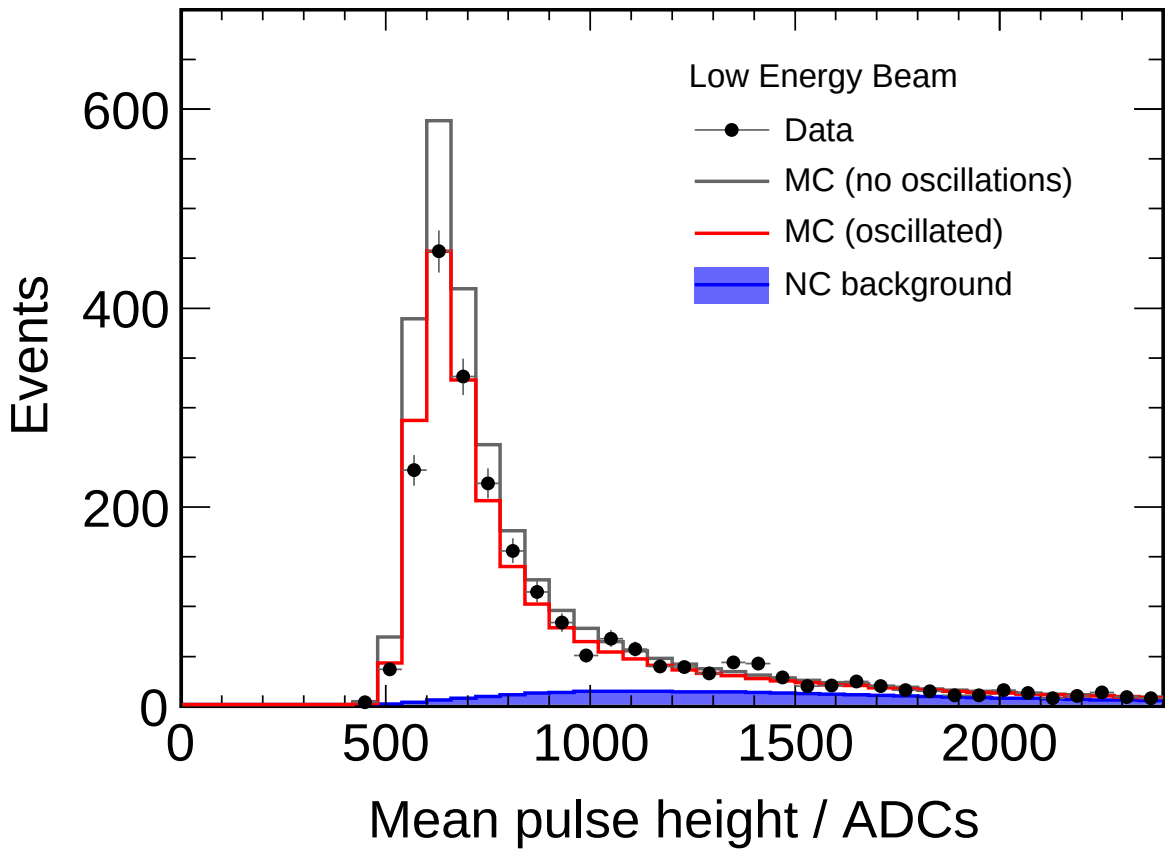

Figure 29: FD LE Data/MC Comparison: JM PID Input Variable, Mean Pulse Height.

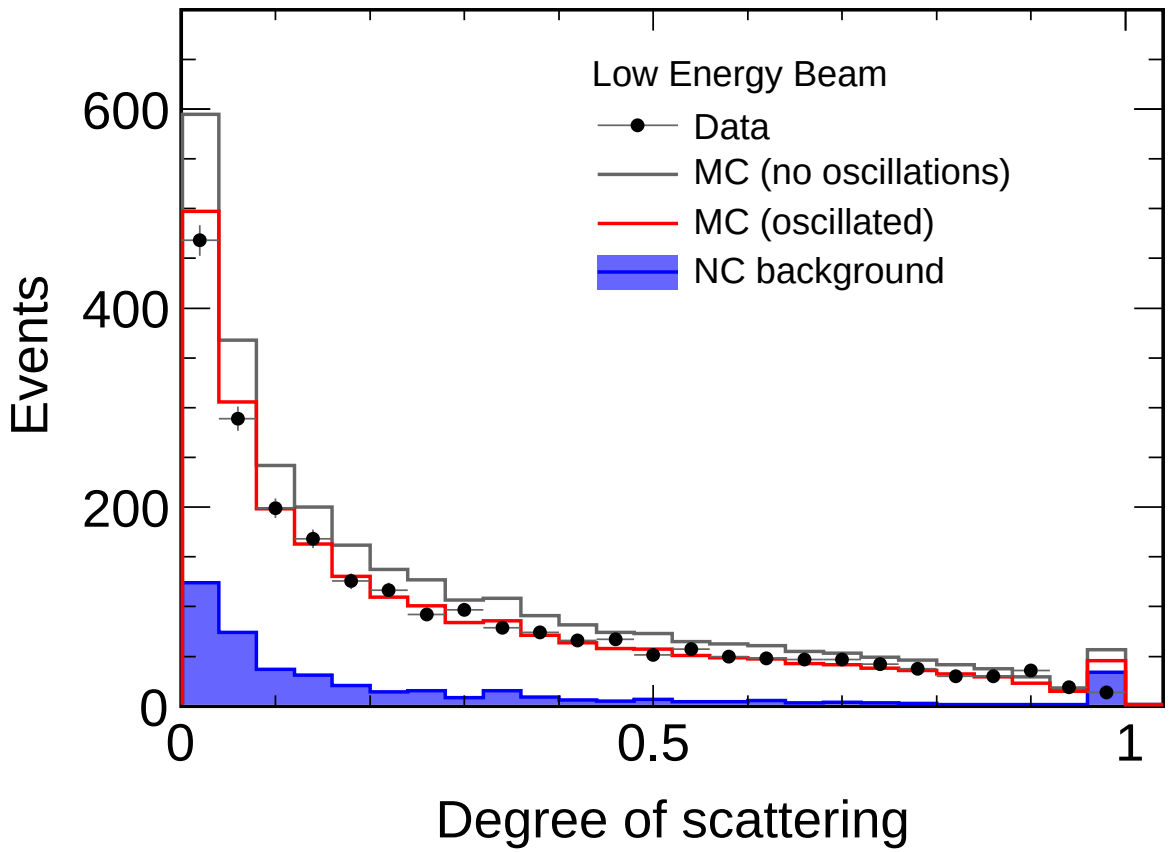

Figure 30: FD LE Data/MC Comparison: JM PID Input Variable, Degree of Scattering.

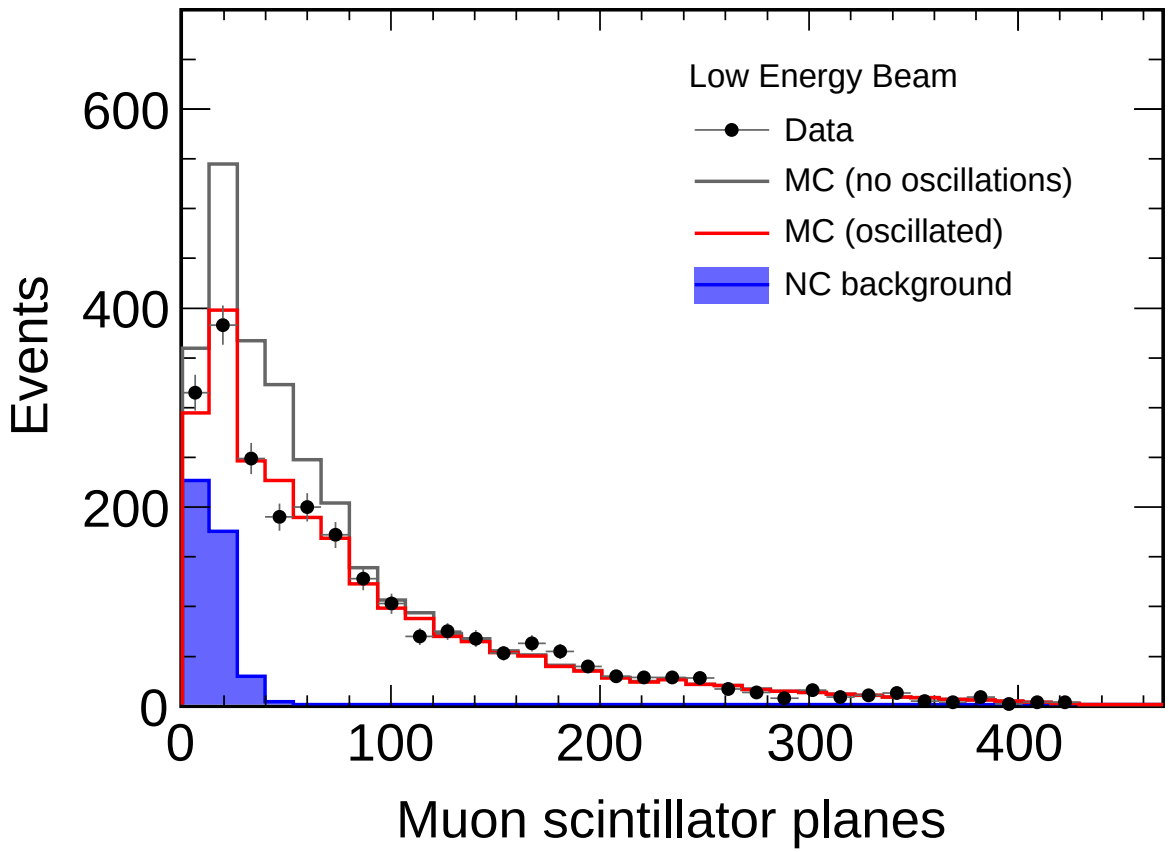

Figure 31: FD LE Data/MC Comparison: JM PID Input Variable, Scintillator Planes.

Other PID plots

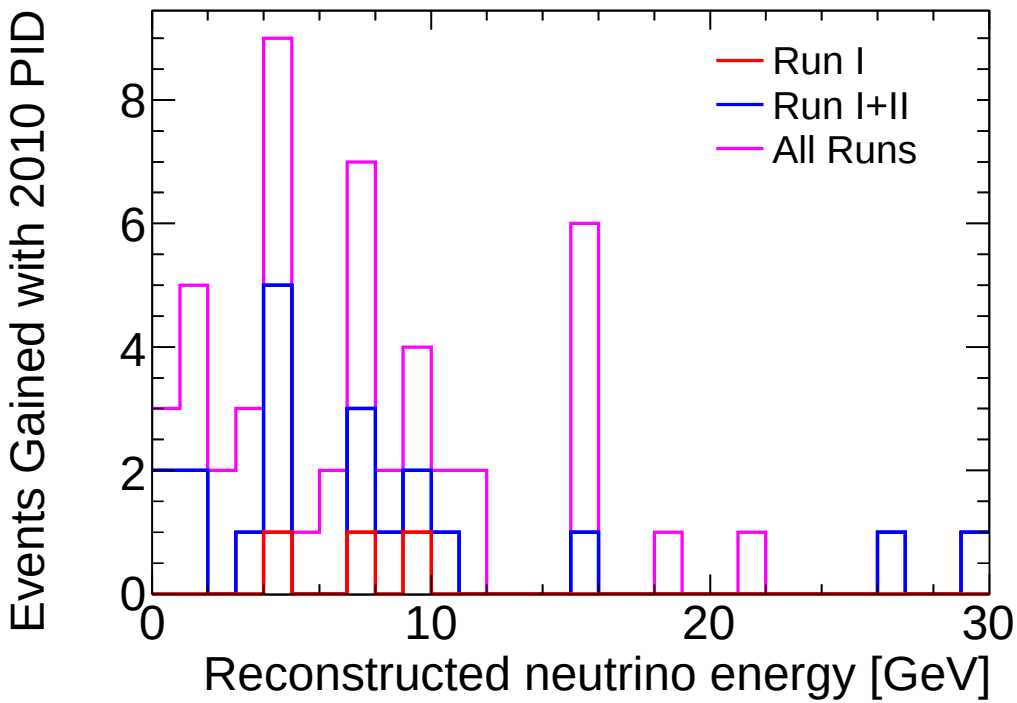

Figure 32: Fiducial events that are gained by a relaxed 2008 cut (greater than 0.25) and an alternate kNN (greater than 0.5) used together in a logical 'OR' for Runs 1, 2 and 3 in bins of energy. The 2008 Analysis used a more stringent PID cut (2008 kNN $>$ 0.3) for comparison

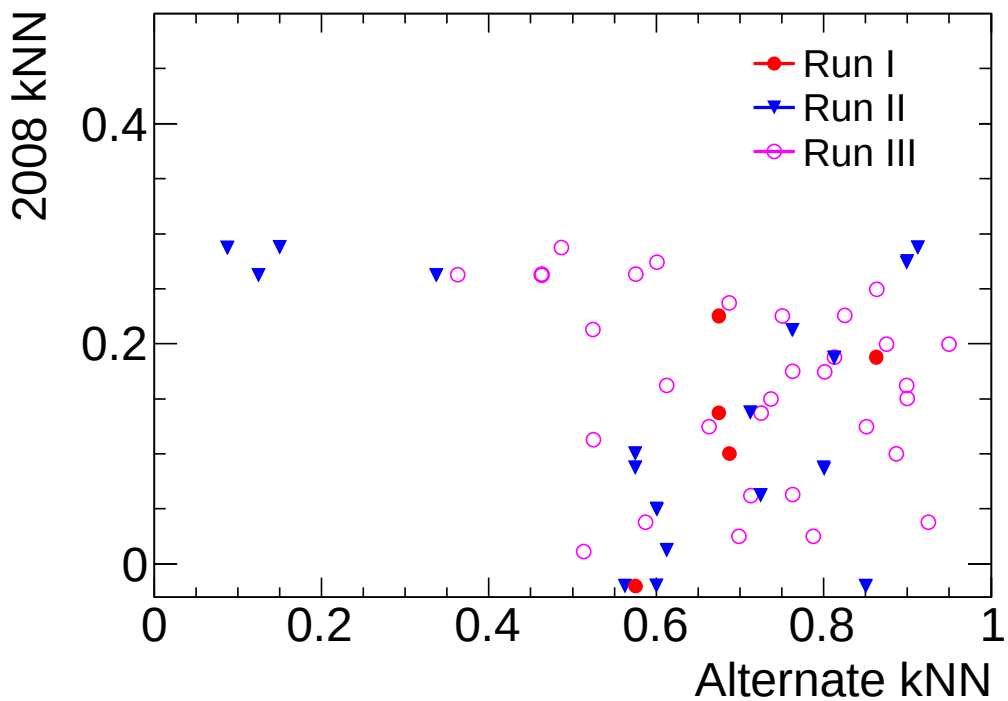

Figure 33: Fiducial events that are gained by a relaxed 2008 cut (greater than 0.25) and an alternate kNN (greater than 0.5) used together in a logical 'OR' for Runs 1, 2 and 3. The X-axis represents the new 'alternate' kNN in the 2010 Analysis. The 2008 Analysis used a more stringent PID cut (2008 kNN $>$ 0.3) for comparison

MRCC (NC background systematic)

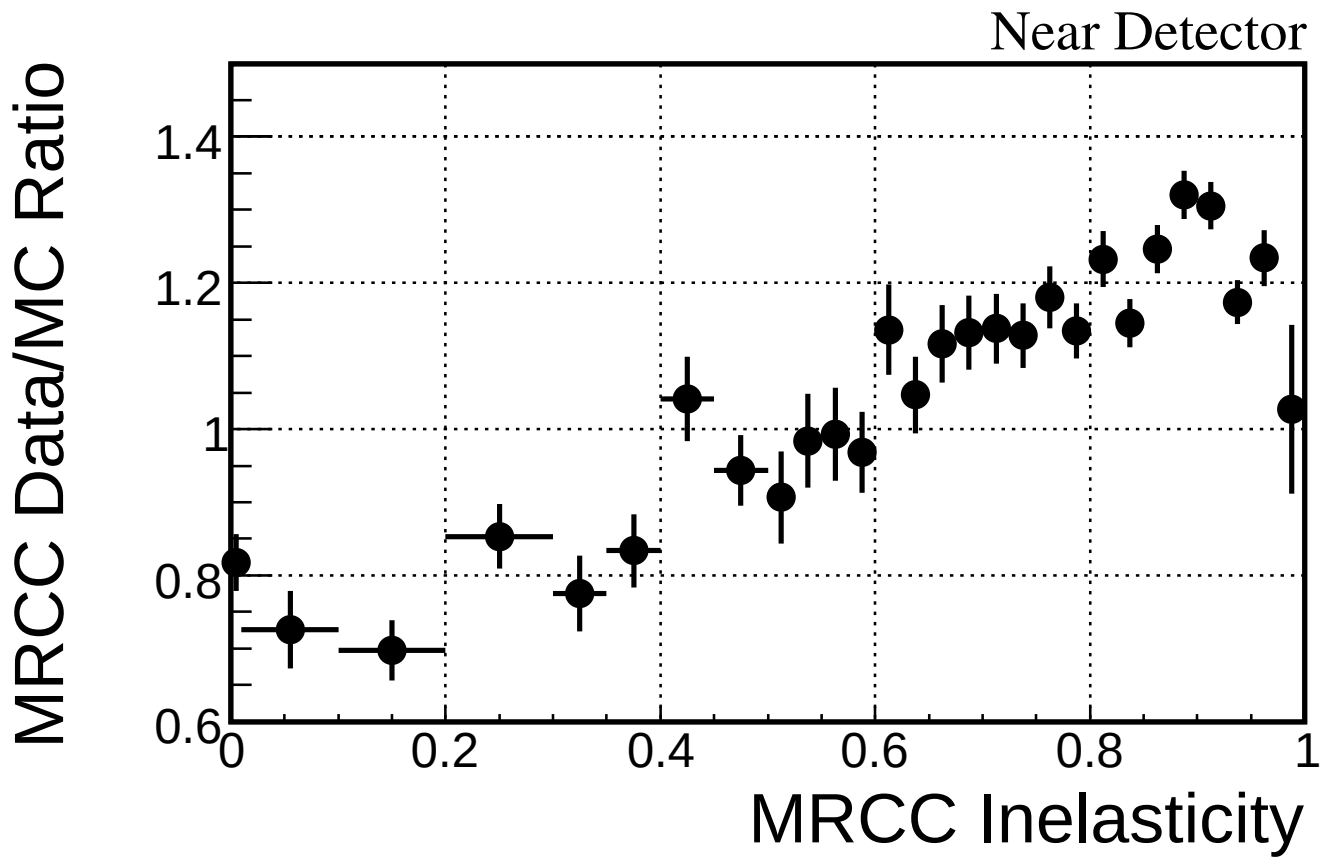

Figure 34: The ratio of MRCC data/MC (dogwood 3 daikon 07, with the reconstructed energy, but not shower kNN energy- which was not used for most of the analysis)

Data/MC Plots

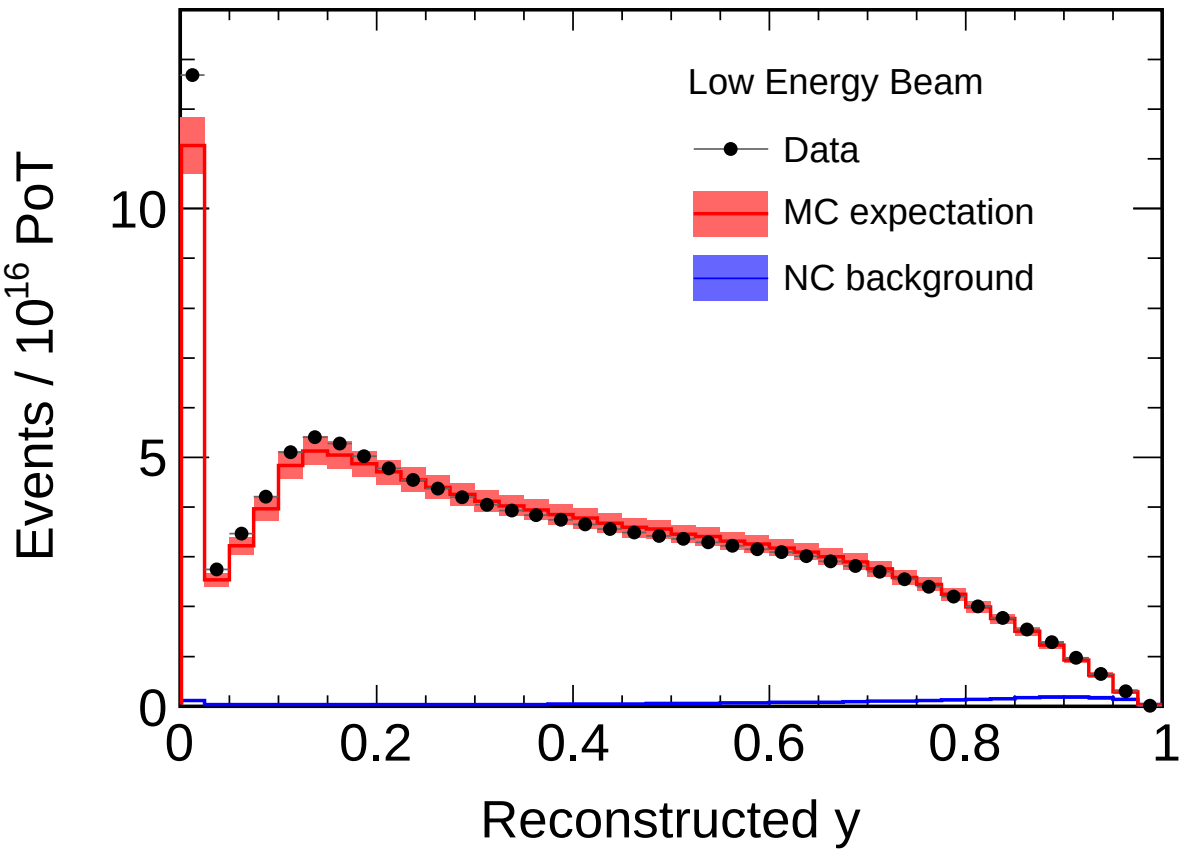

Figure 35: ND LE Data/MC Comparison: Reconstructed y.

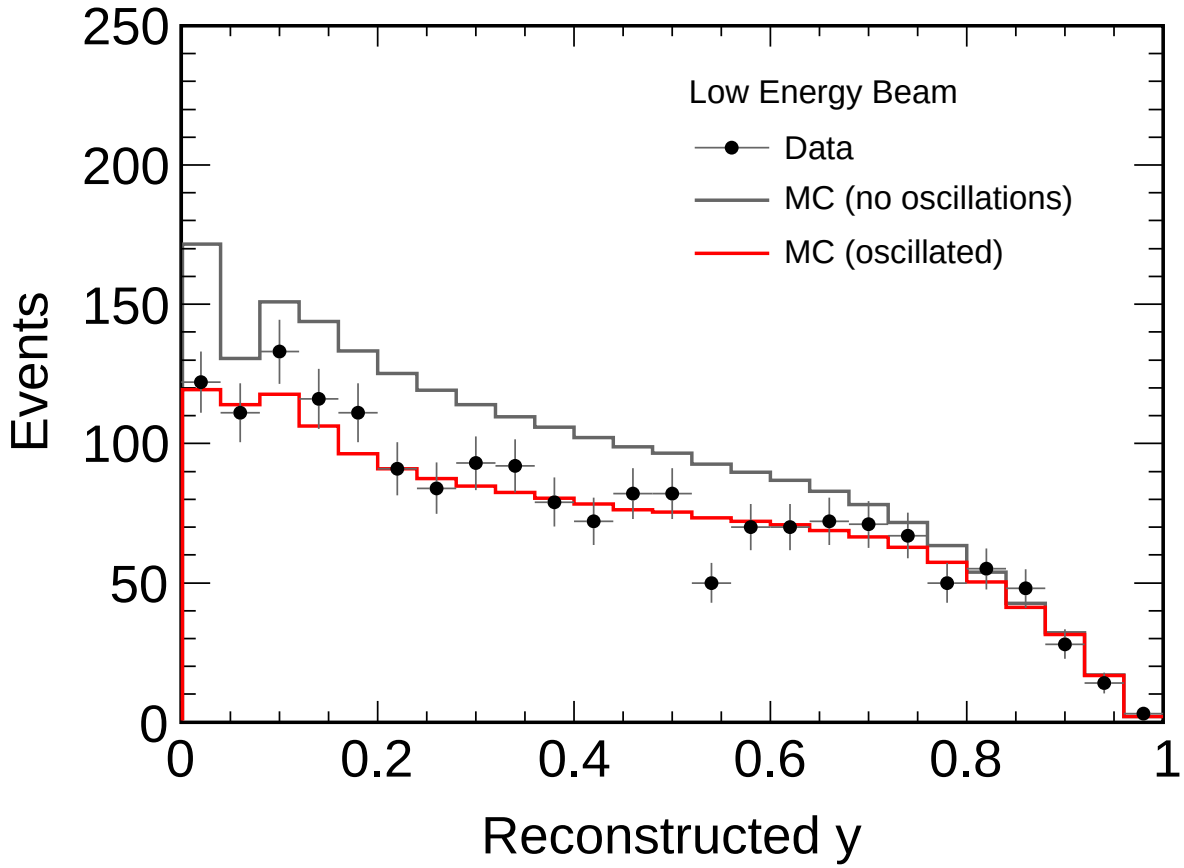

Figure 36: FD LE Data/MC Comparison: Reconstructed y.

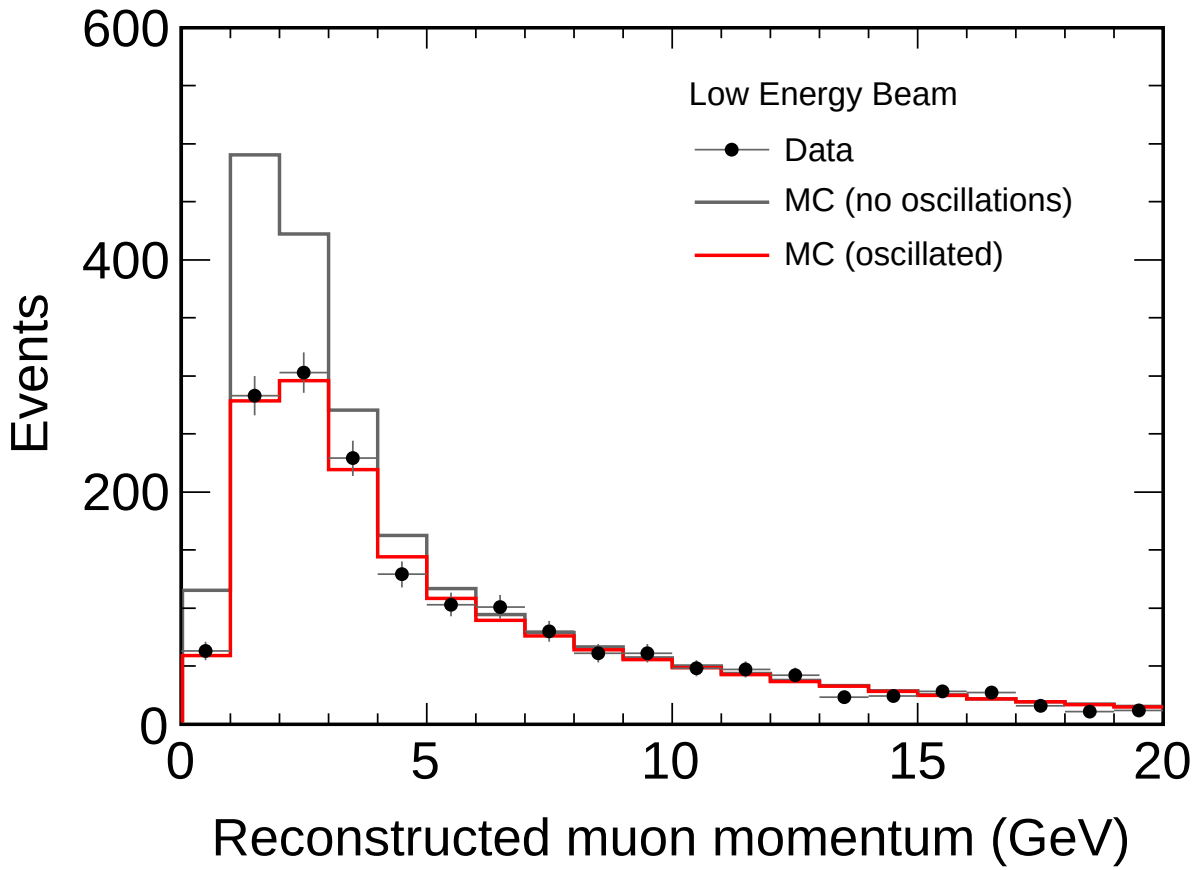

Figure 37: FD LE Data/MC Comparison: Reconstructed Muon Momentum.

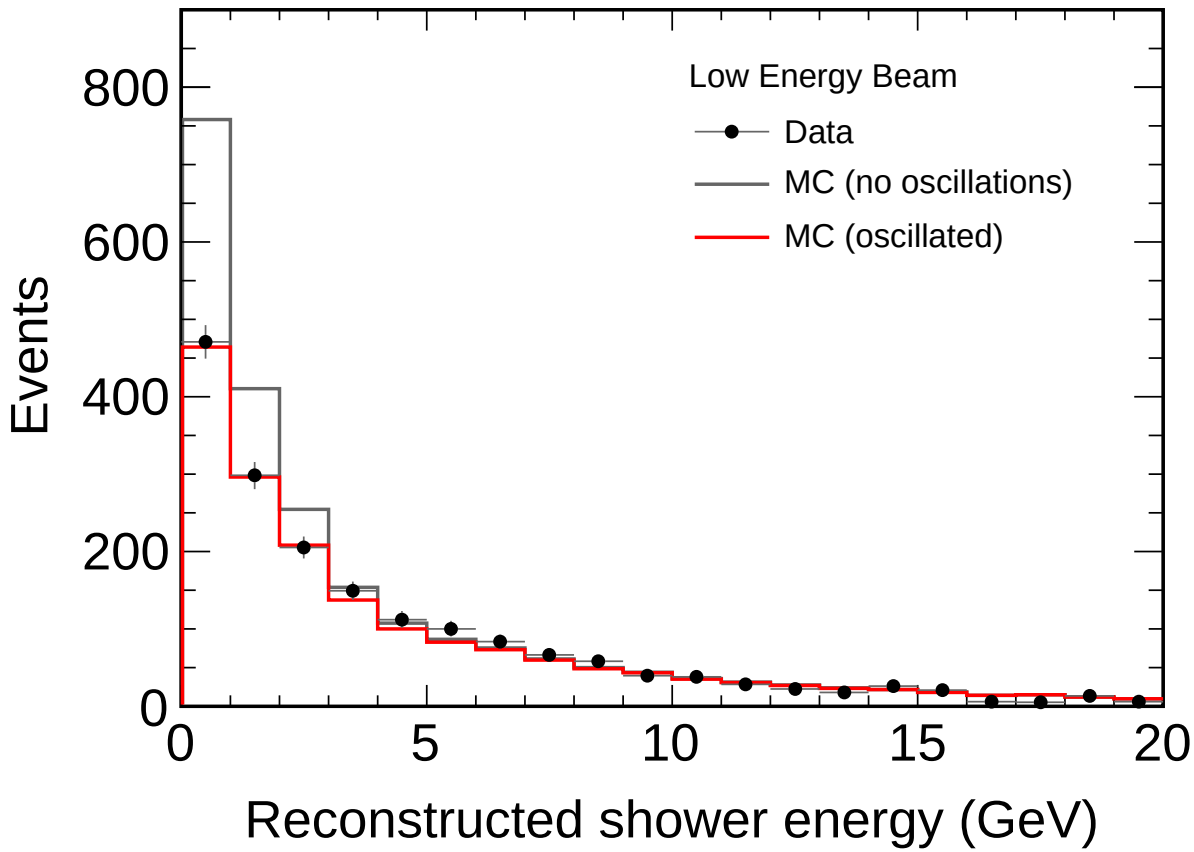

Figure 38: FD LE Data/MC Comparison: Reconstructed Shower Energy.

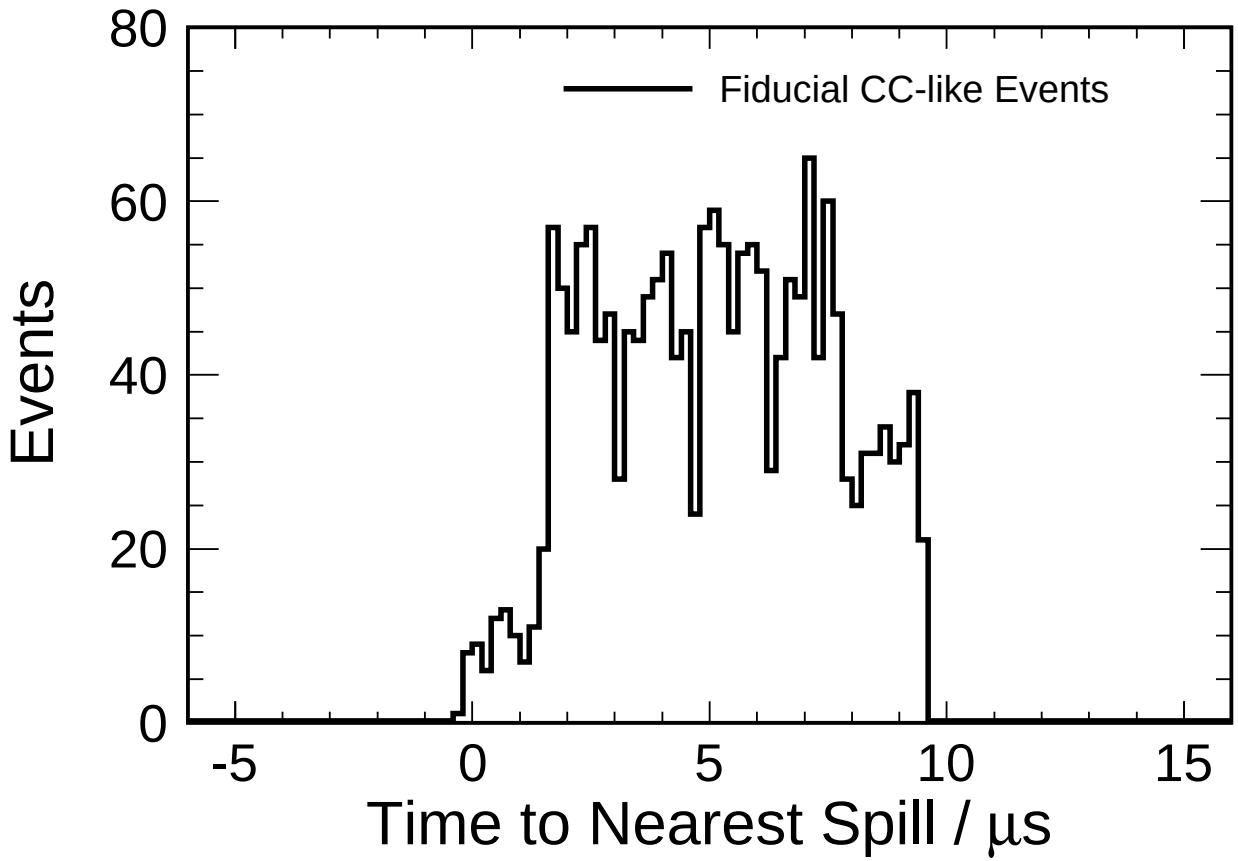

Figure 39: FD LE Data Distribution: Time from Event Vertex to Nearest Spill (plotted for selected fiducial CC-like events).

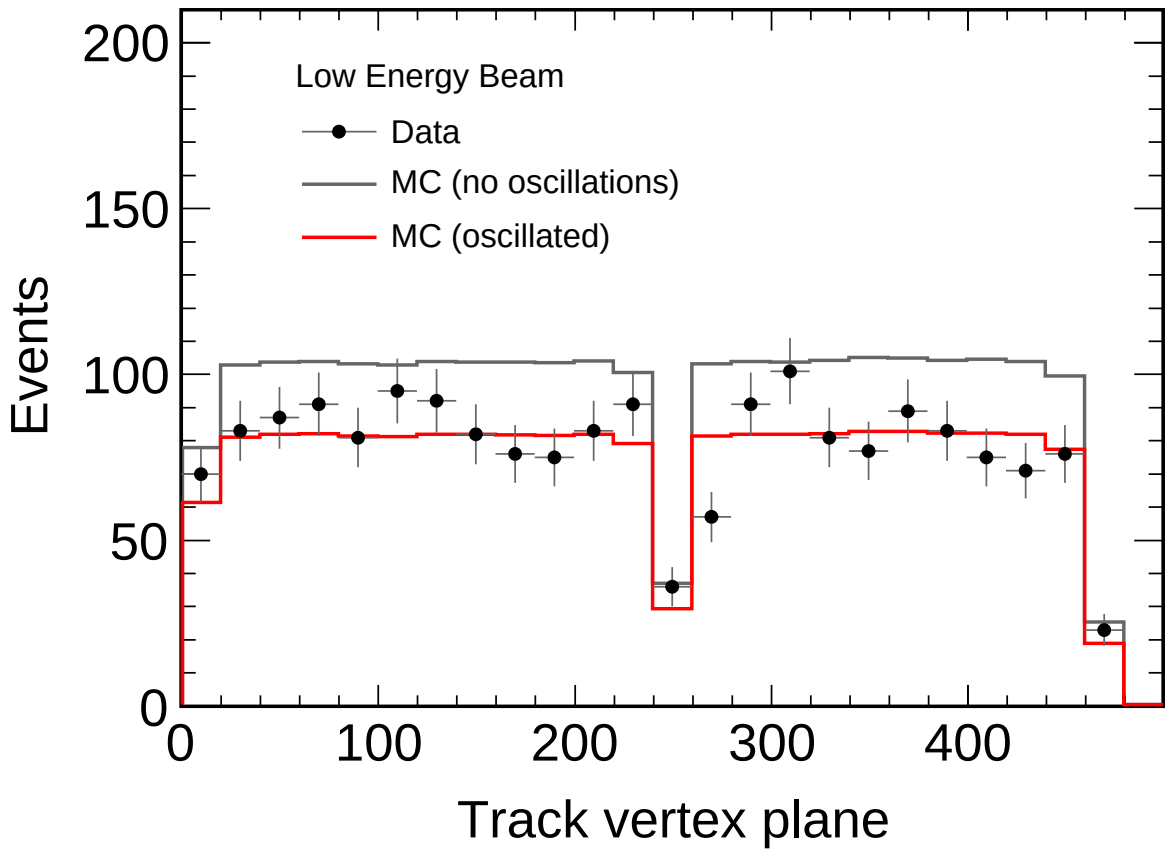

Figure 40: FD LE Data/MC Comparison: Track Vertex Plane

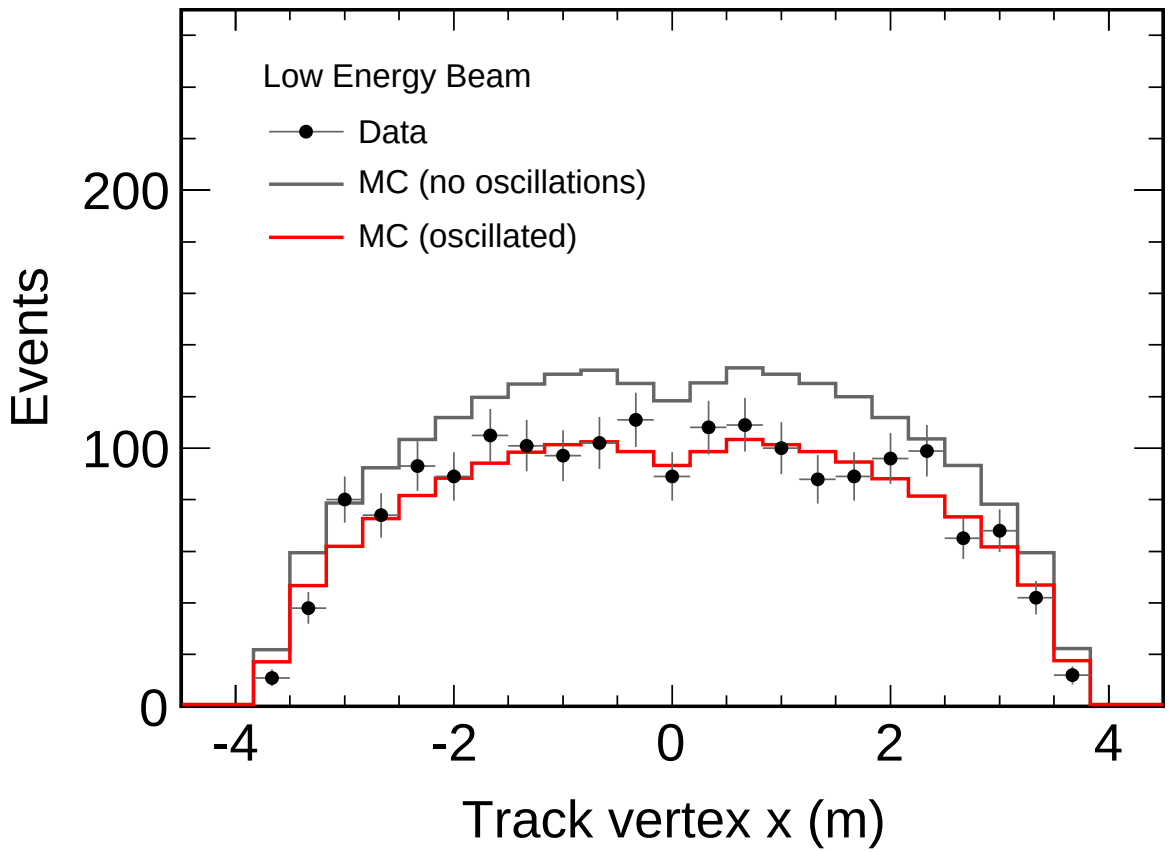

Figure 41: FD LE Data/MC Comparison: Track Vertex X

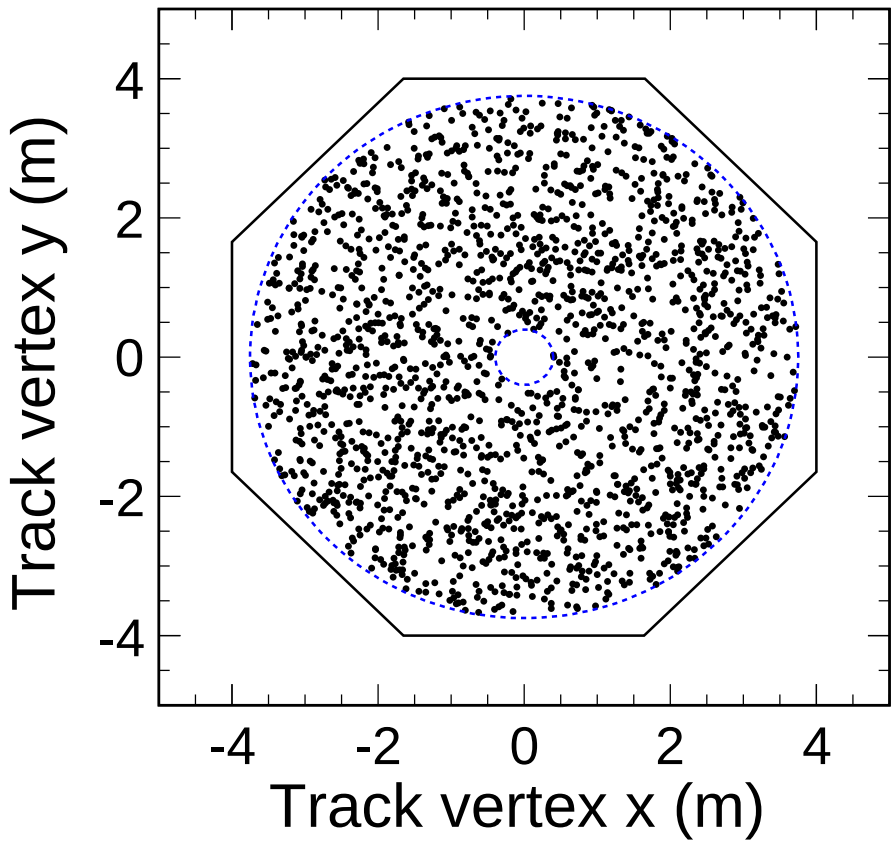

Figure 42: FD LE Data/MC Comparison: Track Vertex Y vs X

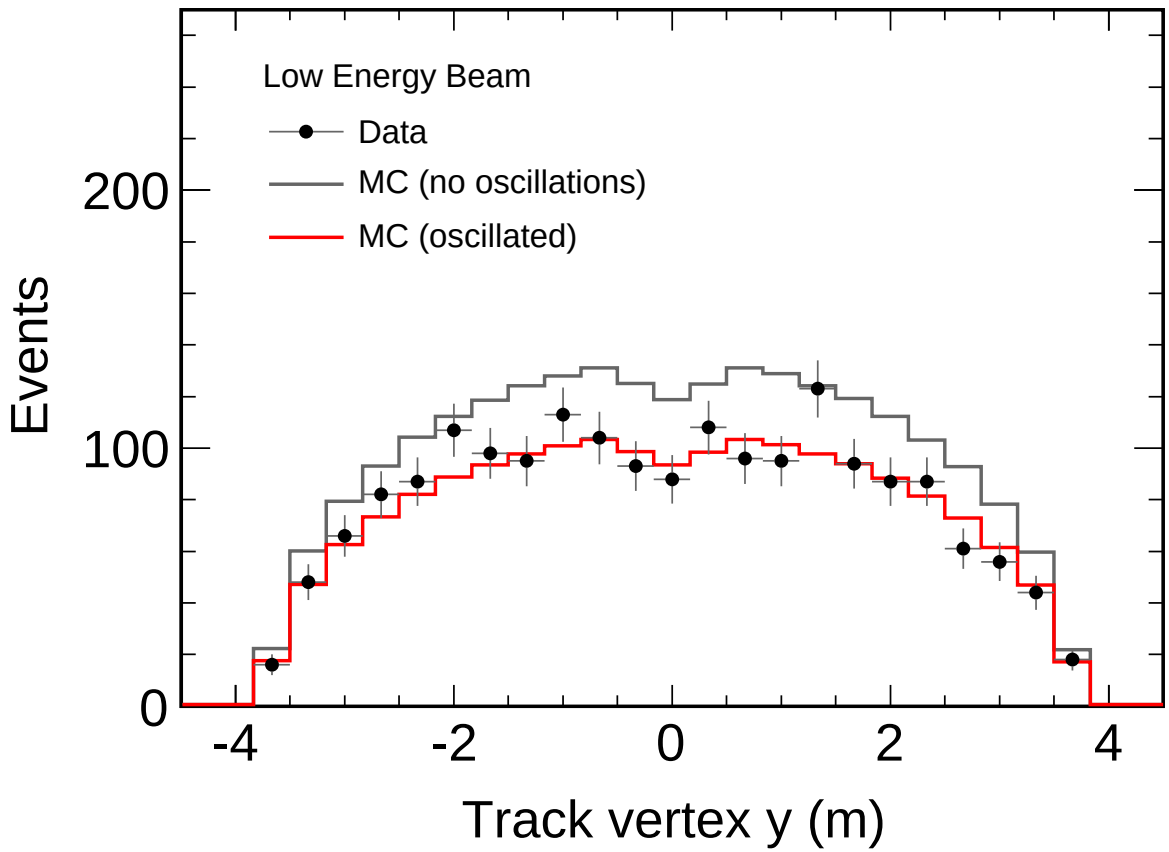

Figure 43: FD LE Data/MC Comparison: Track Vertex Y

Resolution binning

minos-doc-6887

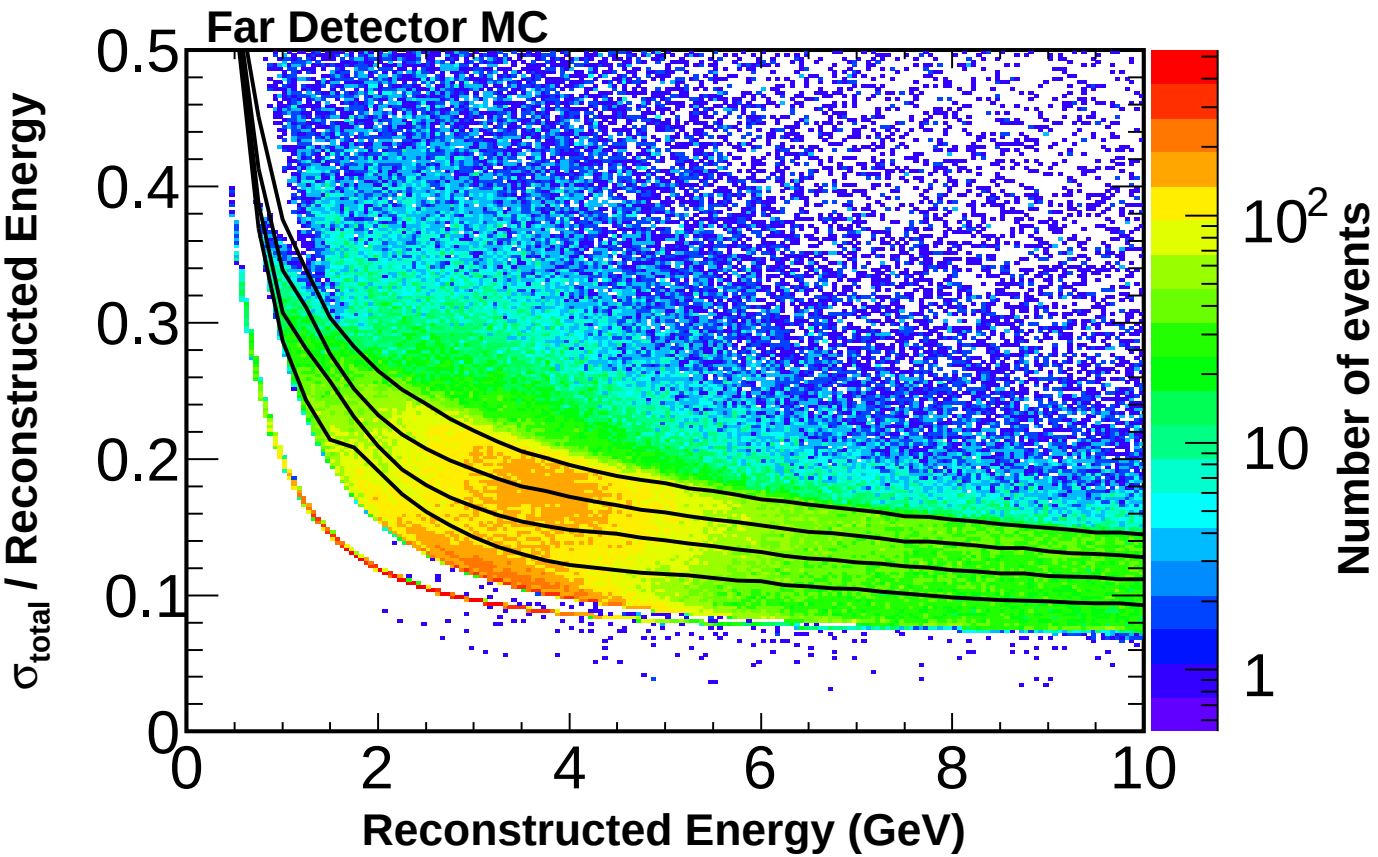

Figure 44: Event resolution is paramaterized as a function of track energy, shower energy, and track containment. Cuts are then trained as a function of reconstructed energy to define five quantiles that yield identical unoscillated predicted spectra, but have different energy resolutions. Black lines show four cuts that divide these five regions.

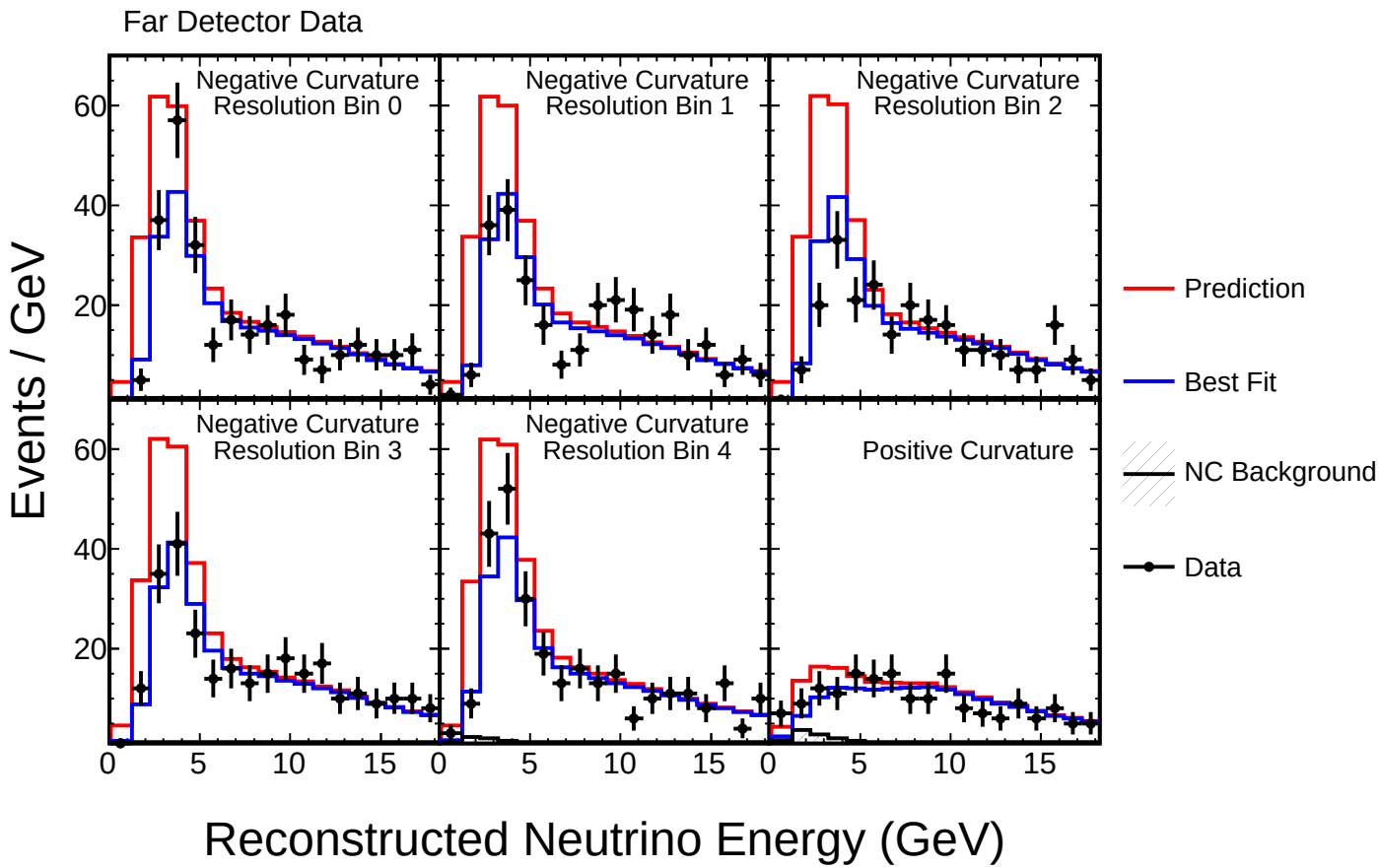

Figure 45: Far Detector events with negative curvature are split into five samples based on energy resolution, with best energy resolution events in Resolution Bin 0 and worst resolution events in Resolution Bin 4. Additionally, Far Detector events with positive curvature are included as a sixth sample. These six spectra are then fit simultaneously.

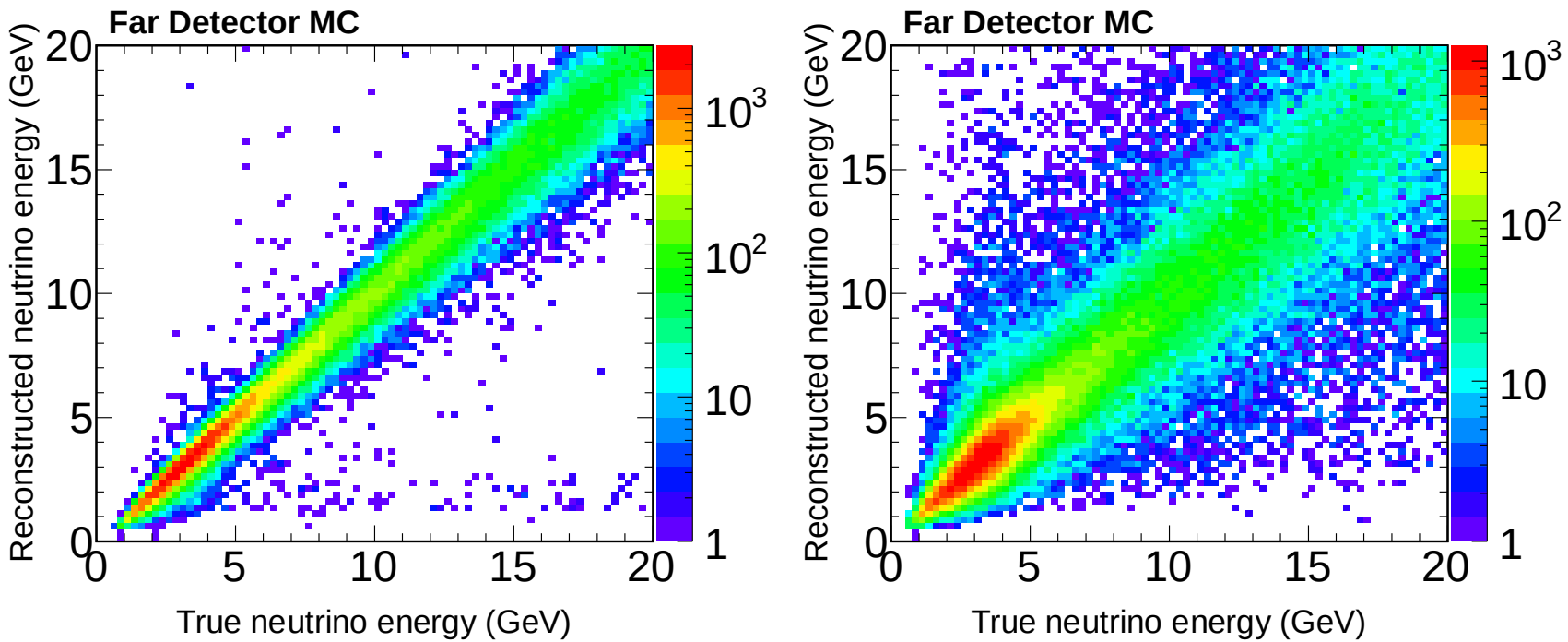

Figure 46: Smearing matrix for the 20% of events with the best (left) and worst (right) energy resolution, as simulated in the Far Detector. By separating events by resolution, we are able to better measure oscilllations without poorer-resolution events filling in the oscillation dip.

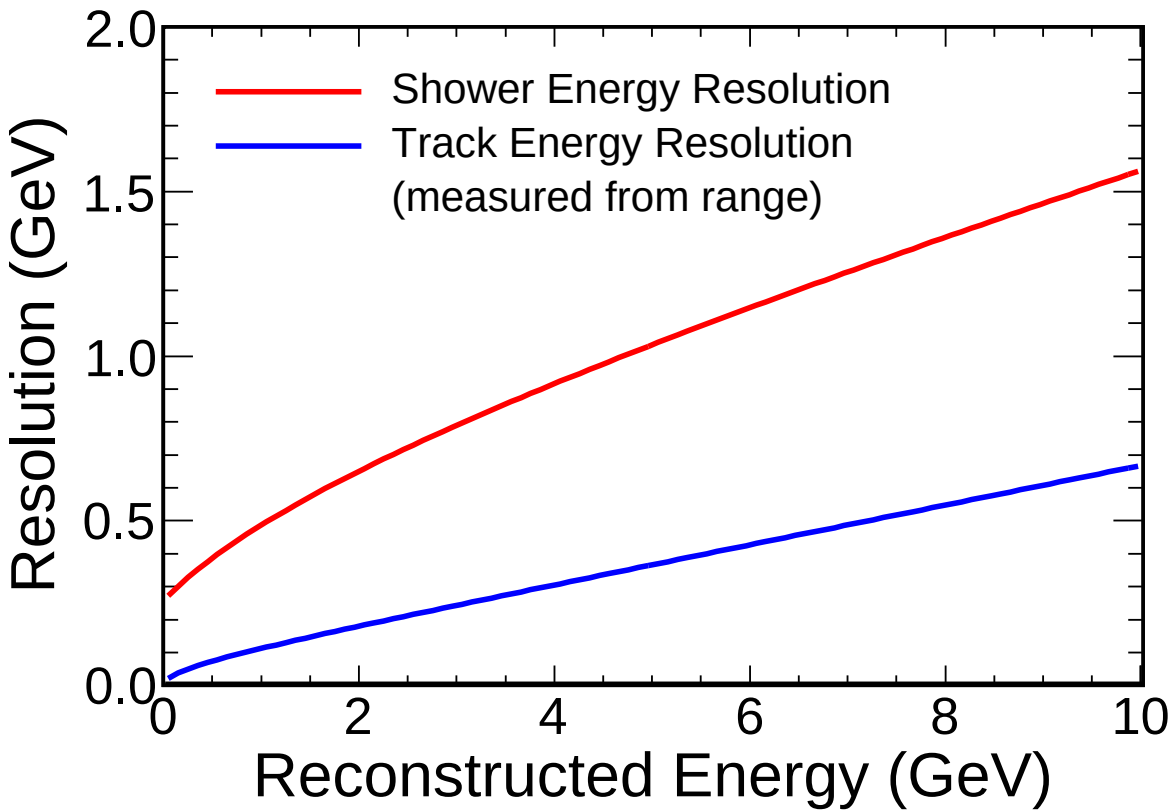

Figure 47: Resolution parameterisations for the shower energy and track energy. The latter is for events with their momentum measured from range; for events where the momentum is calculated from the track curvature, the track fitter error is used to determine the resolution. The shower and track resolutions are then combined in quadrature to determine the overall event resolution.

Resolution Parameterisations for shower and track energy (from range).

Shower Energy: $\frac{\sigma}{E} = \frac{40.4\%}{\sqrt{E}} + 8.6\% + \frac{257\ \text{MeV}}{E}$

Track Energy from Range: $\frac{\sigma}{E} = \frac{5.1\%}{\sqrt{E}} + 6.9\%$

kNN shower energy estimator

minos-doc-6868

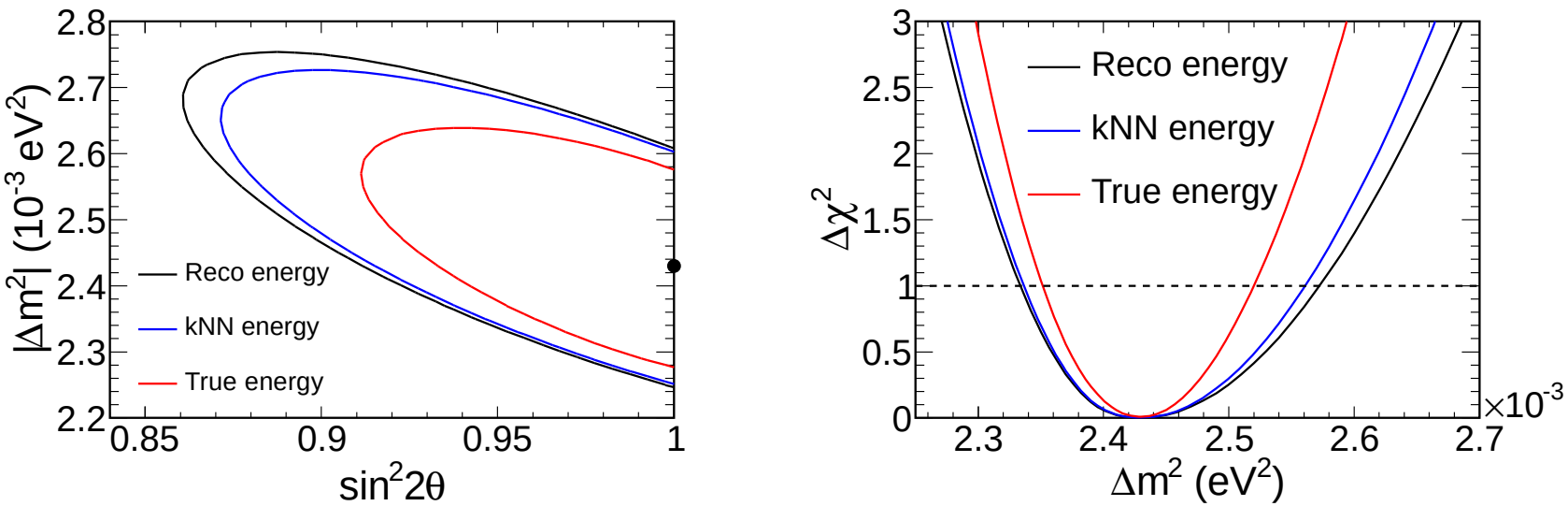

Figure 48: Left: The black contour shows our sensitivity using the current shower energy reconstruction and the blue contour shows the improvement achieved when using the best kNN found (3 variables, 400 neighbours). The red contour shows the maximum possible sensitivity in the case where we have perfect energy reconstruction. Right: Marginalization of the left plot onto the Δm^2 axis.

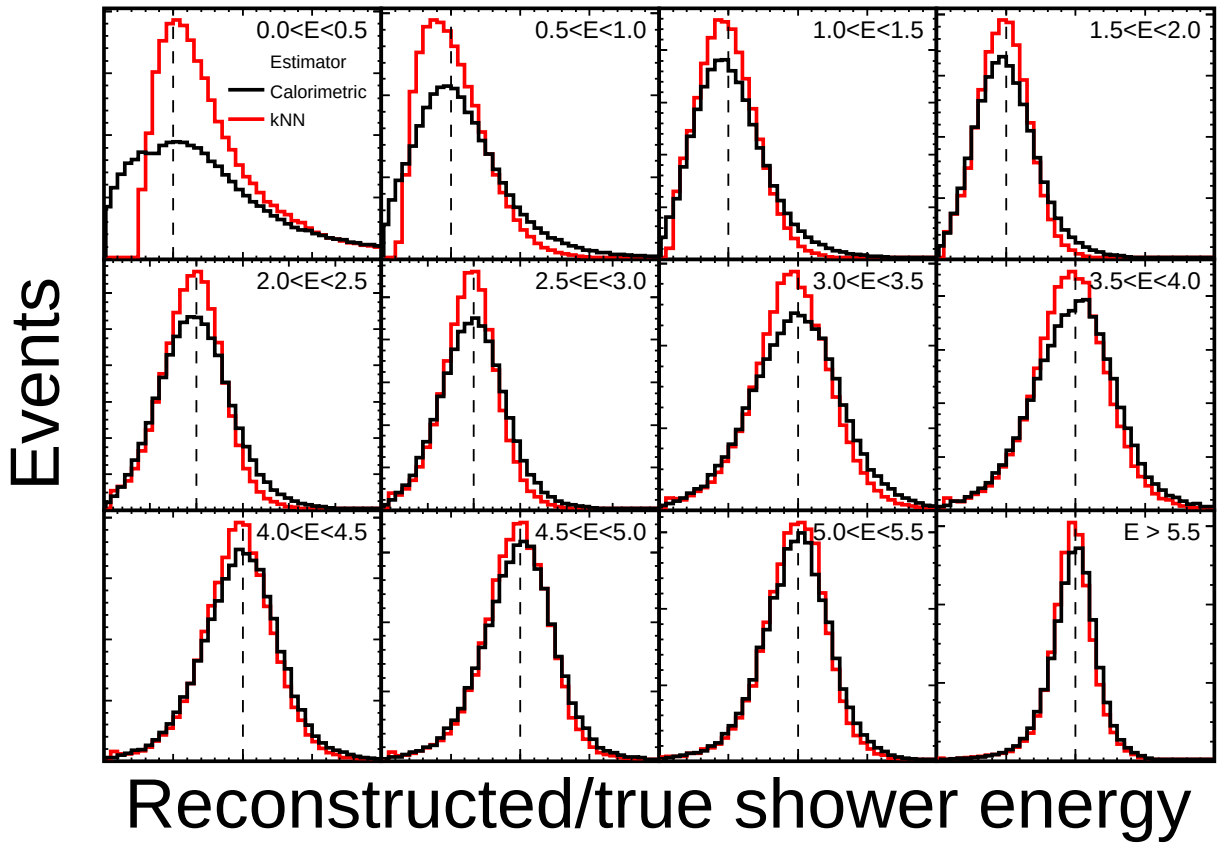

Figure 49: Distribution of $E_{\mathrm{reco}}/E_{\mathrm{true}}$ for different ranges of true shower energy. The standard reconstruction is in black, and the kNN energy estimate in red. The dotted lines mark $E_{\mathrm{reco}} = E_{\mathrm{true}}$. The kNN peak is sharper than standard reconstruction at low energies.

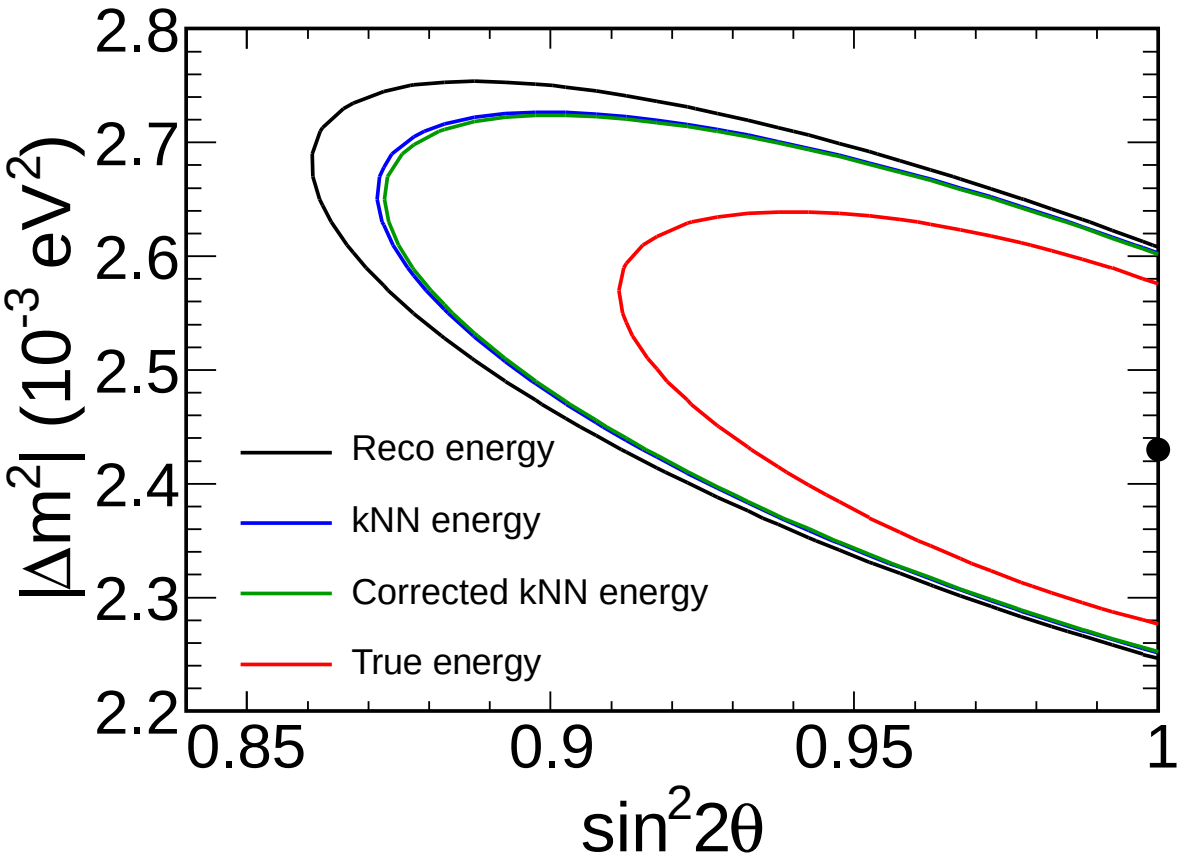

Figure 50: Additional sensitivity improvement due to energy corrections. The black, blue and red contours are as in the previous contour plot. The green contour shows the sensitivity once shower energy corrections are included.

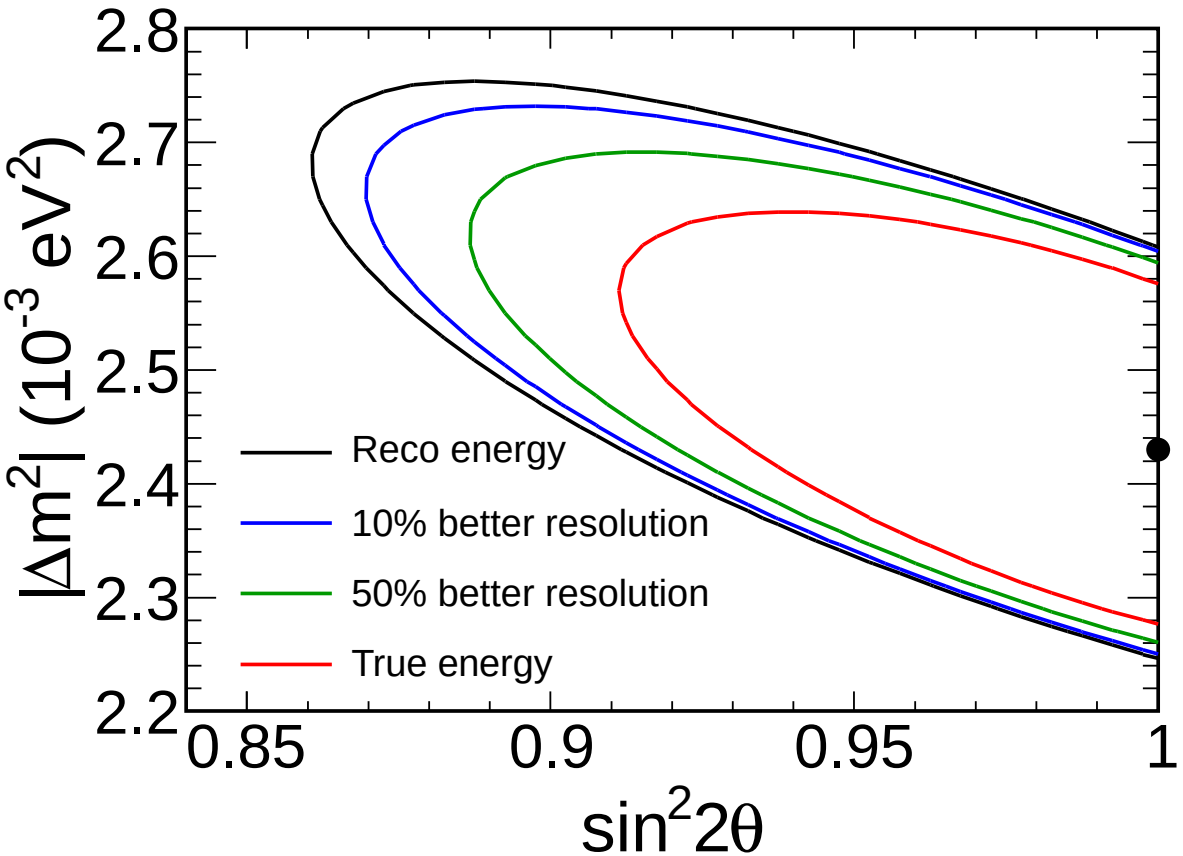

Figure 51: Sensitivity to ν_μ oscillations for 7×10^{20} POT of FHC running. The star marks the input oscillation parameters: $\Delta m^2 = 2.43 \times 10^{-3}$ eV^2, $\sin^2 2\theta = 1$. The black contour shows our current sensitivity, and the red contour the sensitivity we would have if we knew the true energy of every event. The blue and green contours show the effect of successive improvements to the energy resolution: the difference in the reconstructed energy of each event from the true energy is reduced by a factor 1.1 or 1.5. Even in the case of a 10% improvement the difference is clearly visible.

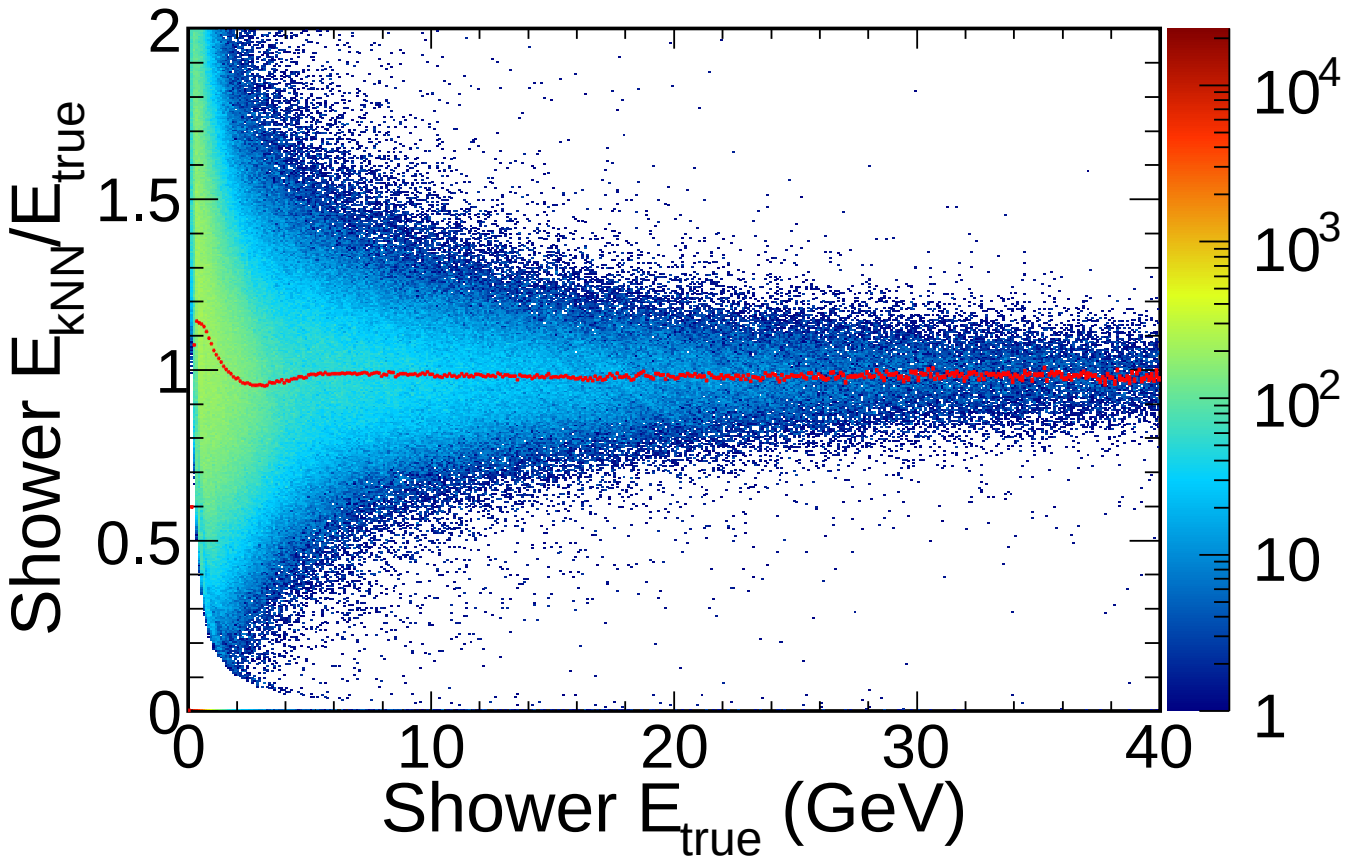

Figure 52: kNN over true shower energy for all CC-selected events versus true shower energy. The red markers show the mean value of the kNN over true ratio in each true energy bin. A significant energy bias can be seen below $\sim 6\ \mathrm{GeV}$. Above $\sim 2\ \mathrm{GeV}$ the kNN estimates are too low, and below $\sim 2\ \mathrm{GeV}$ they are too high.

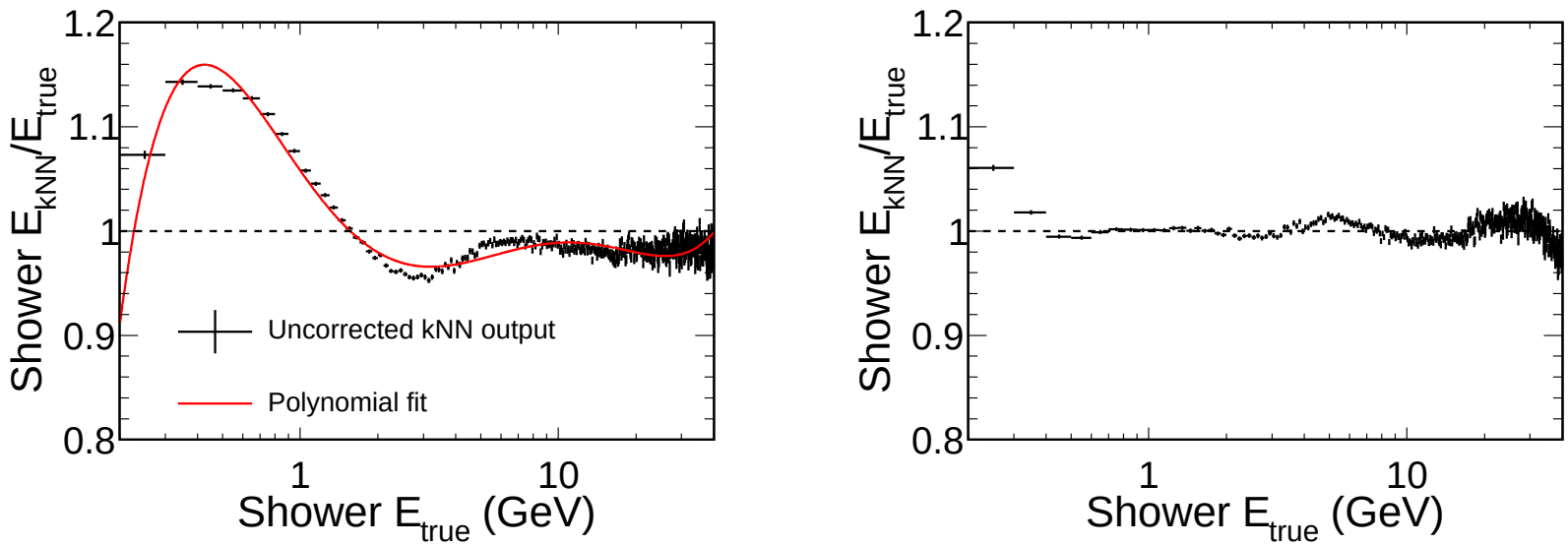

Figure 53: The mean value of kNN shower energy over true shower energy, plotted as a function of true shower energy. The x scale is logarithmic. Left: the distribution from the uncorrected kNN output, with a polynomial fit – the first iteration of three in the correction process. Right: the same distribution after all corrections have been applied.

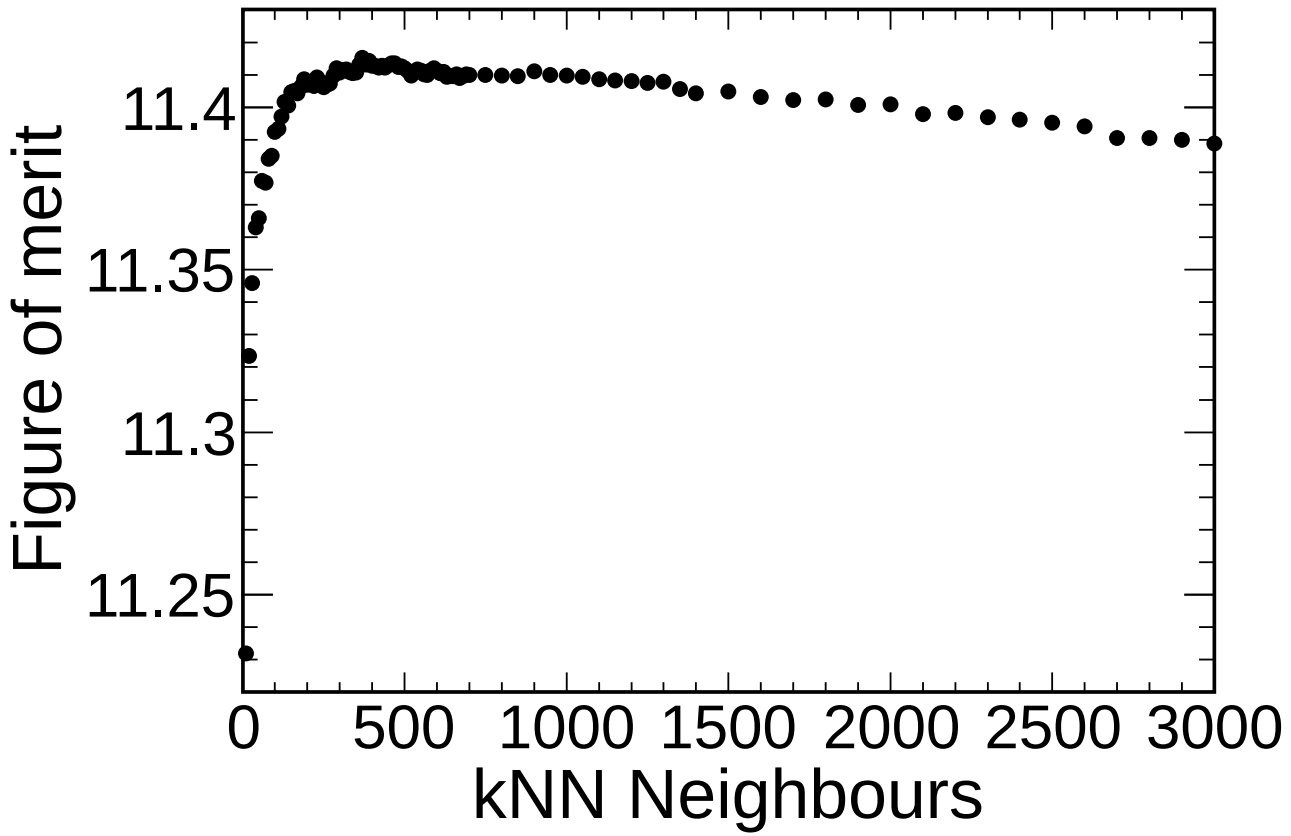

Figure 54: Variation of the figure of merit (log-likelihood difference between $\Delta m^2 = 2.43 \times 10^{-3}$ eV^2 and $\Delta m^2 = 2.7 \times 10^{-3}$ eV^2) against number of neighbours used. The figure of merit increases rapidly with increasing number of neighbours, is essentially flat between approximately 300 and 500 neighbours and eventually falls gradually at high numbers of neighbours. The small-scale variations are due to statistical fluctuations in the training sample.

Systematics star plots

minos-doc-6874

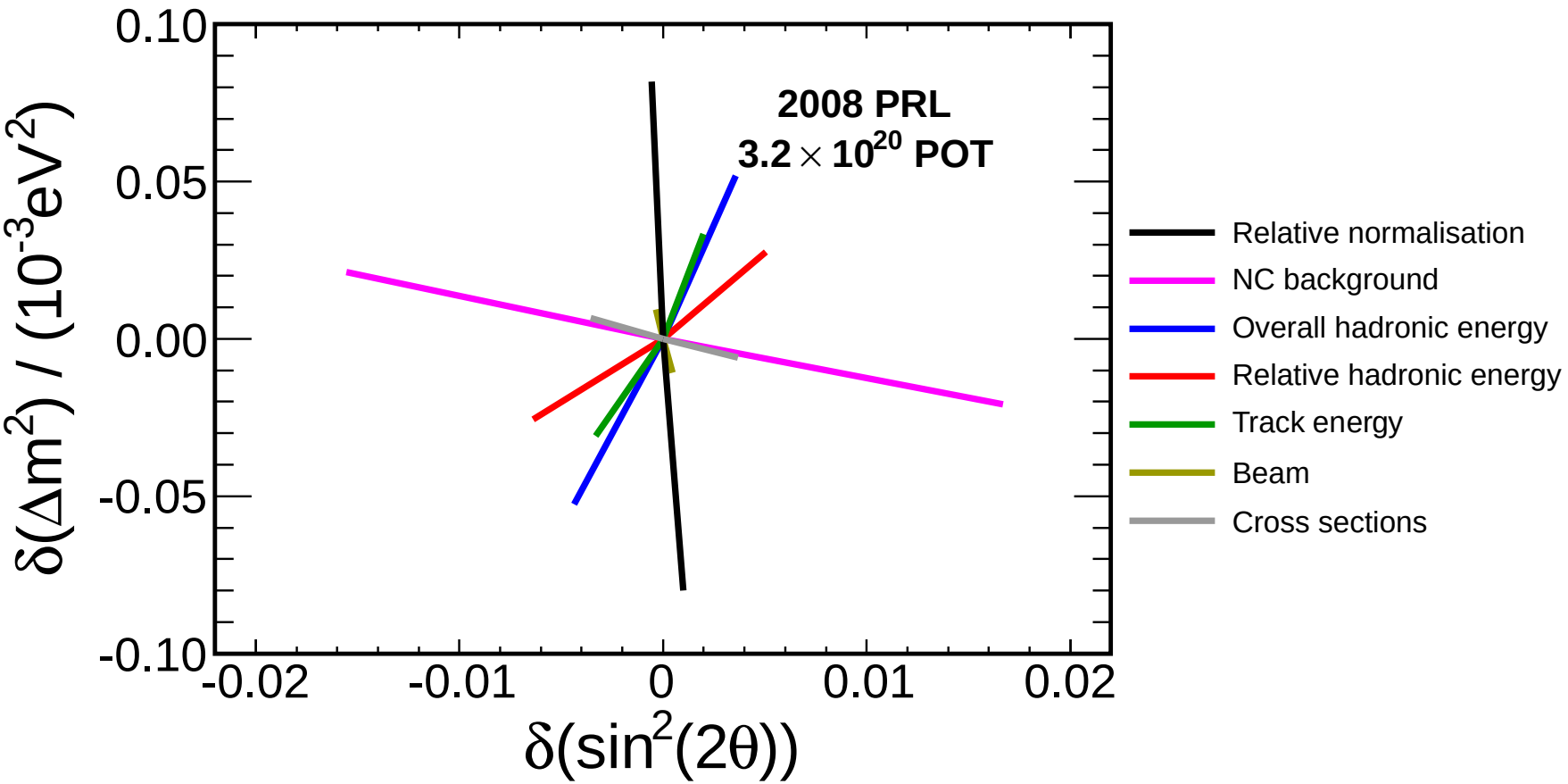

Figure 55: The shifts to the best fit oscillation parameters (the fit unconstrained) induced by the application of systematic shifts to the fake data. Shown here are the errors published in 2008 for a smaller exposure.

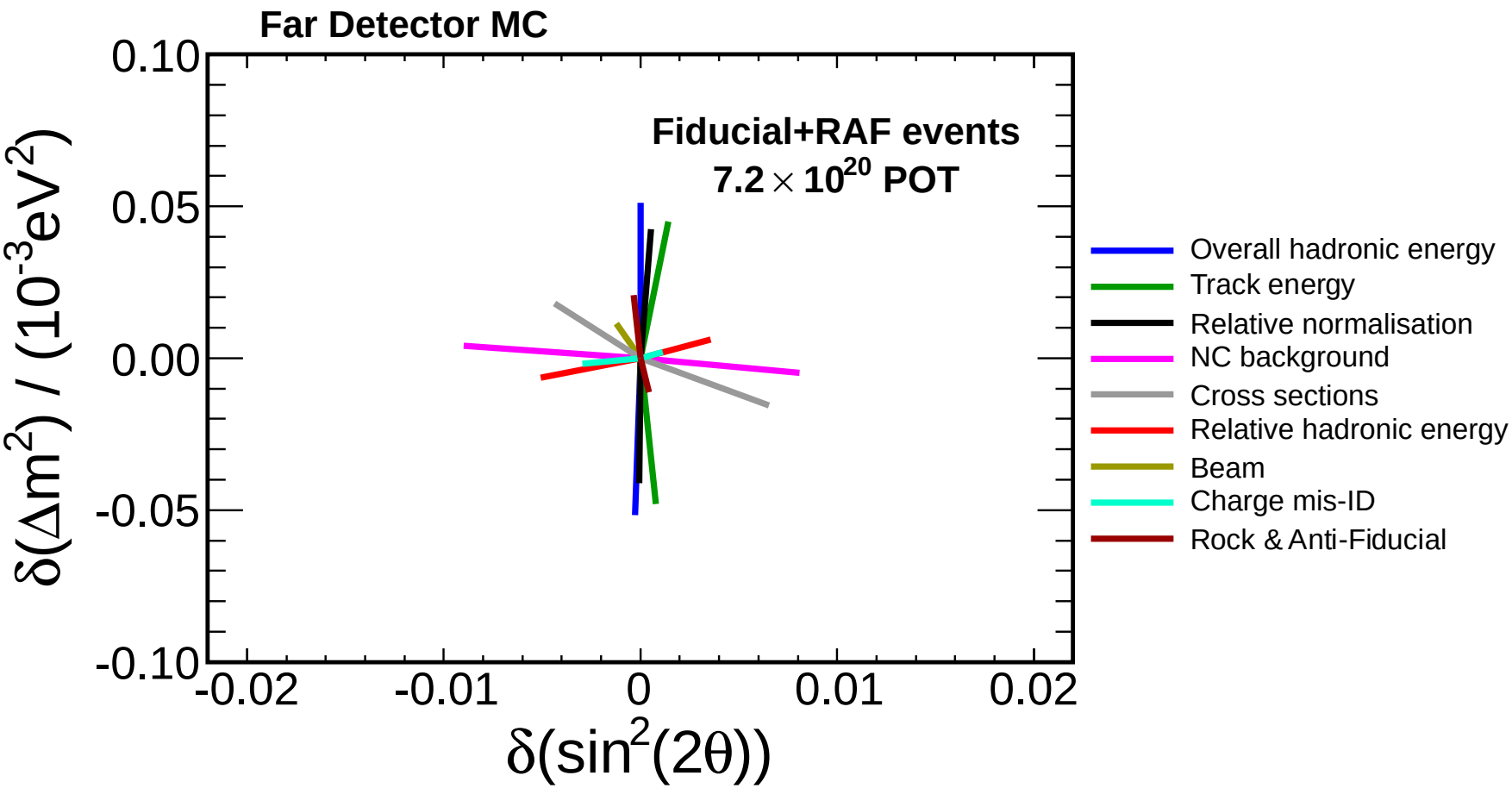

Figure 56: The shifts to the best fit oscillation parameters (the fit unconstrained) induced by the application of systematic shifts to the fake data. Shown are are shifts to the fit of fiducial events and RAF events.

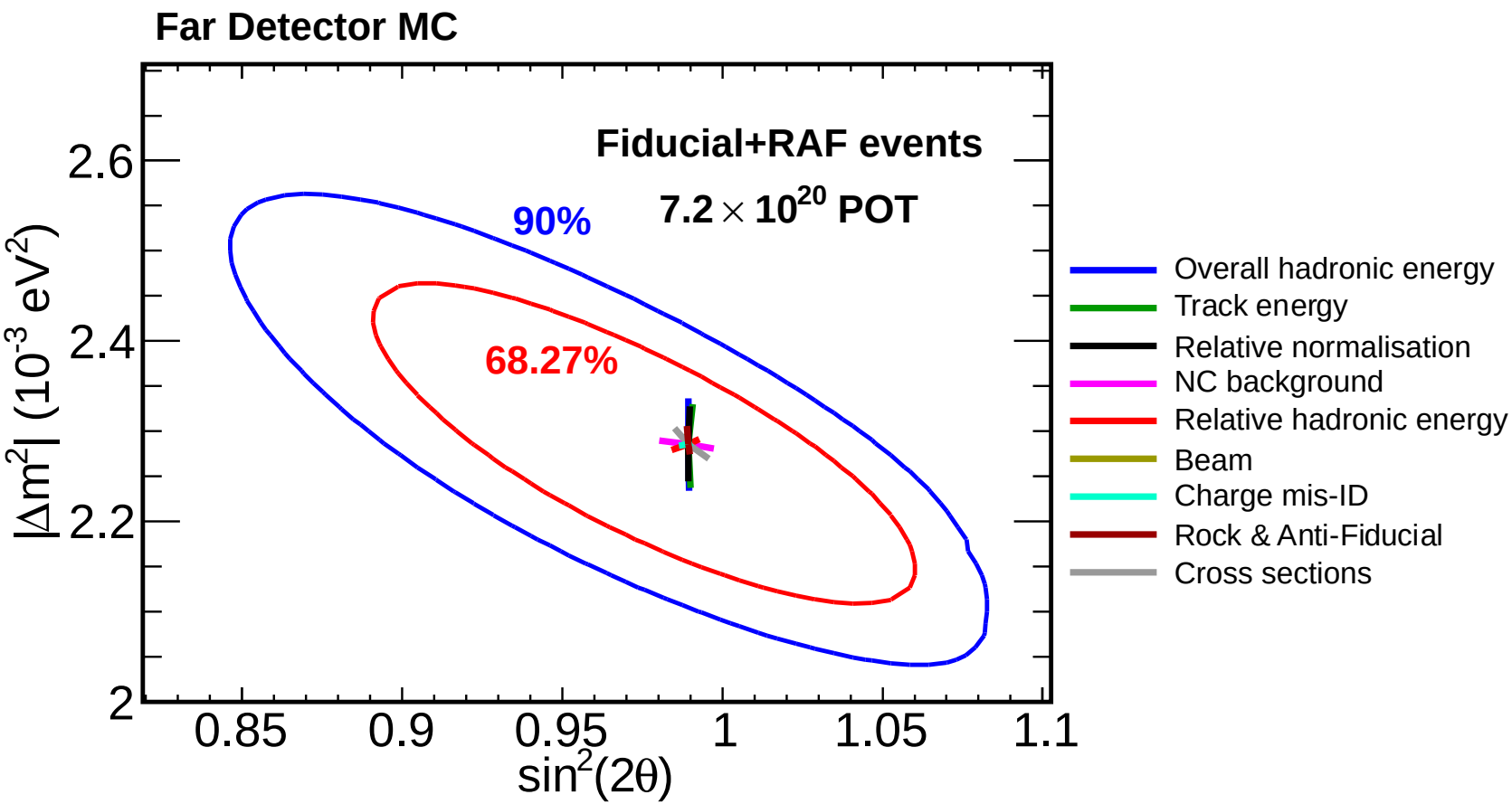

Figure 57: The shifts to the best fit oscillation parameters (the fit unconstrained) induced by the application of systematic shifts to the fake data. Shown are are shifts to the fit of fiducial events and RAF events. Star is placed at best fit point for fiducial-only fit, which is why this appears asymmetric.

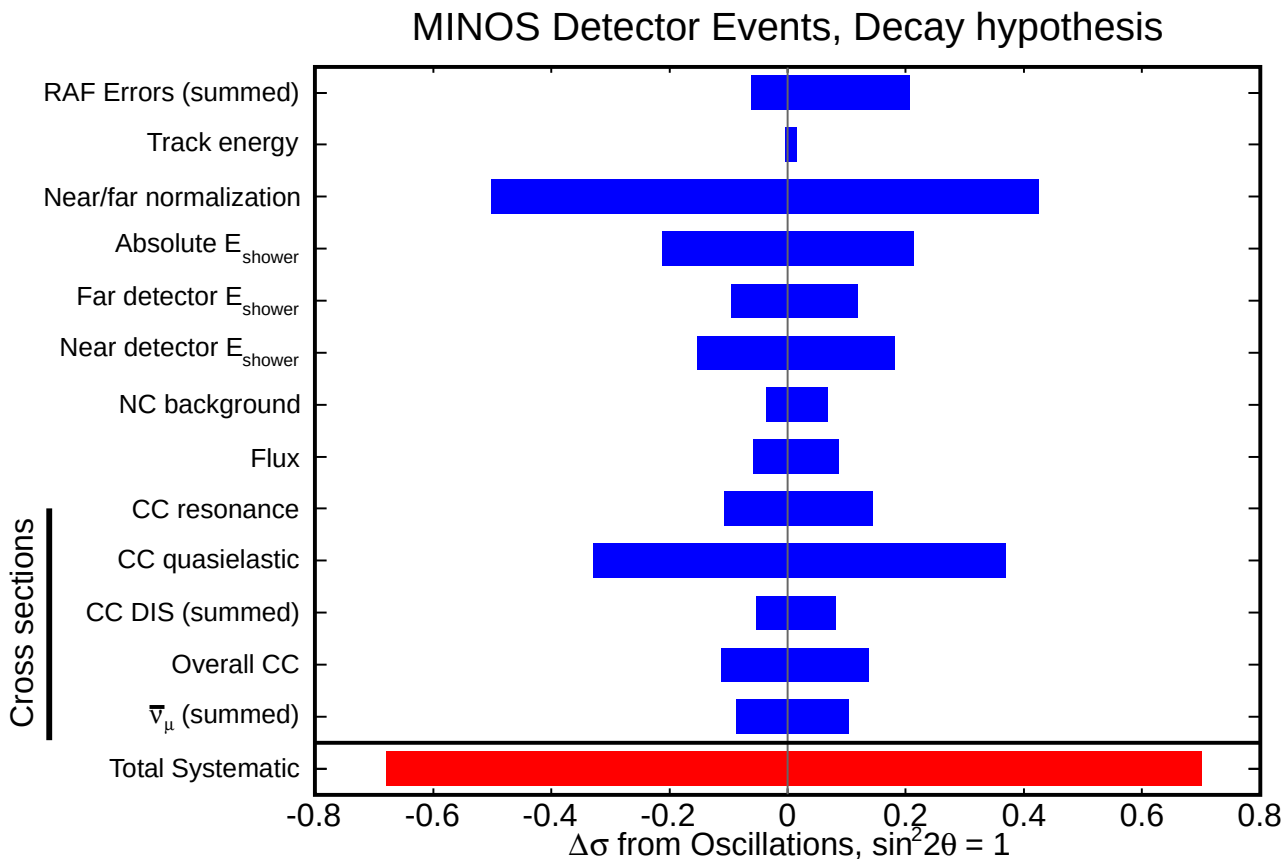

Figure 58: Systematic uncertainty on the exclusion of the pure neutrino decay disappearance model for the combined analysis of fiducial events and partially-contained events.

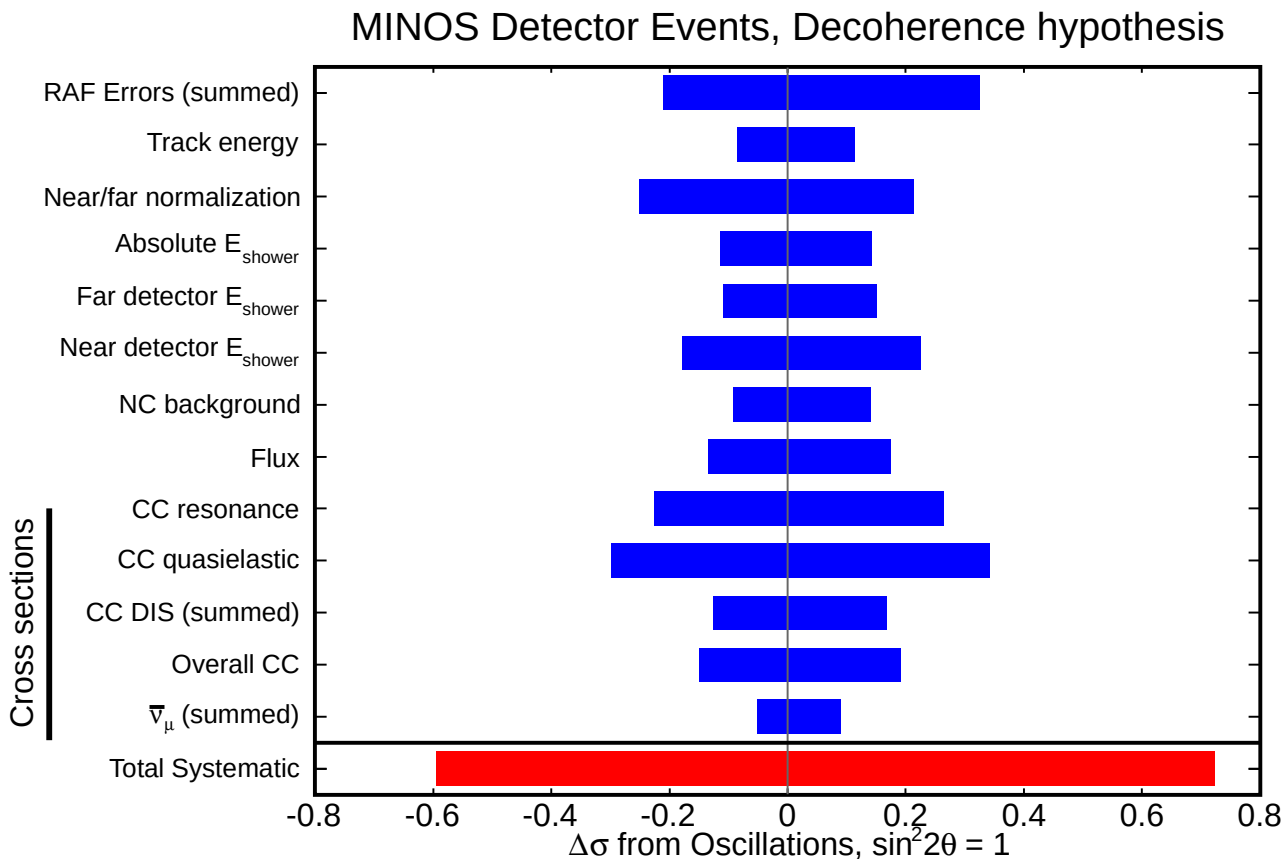

Figure 59: Systematic uncertainty on the exclusion of the pure neutrino decoherence disappearance model for the combined analysis of fiducial events and partially-contained events.

Shift	Amount	7.2×10^{20}POT Fiducial		7.2×10^{20}POT Fiducial+RAF	
		$\delta(\Delta m^2)$	$\delta(\sin^2(2\theta_{23}))$	$\delta(\Delta m^2)$	$\delta(\sin^2(2\theta_{23}))$
Shower Energy	1σ	0.049	0.001	0.051	0.000
Rel. Shower Energy	$1.9\%/1.1\%$	0.008	0.004	0.006	0.004
Norm.	1.6%	0.030	0.001	0.041	0.000
NC Bknd.	20%	0.008	0.008	0.005	0.009
μ Momentum	$2\%/3\%$	0.038	0.001	0.048	0.001
σ_ν (sum in quadrature)	1σ	0.007	0.004	0.017	0.006
Beam	1σ	0.009	0.000	0.014	0.001
$\overline{\nu}_\mu$ wrong-sign	30%	0.003	0.002	0.002	0.002
RAF only	1σ	-	-	0.006	0.000
Total		0.071	0.010	0.085	0.012

Table 1: Current systematic errors and the shifts in best fit values of Δm^2 and $\sin^2(2\theta)$ they induce. Relative shower energy is 1.9% ND, 1.1% FD. μ momentum is 2% range, 3% curvature. Other 1σ shifts are either energy dependent or uncorrelated sums of several errors.

Shift	2008 PRL Fiducial		7.2×10^{20}POT Fiducial		7.2×10^{20}POT Fiducial+RAF	
	$\delta(\Delta m^2)$	$\delta(\sin^2(2\theta_{23}))$	$\delta(\Delta m^2)$	$\delta(\sin^2(2\theta_{23}))$	$\delta(\Delta m^2)$	$\delta(\sin^2(2\theta_{23}))$
Shower Energy	0.052	0.004	0.049	0.001	0.051	0.000
Rel. Shower Energy	0.027	0.006	0.008	0.004	0.006	0.004
Norm. $(4\% \rightarrow 1.6\%)$	0.081	0.001	0.030	0.001	0.041	0.000
NC Bknd. $(50\% \rightarrow 20\%)$	0.021	0.016	0.008	0.008	0.005	0.009
μ Momentum	0.032	0.003	0.038	0.001	0.048	0.001
σ_ν (sum in quadrature)	0.006	0.004	0.007	0.004	0.017	0.006
Beam	0.010	0.000	0.009	0.000	0.014	0.001
$\overline{\nu}_\mu$ wrong-sign	-	-	0.003	0.002	0.002	0.002
RAF only	-	-	-	-	0.006	0.000
Total	0.104	0.017	0.071	0.010	0.085	0.012

Table 2: The evolution of systematic errors from the 3.2×10^{20} POT dataset published in 2008 to the current analysis, including new systematic errors associated with new samples included in the analysis

Sensitivities

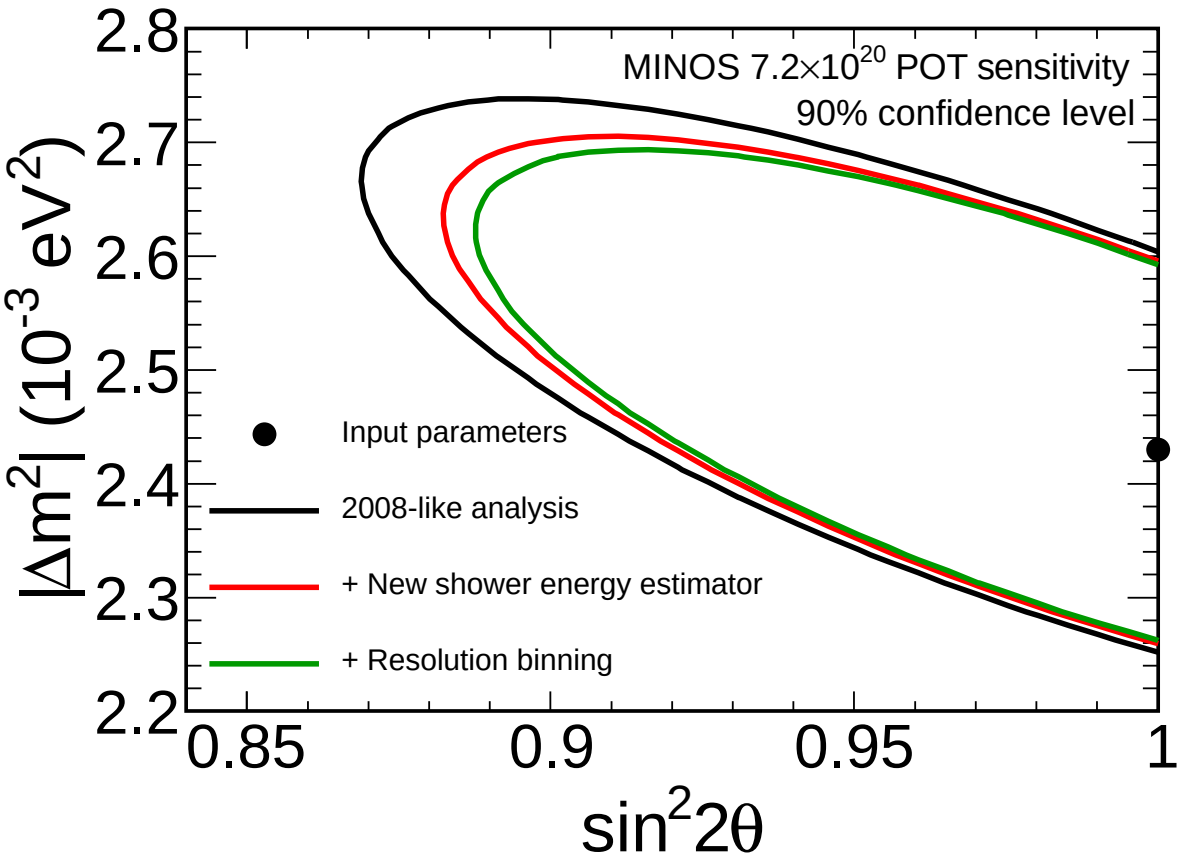

Figure 60: Sensitivity improvement from successive analysis improvements: kNN energy and resolution binning.

The fake data in these fits is based on extrapolated near detector data.

“2008-like” already includes reconstruction changes and positively-charged events.

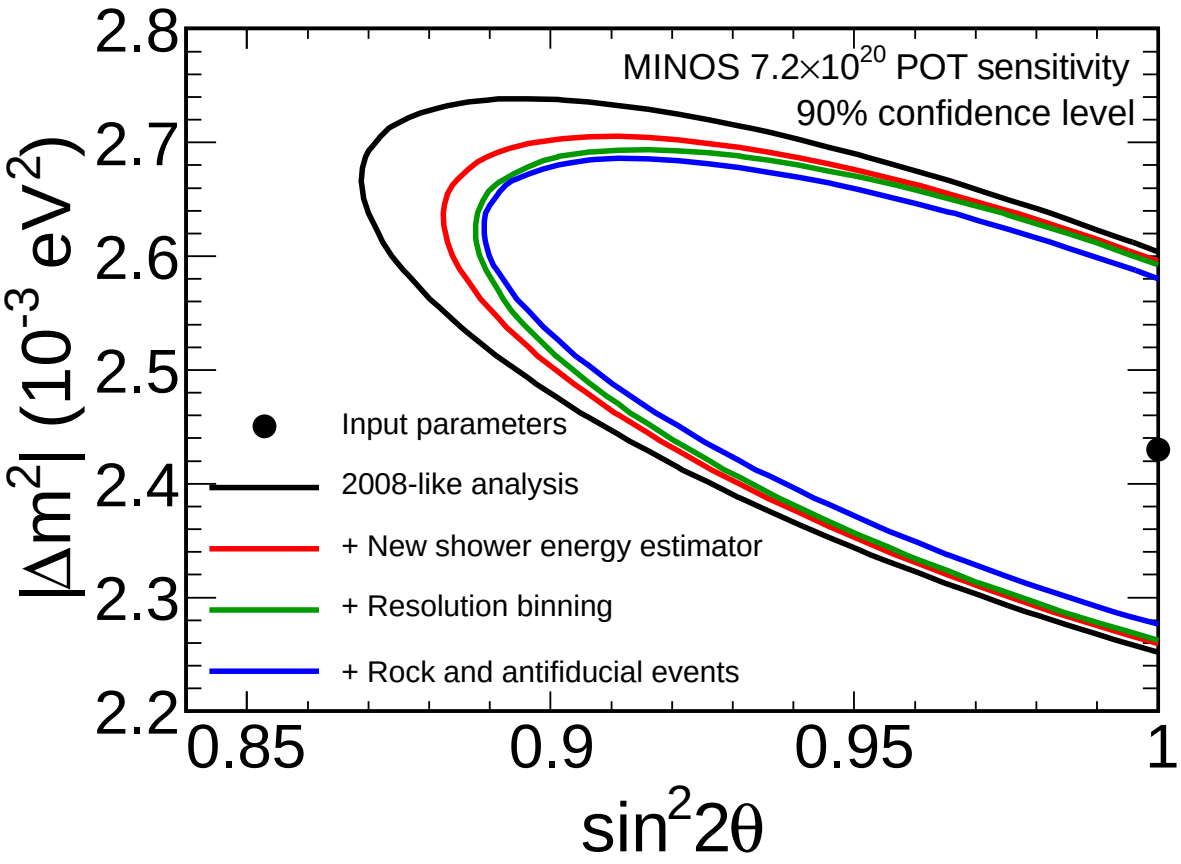

Figure 61: Sensitivity improvement from successive analysis improvements: kNN energy, resolution binning, inclusion of RAF events.
The fake data in these fits is based on extrapolated near detector data.
“2008-like” already includes reconstruction changes and positively-charged events.

Energy spectra

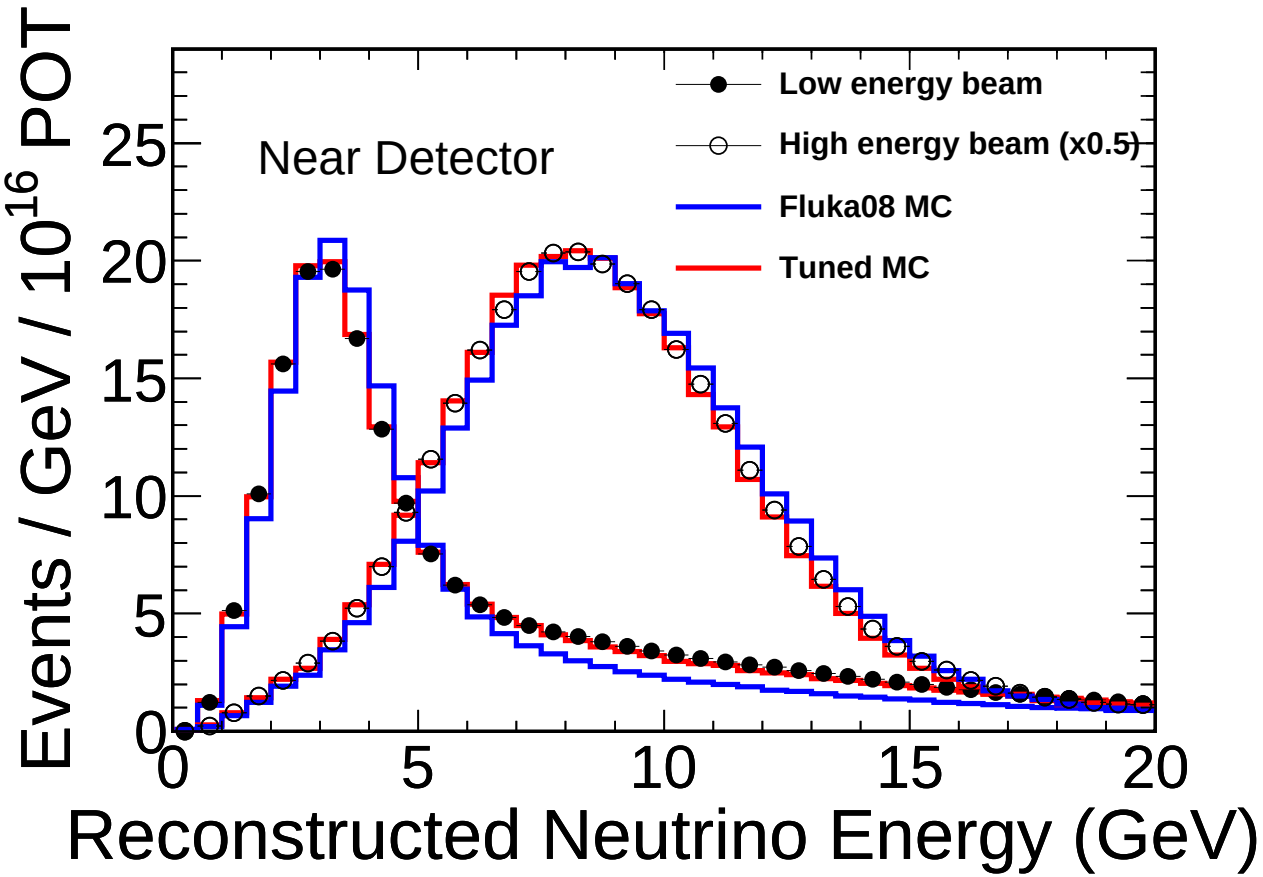

Figure 62: ND LE-10 and pHe reconstructed neutrino energy spectrum with and without beam reweighting.

Resolution Bin	Unoscillated Prediction	Data
LE Run1	413.46	318
LE Run2	639.21	511
LE Run3	1251.63	1037
pHE	134.11	120
Total LE	2304.30	1866
Total pHE	134.11	120

Table 3: Expected event counts and measured event counts for Runs I, II, III, and pHE separately.

	Unoscillated Prediction		7.2×10^{20} POT Fiducial Data	
Resolution Bin	Events < 5 GeV	Events < 10 GeV	Events < 5 GeV	Events < 10 GeV
Bin0	196.5	284.9	131	208
Bin1	196.9	285.2	108	184
Bin2	197.3	284.6	82	173
Bin3	197.8	284.5	112	188
Bin4	198.4	285.0	137	213
Positive Curavture	64.9	77.3	54	118
Total	1051.8	1501.5	624	1084

Table 4: Expected and measured events within different energy ranges for Runs I, II, III, and pHE. 7.2×10^{20} POT.

Resolution Bin	NC Bknd. Expectation	Rock Bknd. Expectation
Bin 0	0.09	4.96
Bin 1	0.27	0.79
Bin 2	0.65	0.36
Bin 3	6.33	0.38
Bin 4	12.6	0.50
Positive Curvature	21.1	1.11
Total	41.0	8.1

Table 5: Expected backgrounds in each resolution bin for Runs I, II, III, and pHE, a total of 7.2×10^{20} POT.

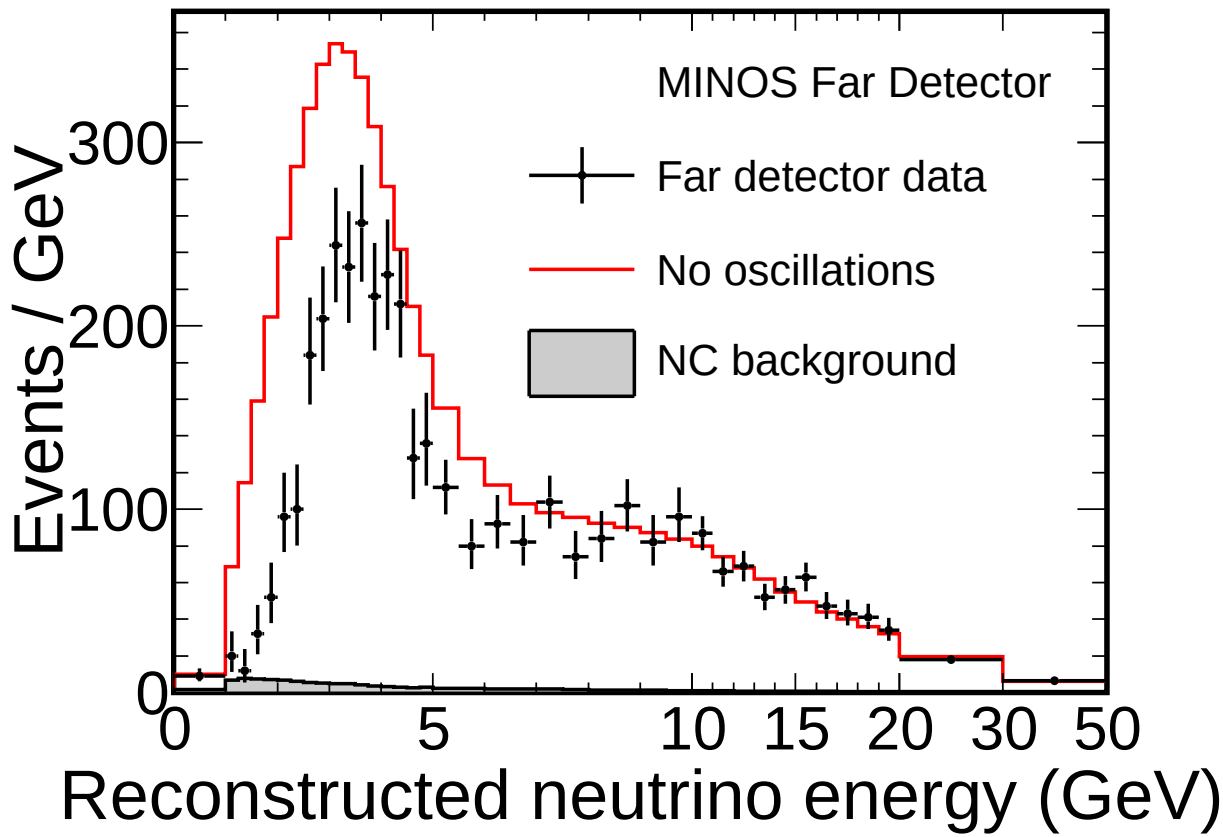

Figure 63: Comparison of MINOS far detector data (sum of all fiducial samples) with the unoscillated prediction (red).

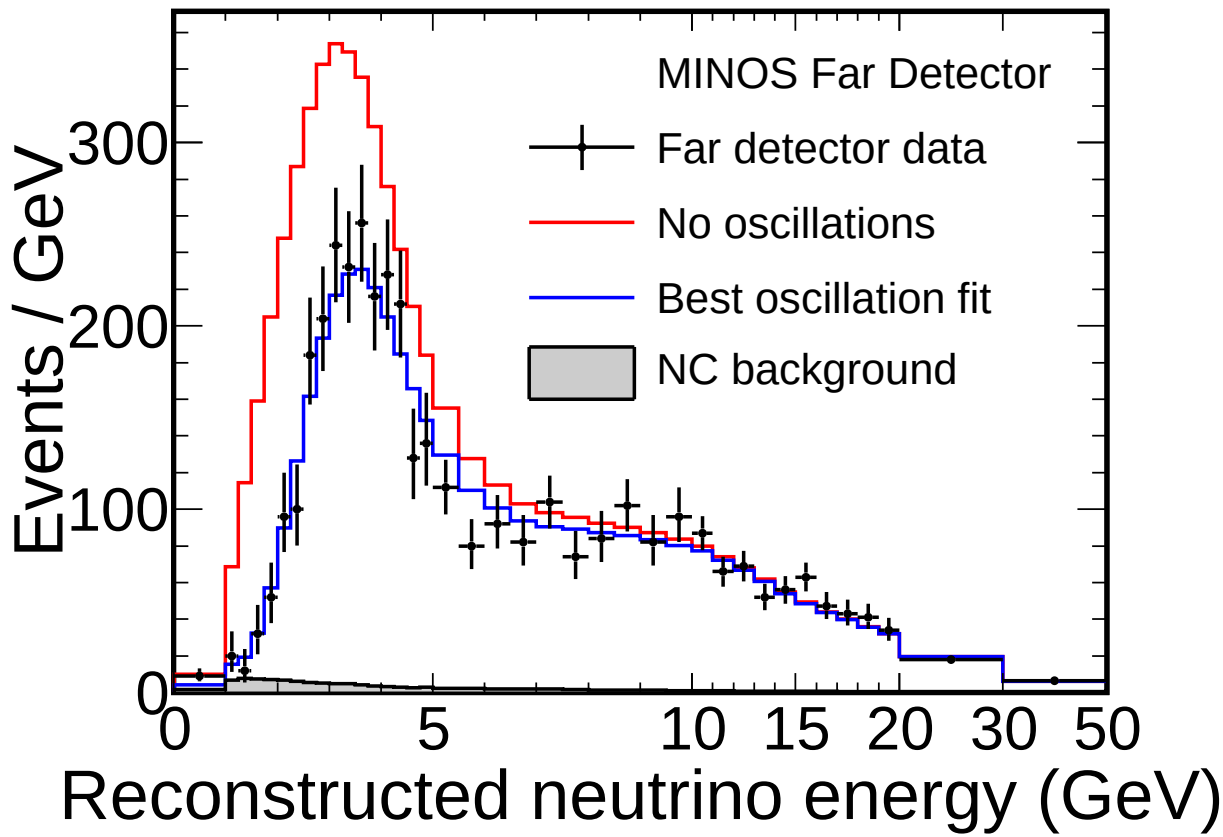

Figure 64: Comparison of MINOS far detector data (sum of all fiducial samples) with the unoscillated prediction (red) and the best fit to oscillations (blue).

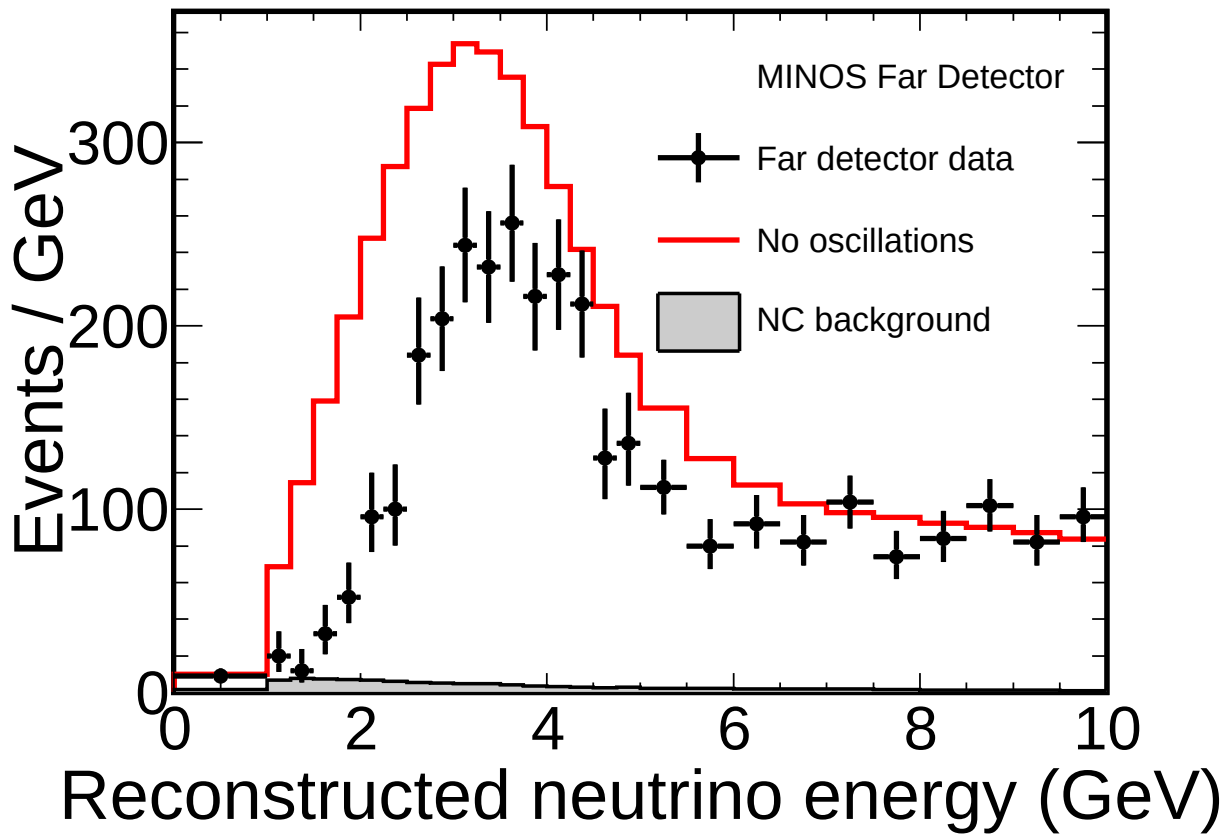

Figure 65: Comparison of MINOS far detector data (sum of all fiducial samples) with the unoscillated prediction (red). Zoomed to the oscillation region.

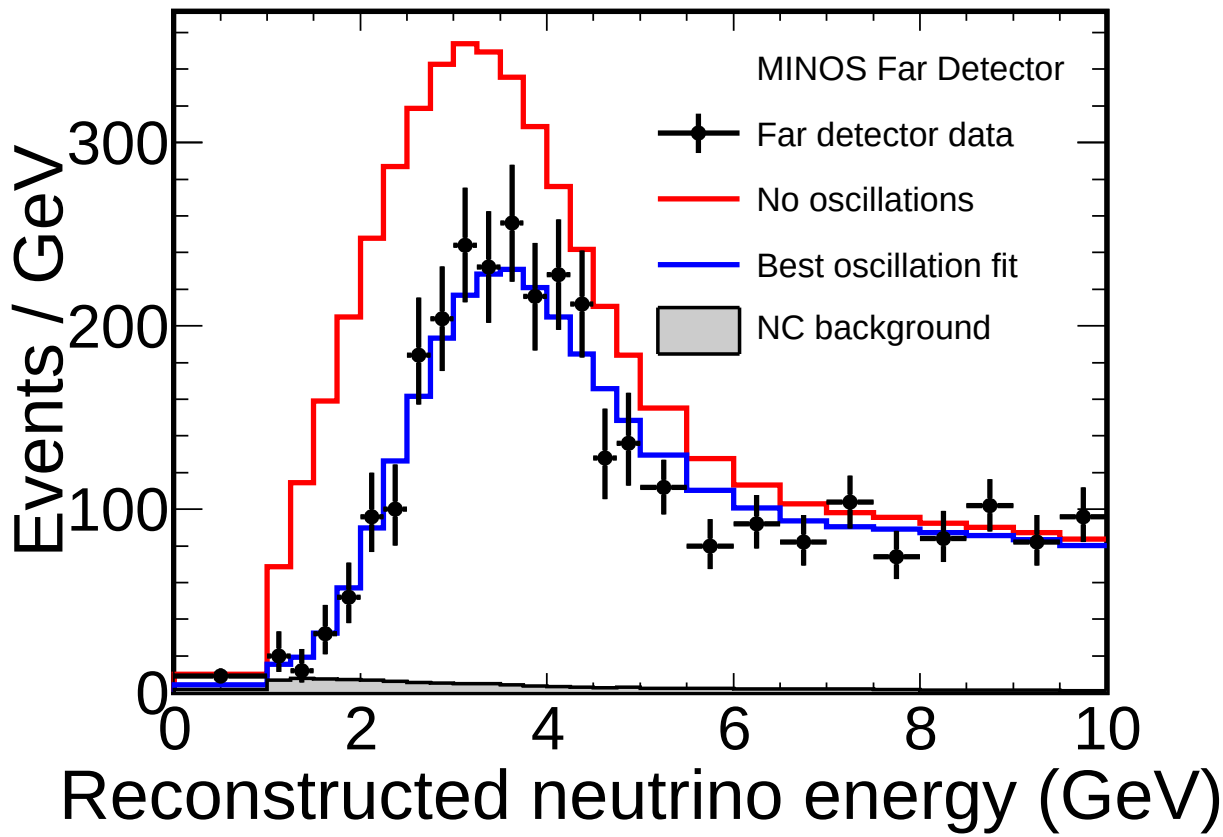

Figure 66: Comparison of MINOS far detector data (sum of all fiducial samples) with the unoscillated prediction (red) and the best fit to oscillations (blue). Zoomed to the oscillation region.

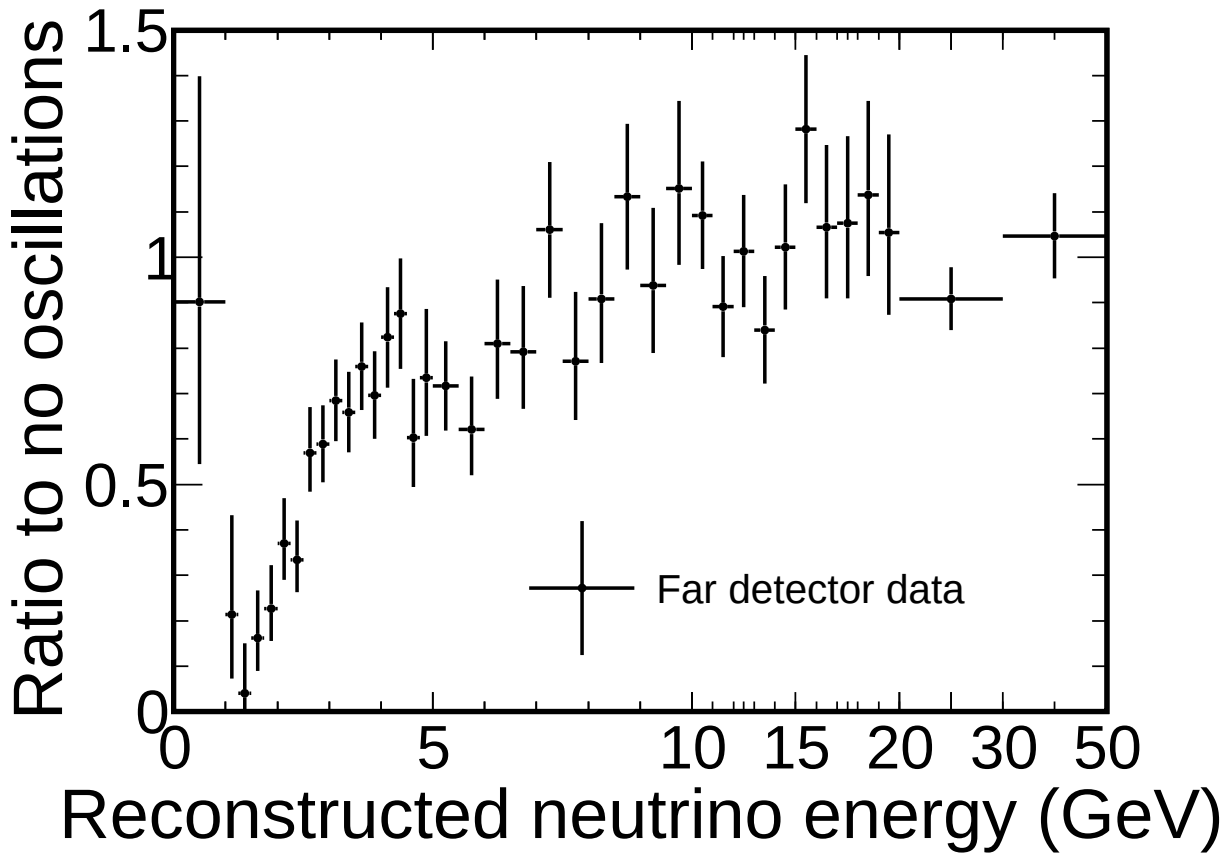

Figure 67: Ratio of the Far Detector data energy spectrum to the unoscillated prediction (both data and prediction have had the predicted Neutral Current background subtracted).

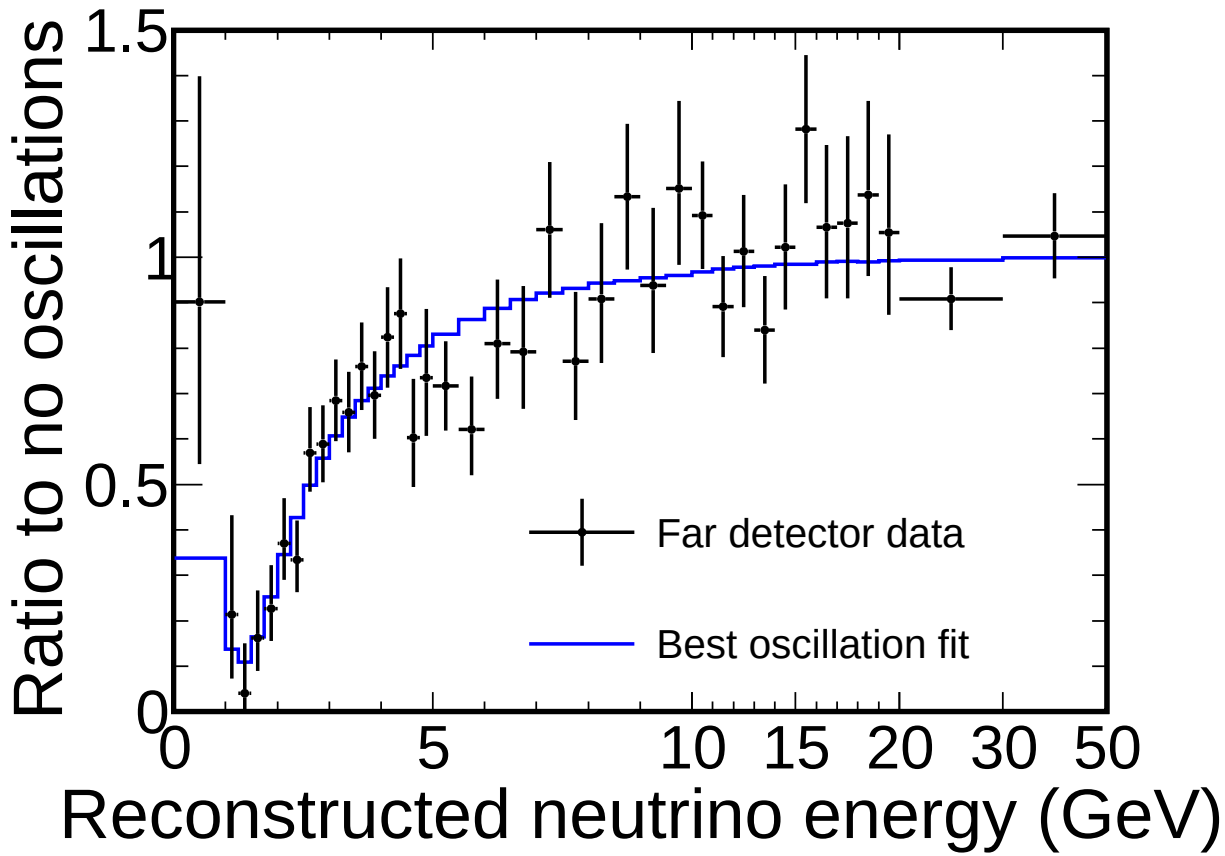

Figure 68: Ratio of the Far Detector data energy spectrum to the unoscillated prediction (both data and prediction have had the predicted Neutral Current background subtracted).

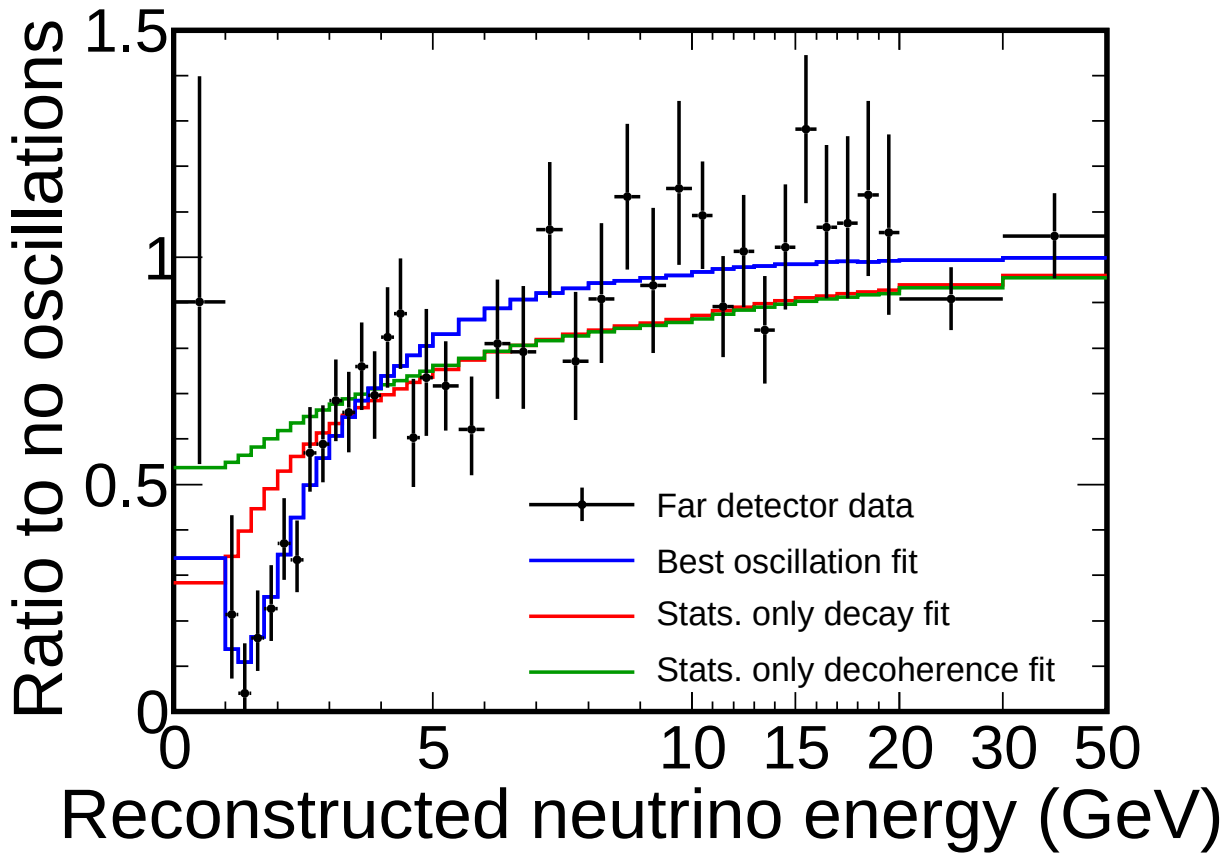

Figure 69: Ratio of the Far Detector data energy spectrum to the unoscillated prediction (both data and prediction have had the predicted Neutral Current background subtracted). The decay and decoherence fits are stats only.

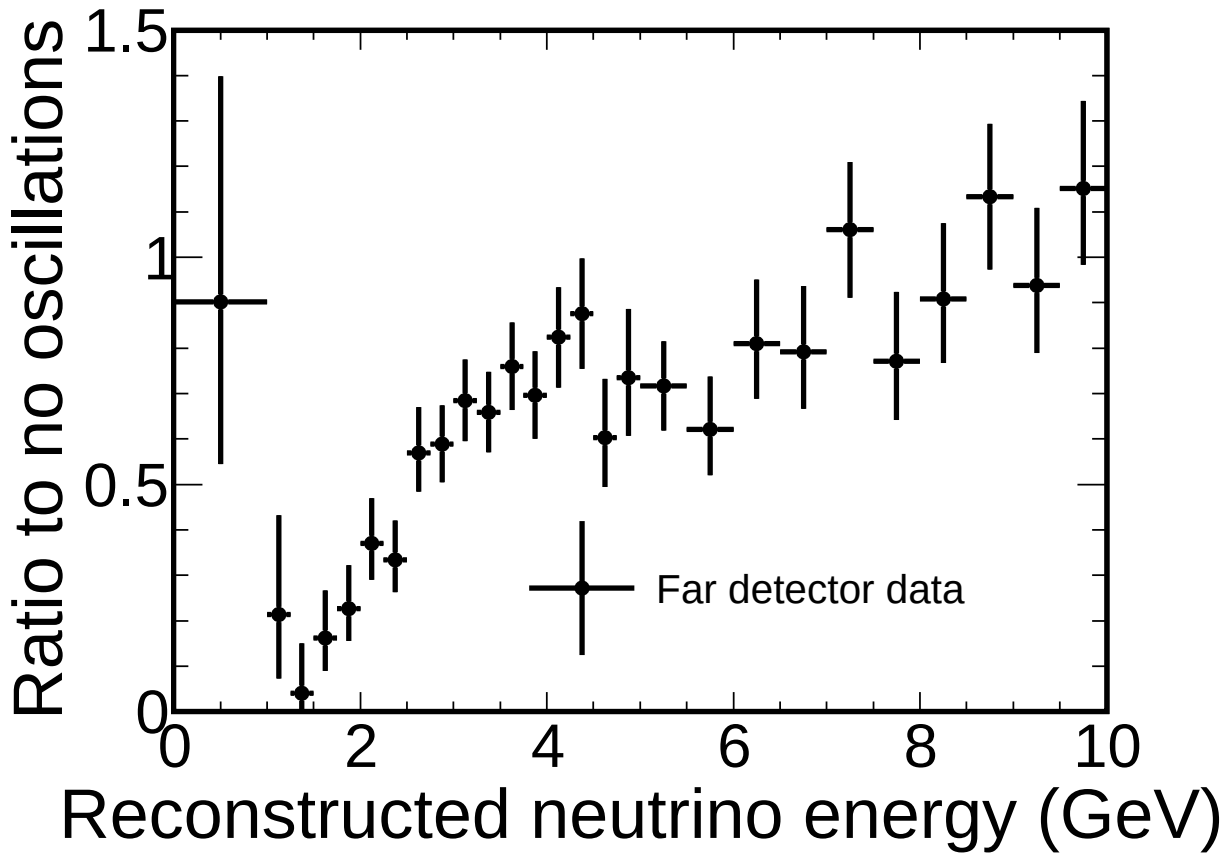

Figure 70: Ratio of the Far Detector data energy spectrum to the unoscillated prediction (both data and prediction have had the predicted Neutral Current background subtracted). Zoomed to the oscillation region.

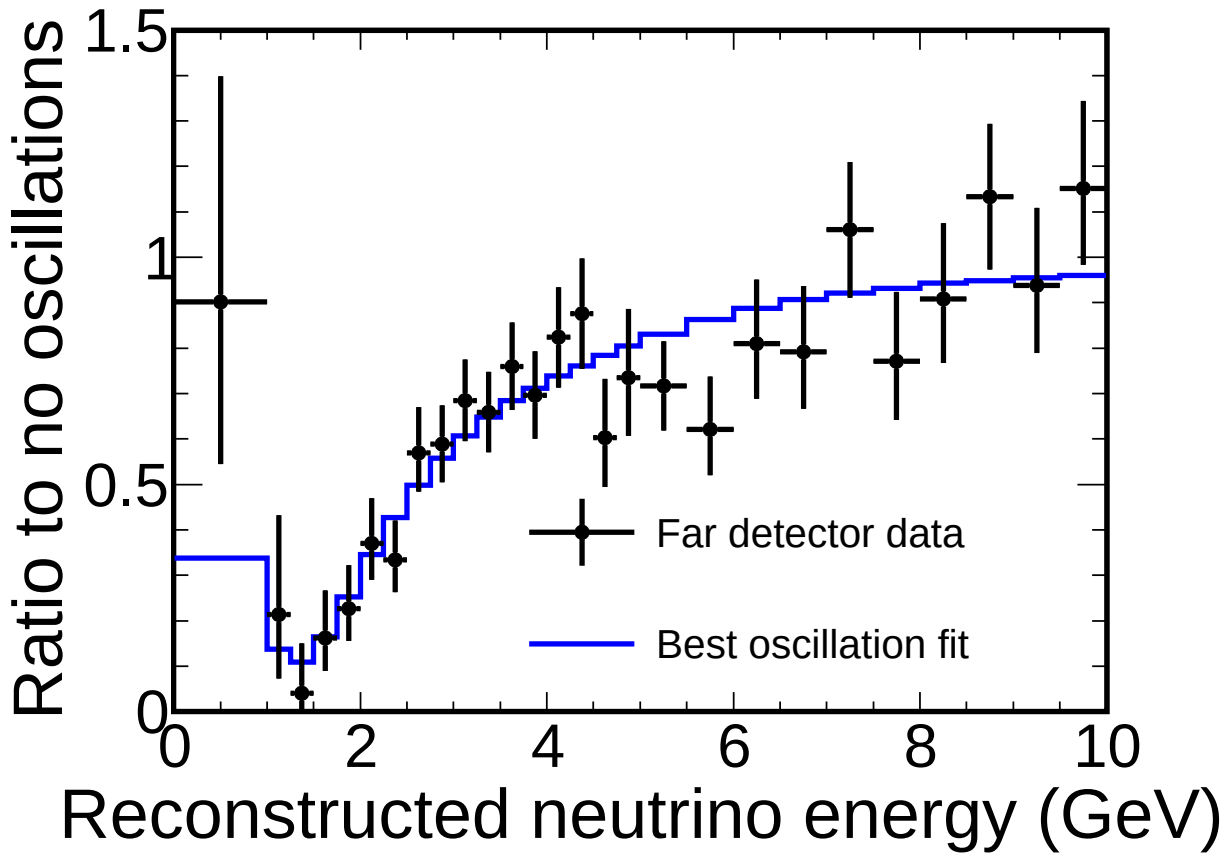

Figure 71: Ratio of the Far Detector data energy spectrum to the unoscillated prediction (both data and prediction have had the predicted Neutral Current background subtracted). Zoomed to the oscillation region.

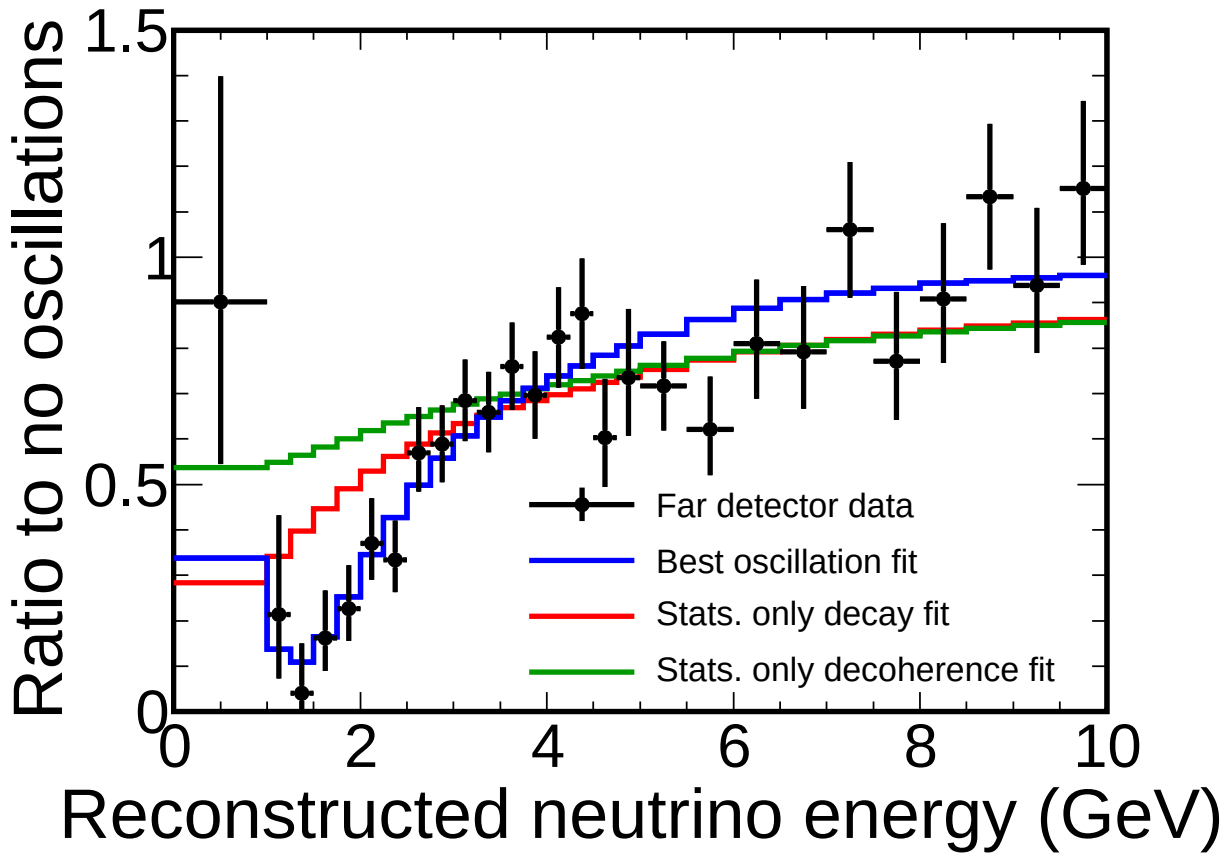

Figure 72: Ratio of the Far Detector data energy spectrum to the unoscillated prediction (both data and prediction have had the predicted Neutral Current background subtracted). Zoomed to the oscillation region. The decay and decoherence lines are stats only fits.

Contours

Likelihood surface

The fiducial likelihood surface (including the effect of systematics) is available from CVS in the file Contrib/evans/CC2010/BlessedPlots/Contours/CCLikelihoodSurface.root

It contains two histograms:

- `hLogLikelihoodSurface`: The absolute likelihood surface.
- `hDeltaLogLikelihoodSurface`: The delta likelihood surface, with respect to the best fit point.

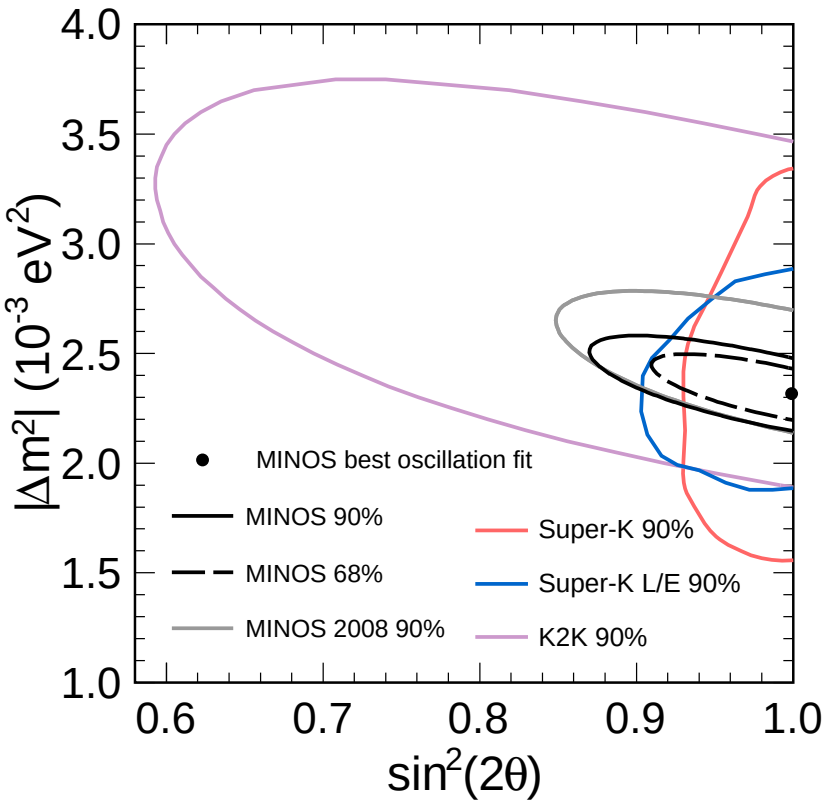

Figure 73: Comparison of MINOS fiducial+raf contours with previous MINOS, Super-K and K2K results. Conference style plot with colour.

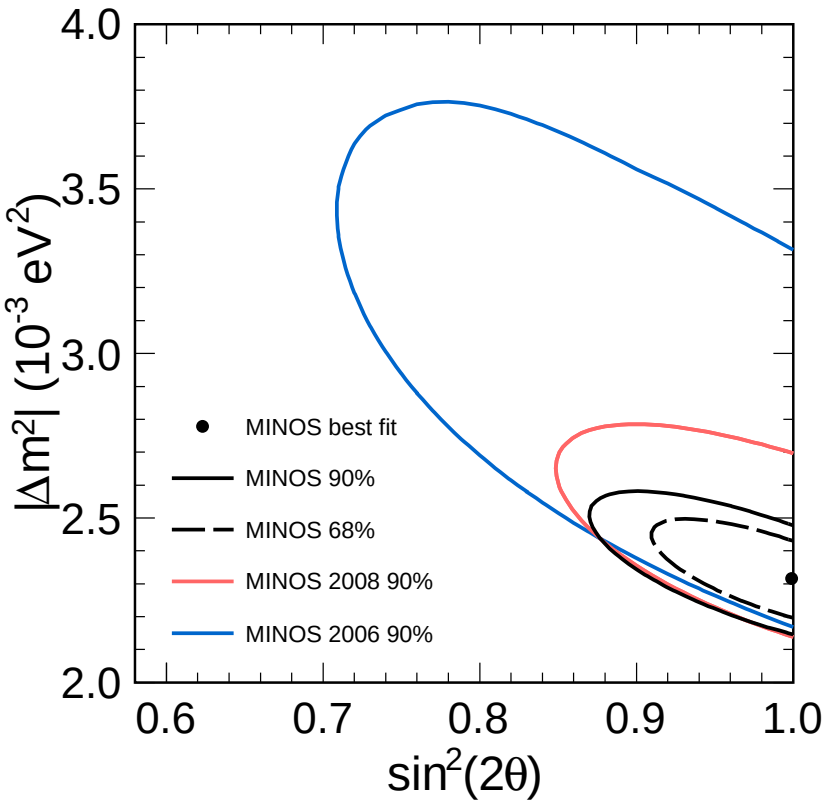

Figure 74: Comparison of MINOS fiducial+raf contours with previous results. Conference style plot with colour.

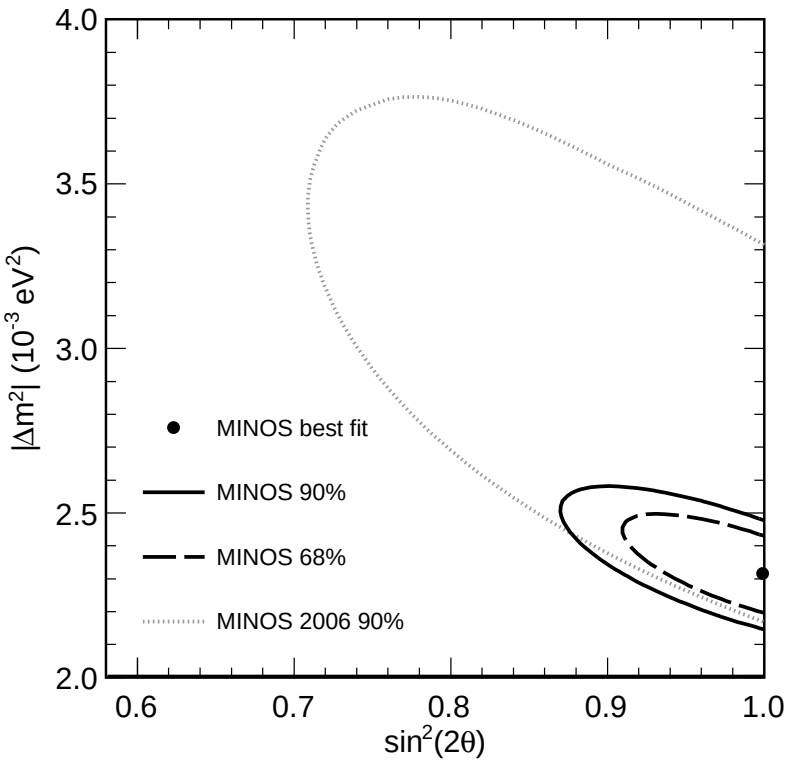

Figure 75: Comparison of MINOS fiducial+raf contours with previous results, not including the 2008 result.

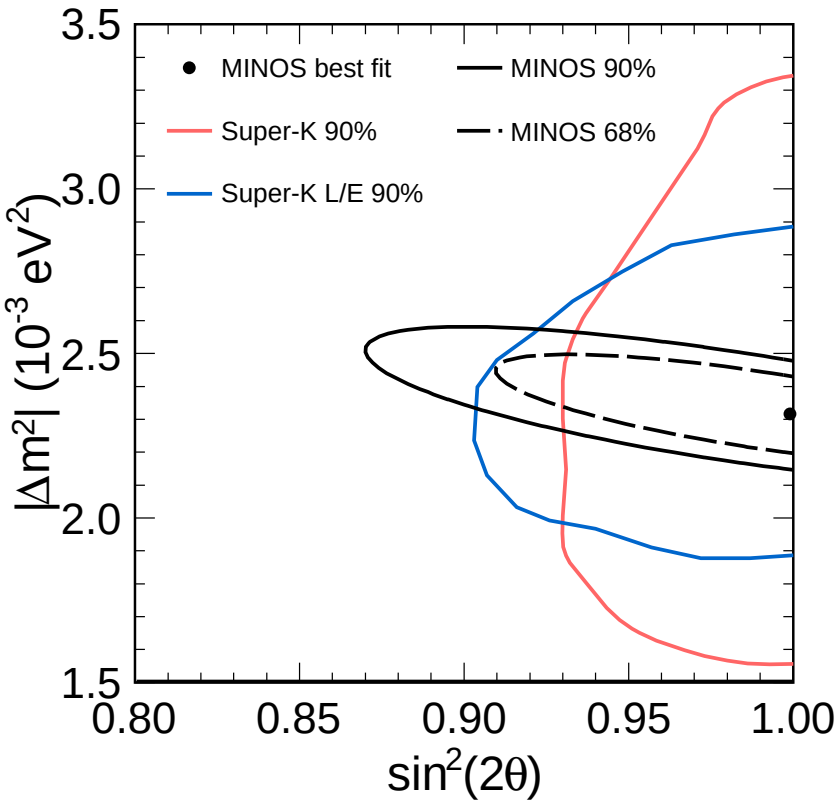

Figure 76: Comparison of MINOS fiducial+raf contours with previous MINOS and Super-K results, not including 2008 result. Conference style plot with colour.

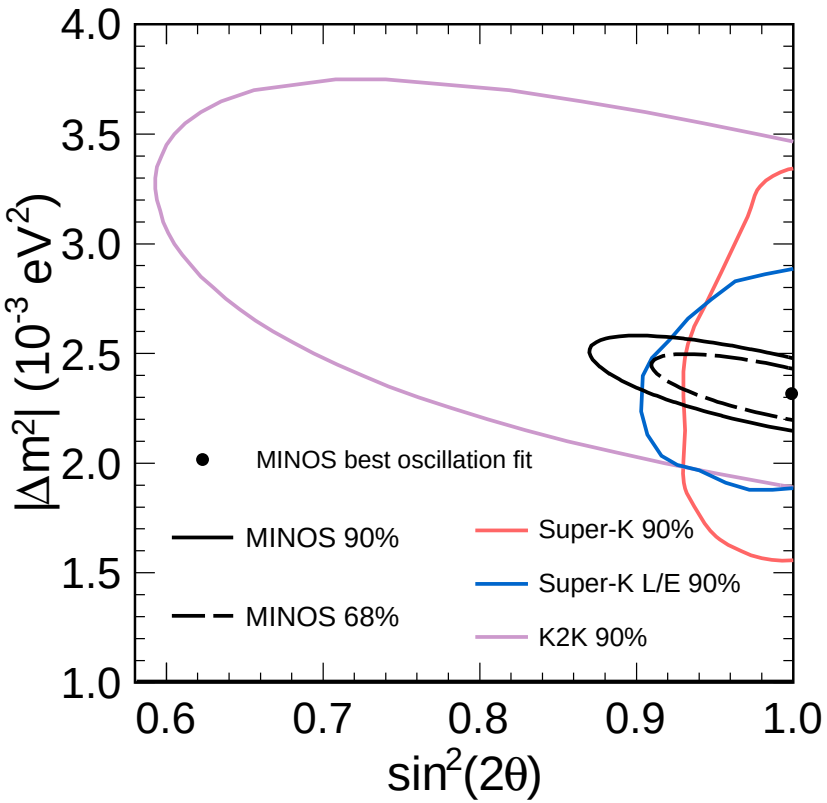

Figure 77: Comparison of MINOS fiducial+raf contours with previous MINOS, Super-K and K2K results, not including the 2008 result. Conference style plot with colour.

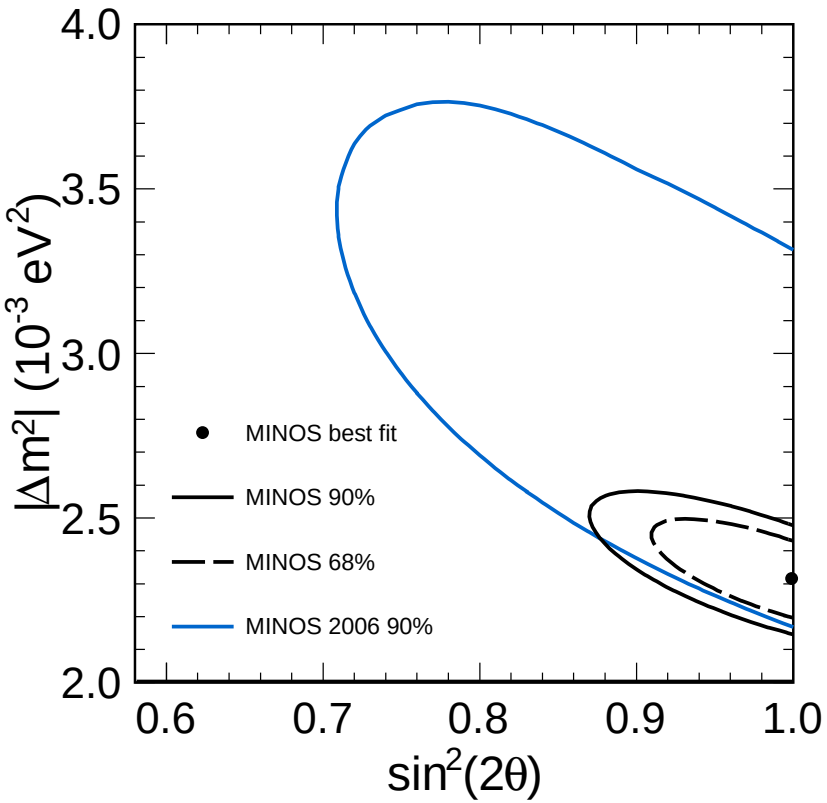

Figure 78: Comparison of MINOS fiducial+raf contours with previous results, not including the 2008 result. Conference style plot with colour.

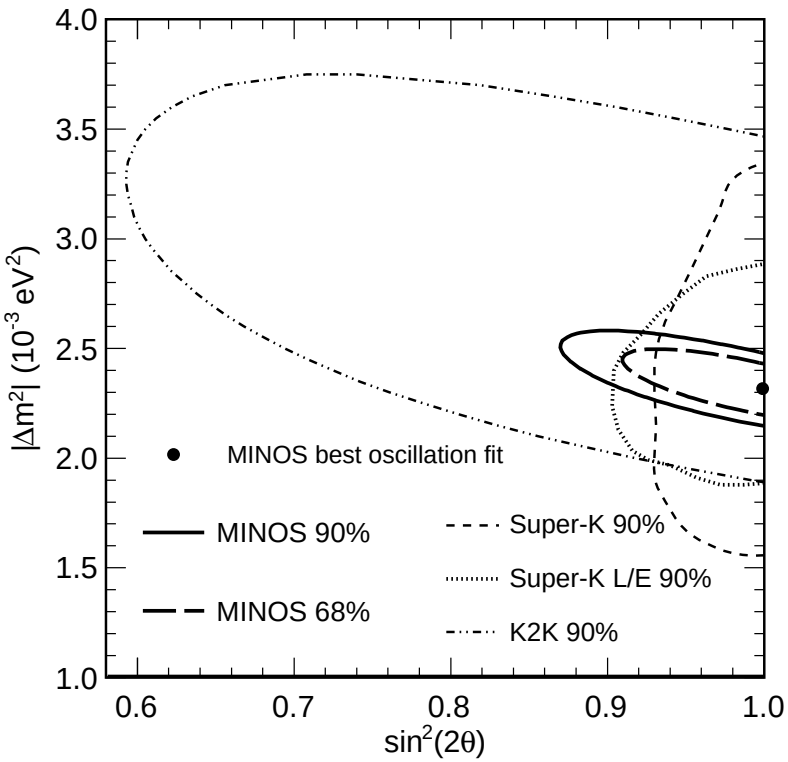

Figure 79: Comparison of MINOS fiducial+raf contours with previous MINOS, Super-K and K2K results; not including 2008 result.

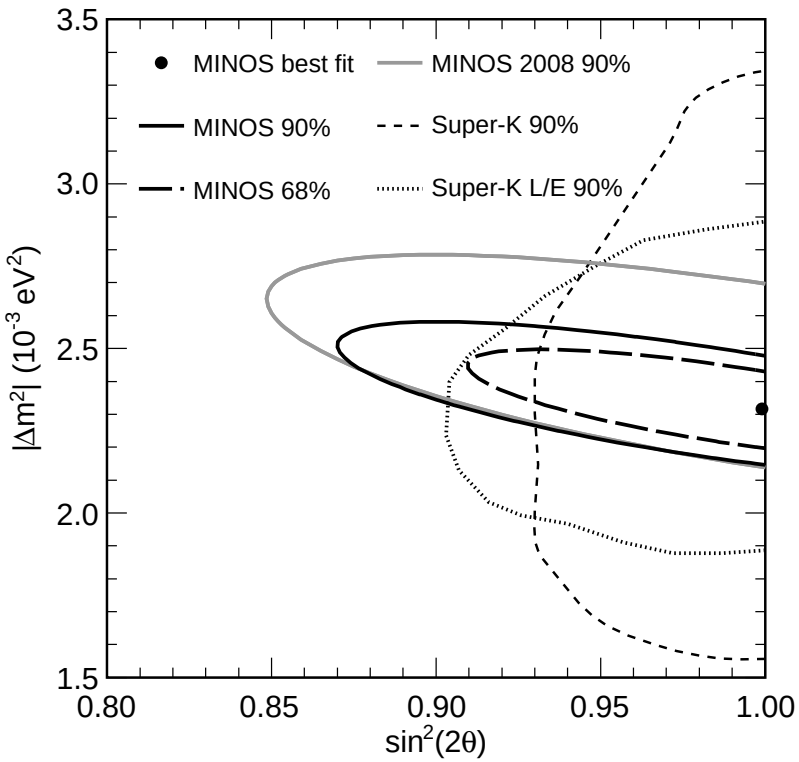

Figure 80: Comparison of MINOS fiducial+raf contours with previous MINOS and Super-K results.

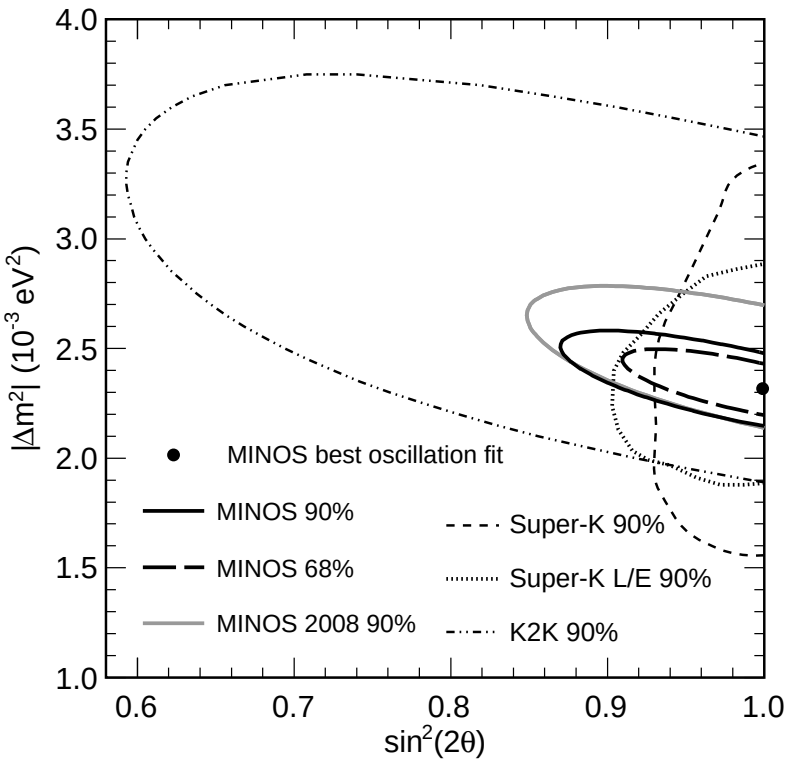

Figure 81: Comparison of MINOS fiducial+raf contours with previous MINOS, Super-K and K2K results.

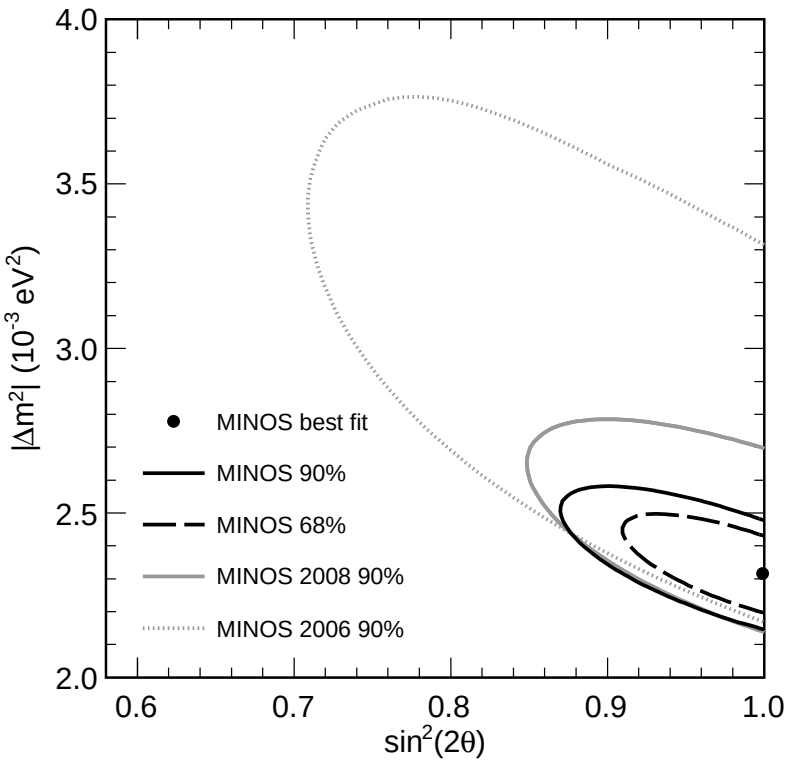

Figure 82: Comparison of MINOS fiducial+raf contours with previous results.

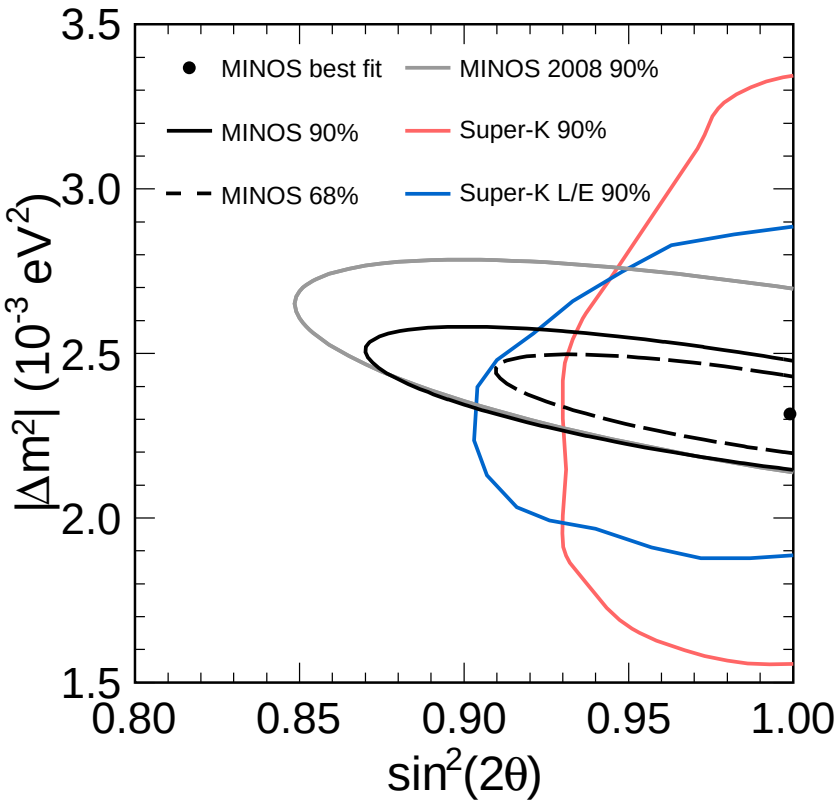

Figure 83: Comparison of MINOS fiducial+raf contours with previous MINOS and Super-K results. Conference style plot with colour.

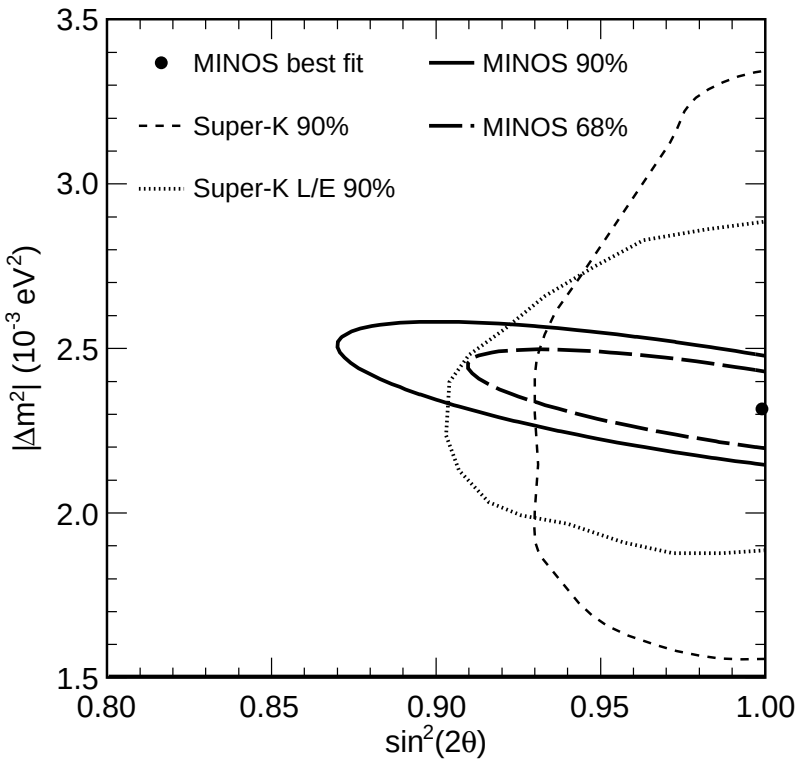

Figure 84: Comparison of MINOS fiducial+raf contours with previous MINOS and Super-K results, not including 2008 result.

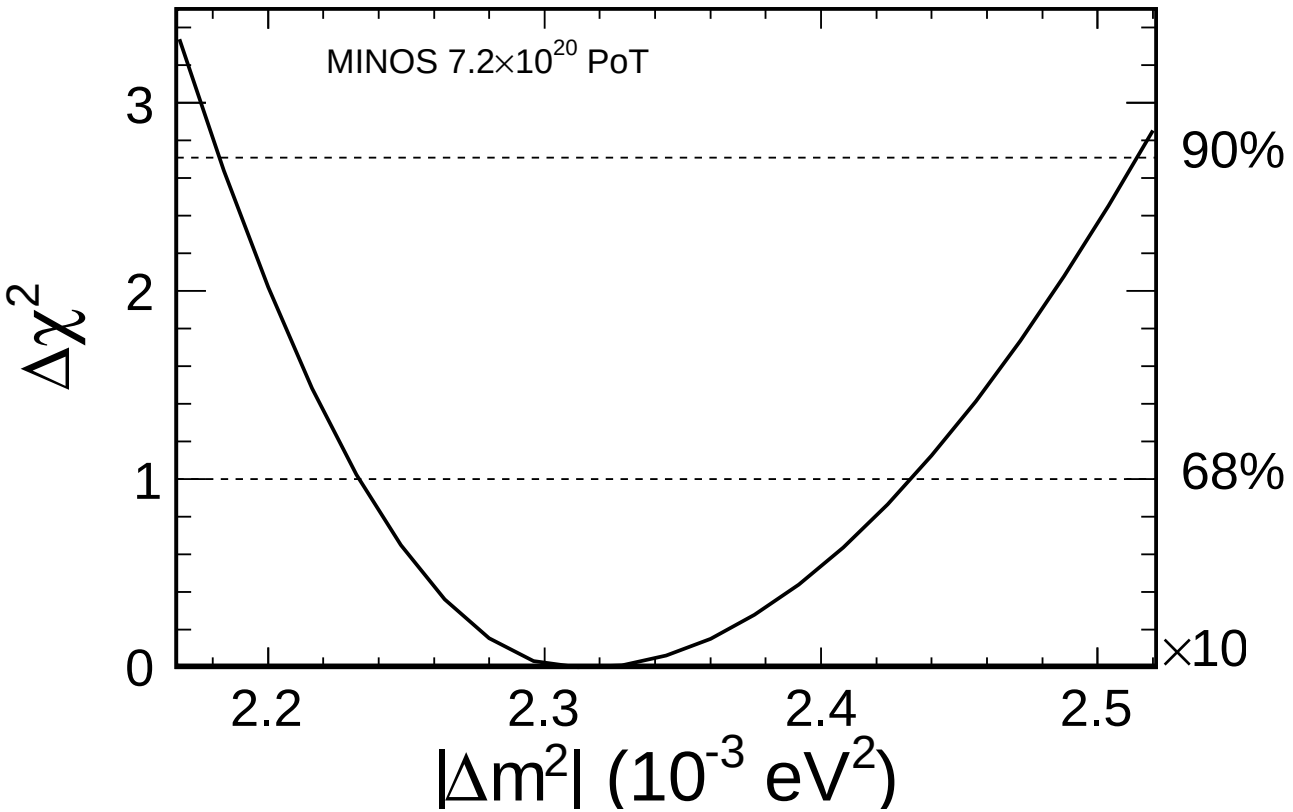

Figure 85: Marginalization of the fiducial+raf log-likelihood surface onto the Δm^2 (left) and $\sin^2 2\theta$ (right) axes.

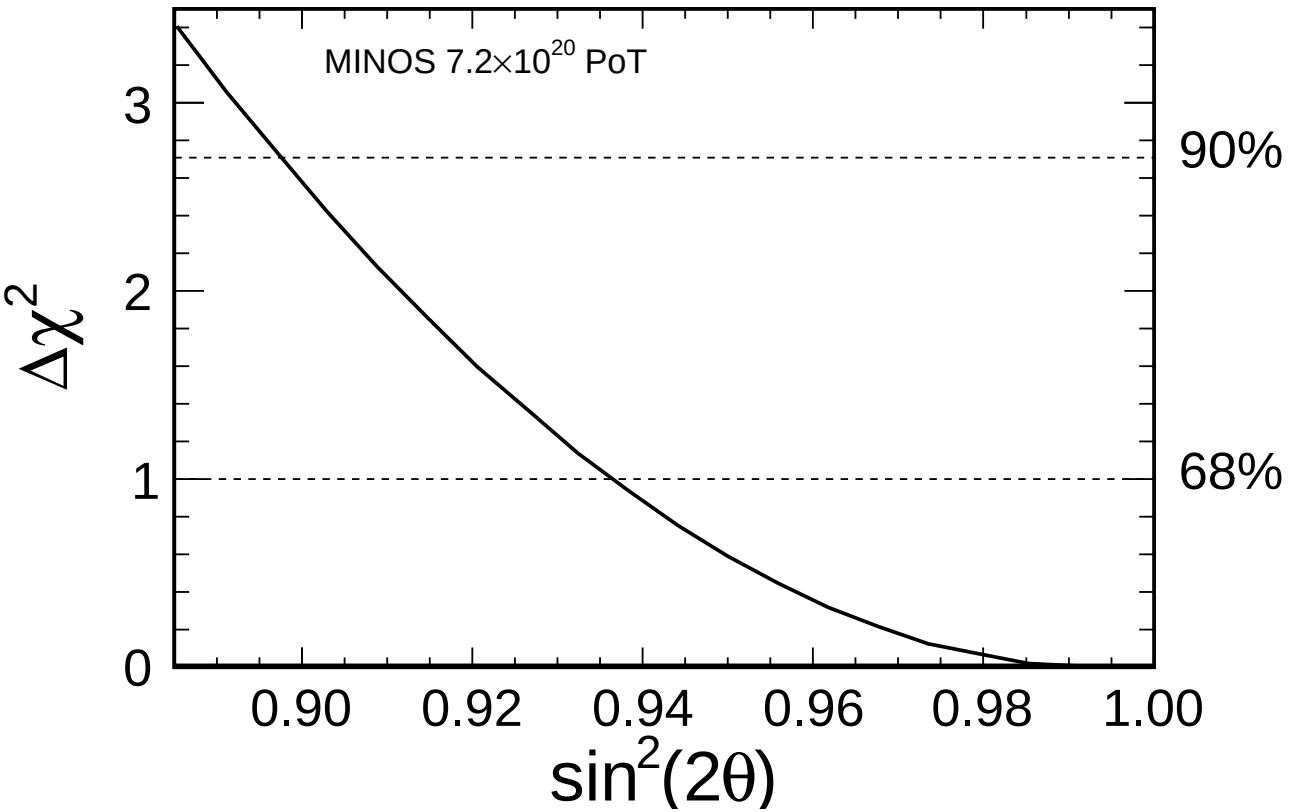

Figure 86: Marginalization of the fiducial+raf log-likelihood surface onto the Δm^2 (left) and $\sin^2 2\theta$ (right) axes.

Partially Reconstructed Event (RAF) plots

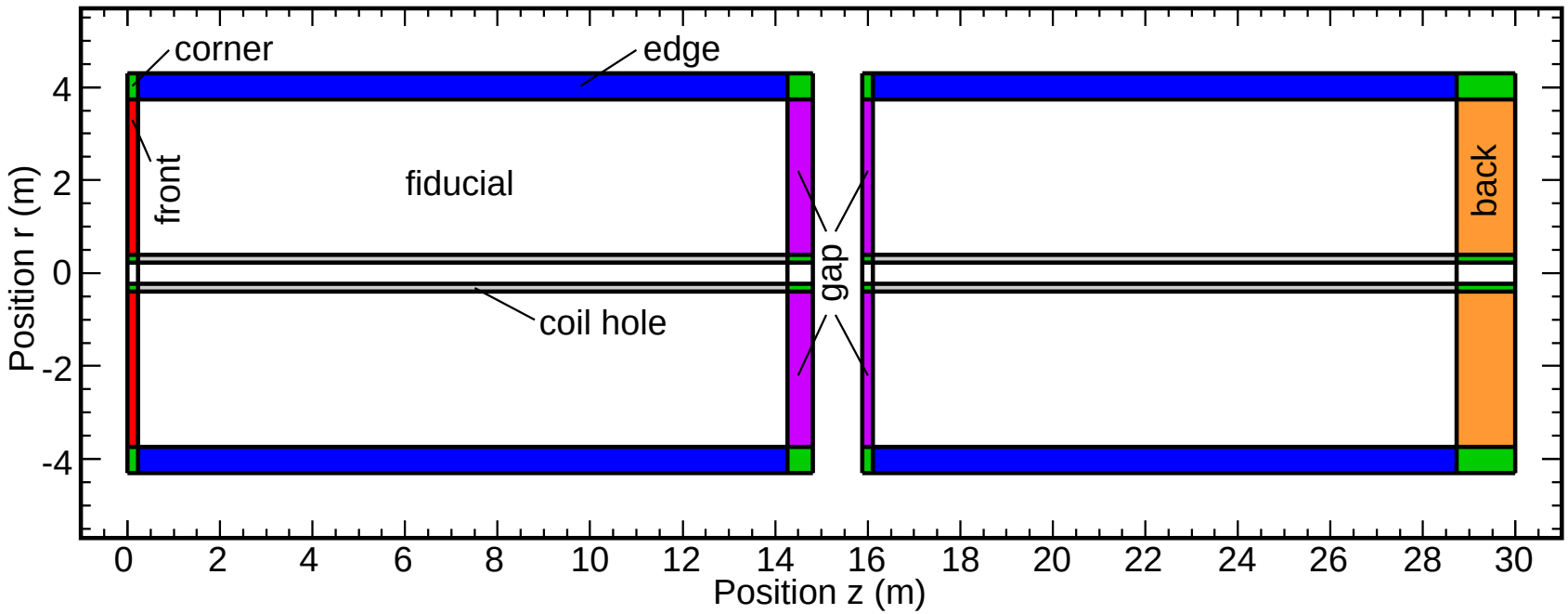

Figure 87: Diagram of antifiducial regions. These are colored to correspond with a simple narration of regions, not the fit histograms. So the edge is only one color, all corners are lumped together and the coil hole is included.

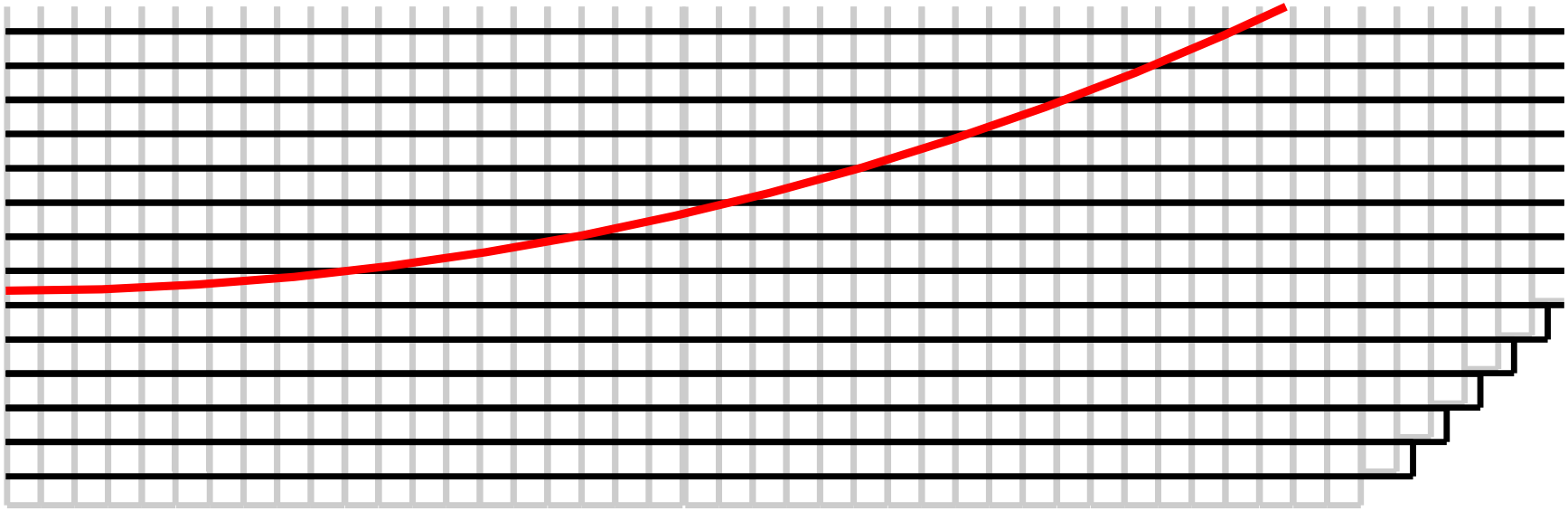

Figure 88: Strip detail on a diagonal edge. This is the Monte Carlo geometry which includes strip-by-strip transverse alignment data, but has ideal strip lengths and ideal strip longitudial alignment. Black is one view and grey is the other. It's not important which is U and which is V. The fiducial cut is shown in red.

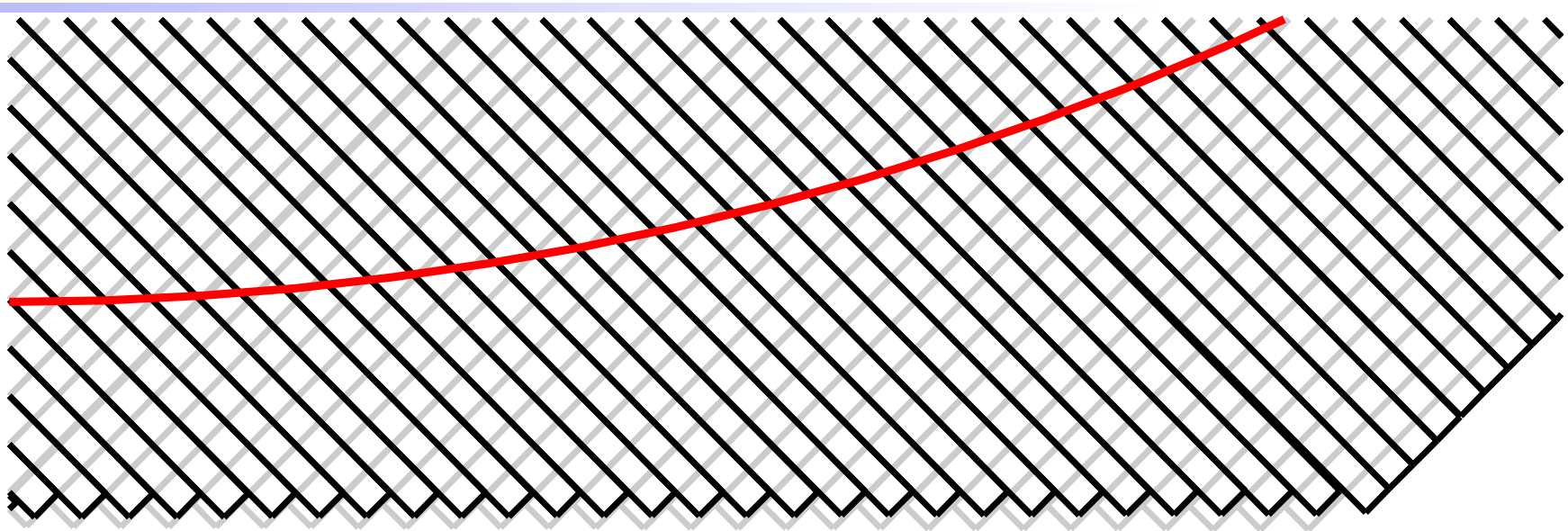

Figure 89: Strip detail on the bottom edge. This is the Monte Carlo geometry which includes strip-by-strip transverse alignment data, but has ideal strip lengths and ideal strip longitudial alignment. Black is one view and grey is the other. It's not important which is U and which is V. The fiducial cut is shown in red.

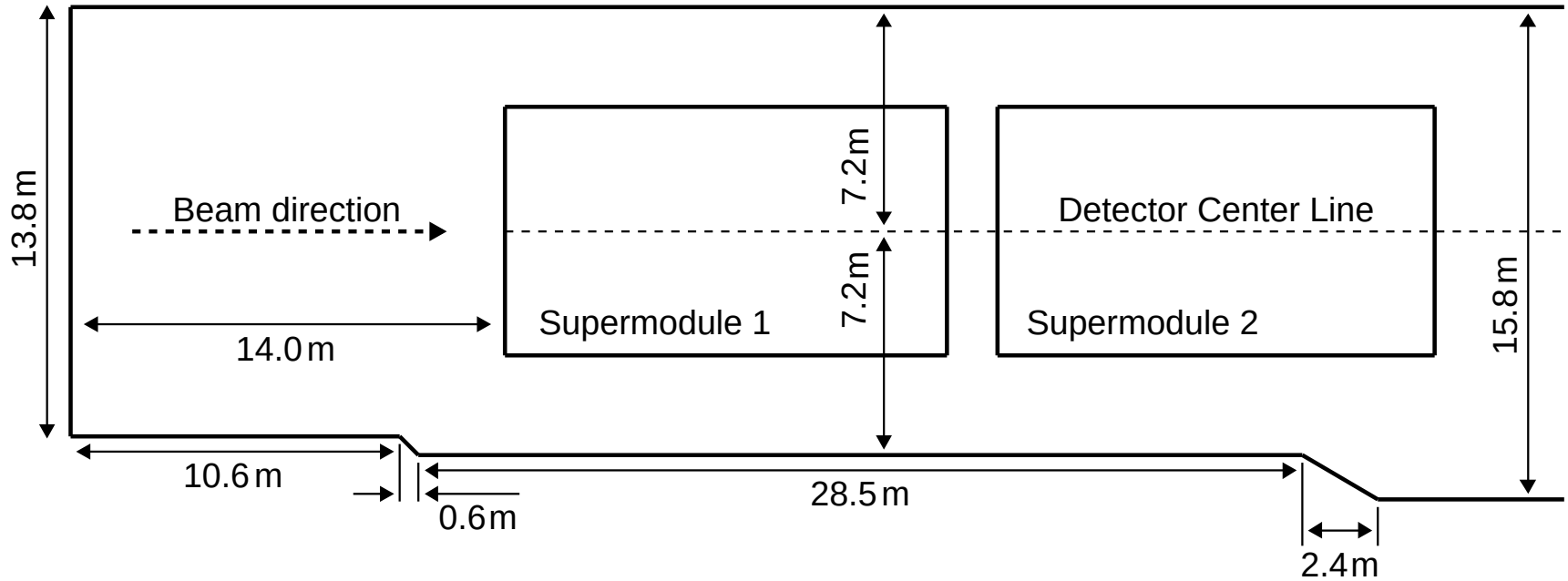

Figure 90: Plan view of the far detector hall with an emphasis on features important for the partially reconstructed event analysis.

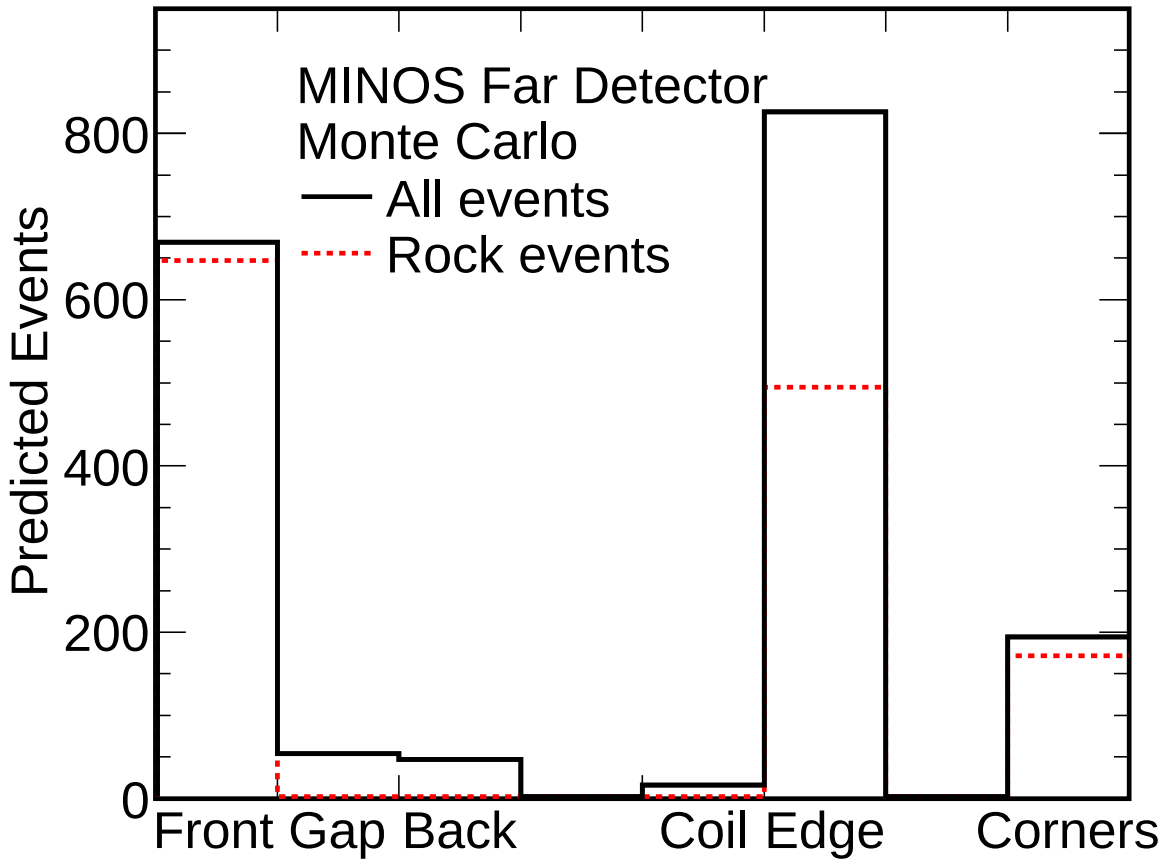

Figure 91: Frequency of partially reconstructed events by detector region. This is not the categorization used in the fit, but rather a simple categorization to go with the diagram of detector regions. It includes coil events to show how many events are lost from not using the coil, and puts all edge events together to show the fraction of true rock, for instance.

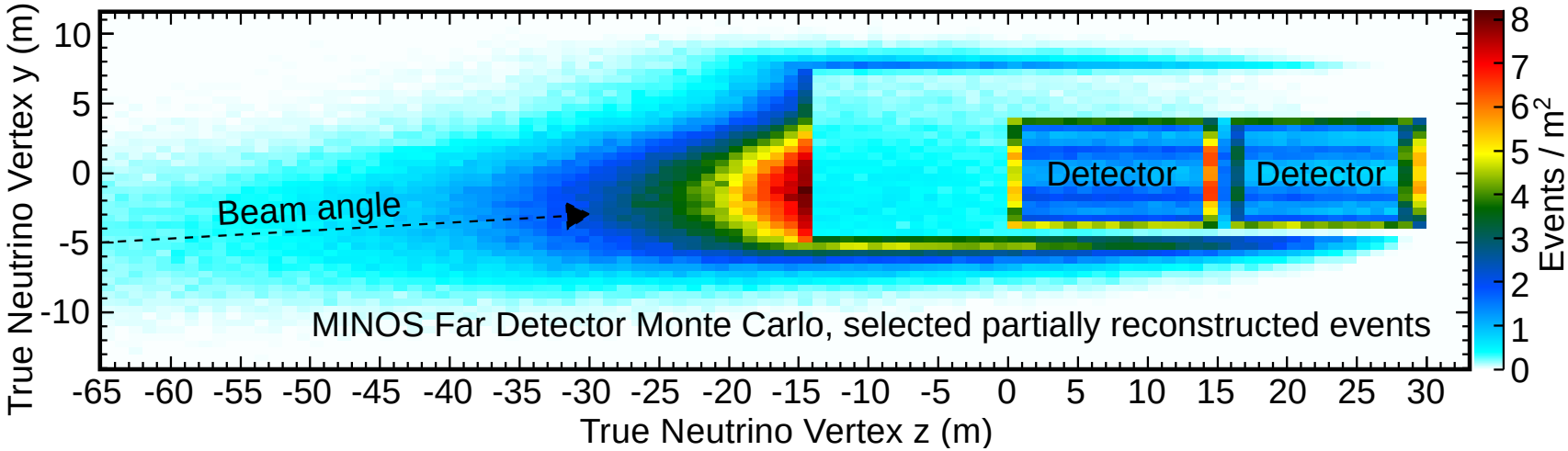

Figure 92: 2D projection of the distribution of true neutrino vertices of selected partially reconstructed events. The high energy tail extends to ~ -150 m, but this is hard to show without unacceptably shrinking the rest of the plot. Note that this is not a cross section, so the number of events between the south wall of the cavern and the detector is non-zero due to events in the east and west walls. Similarly, there are events all around the outside of the detector.

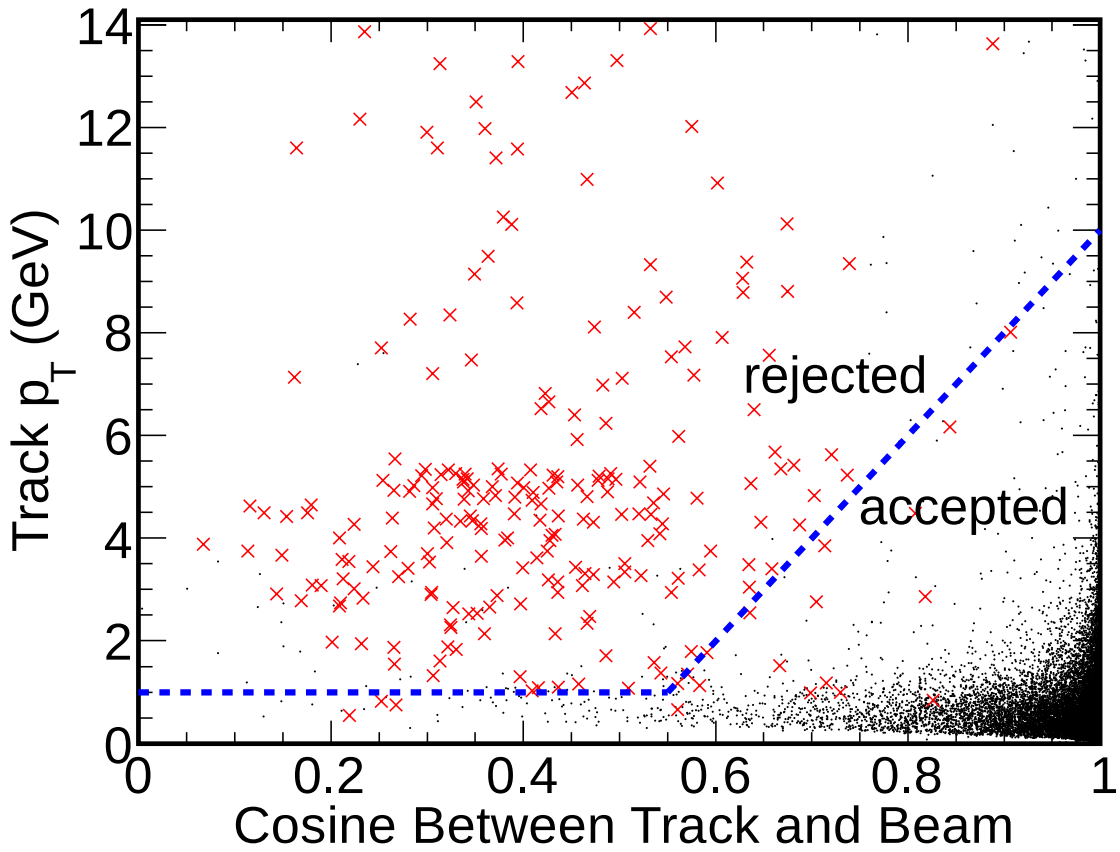

Figure 93: Two of the three spatial cosmic rejection cuts. Events above and to the left of the blue dashed line are rejected. Red crosses are cosmic data; black dots are LE spill Monte Carlo. Each is shown at an exposure of 10 times Runs I–III.

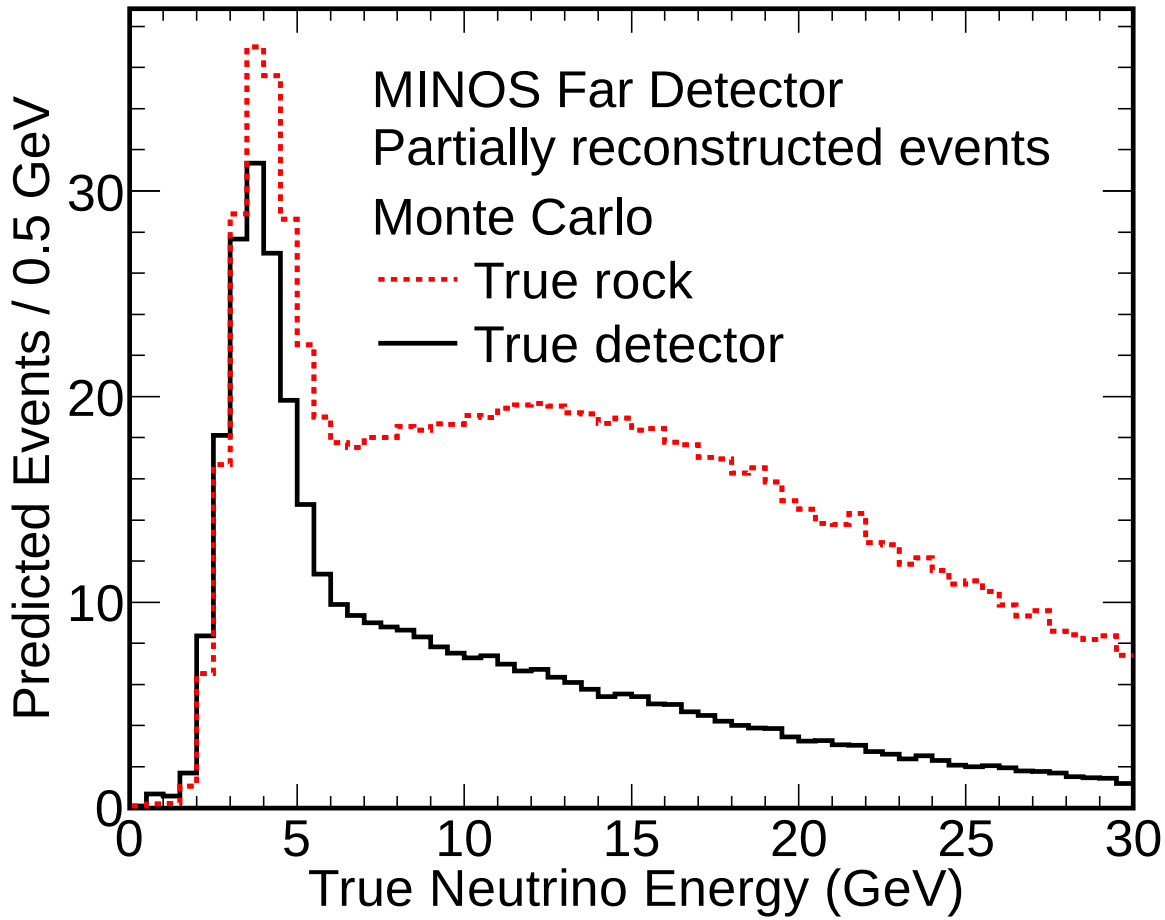

Figure 94: True neutrino spectrum (low energy beam) for selected partially reconstructed events events, separated into true rock events and true detector events.

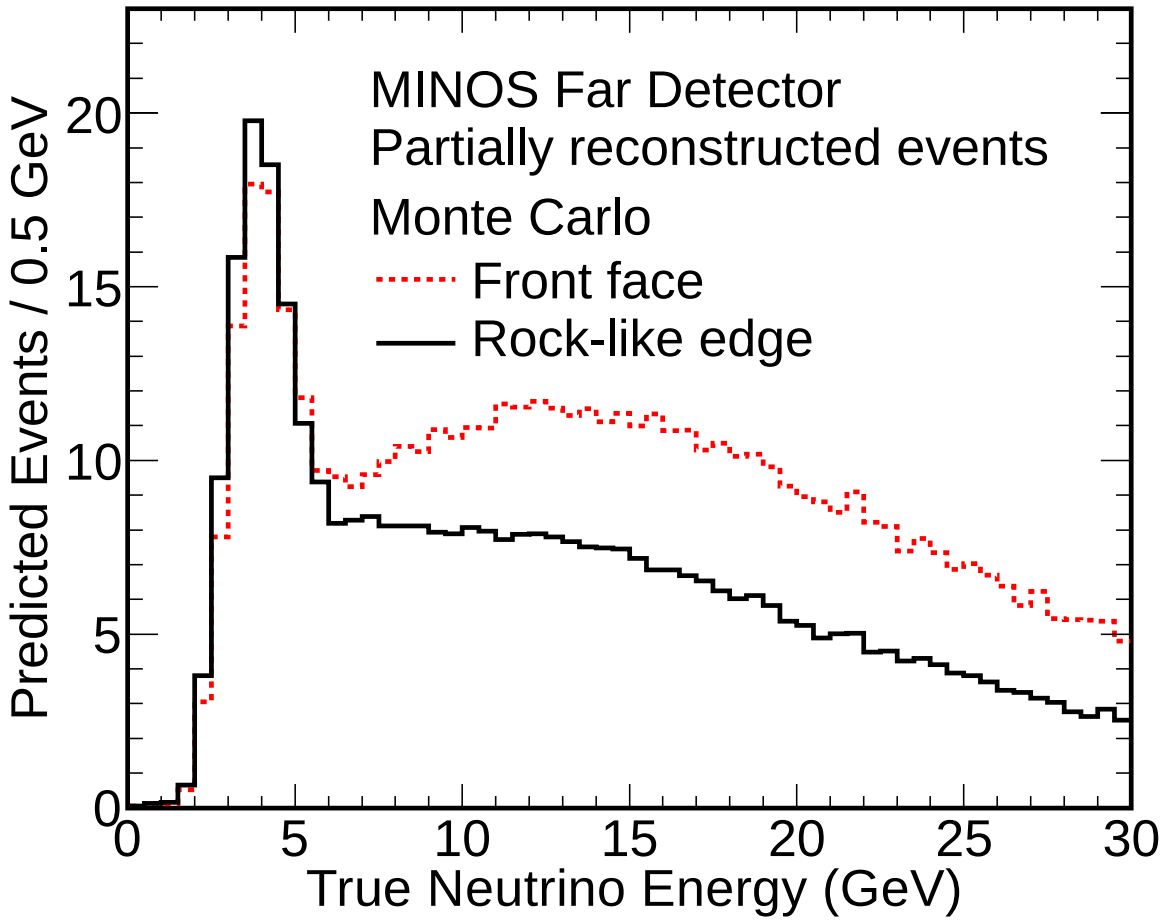

Figure 95: Comparison of true neutrino energy (low energy beam) for selected rock-like events on the front face and the edge. The front face events tend to be higher energy since it is easy for them to reach this face from deep in the upstream rock.

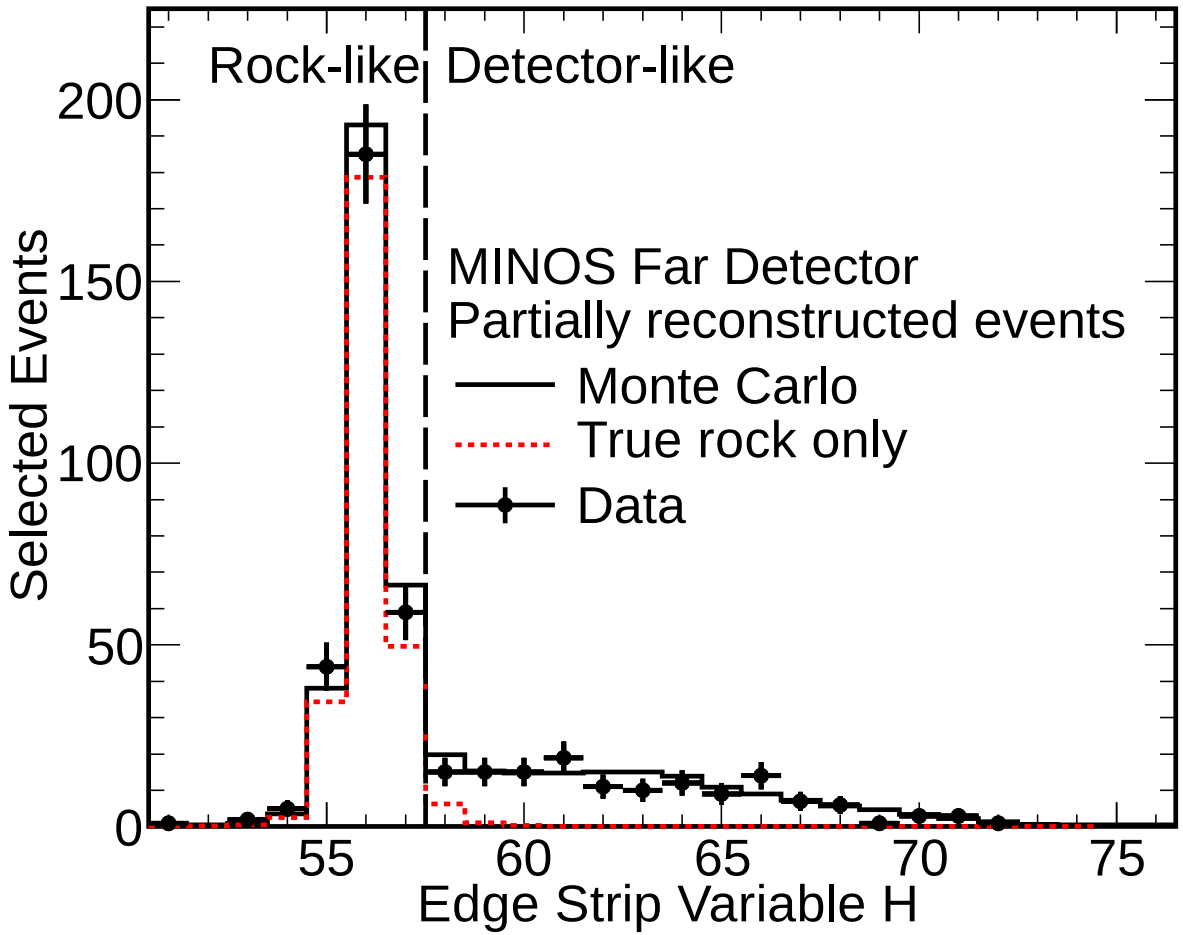

Figure 96: Rock/detector separation on the horizontal and vertical edges. Events are selected as rock-like if H, the discrimination parameter, is 57 or less and detector-like otherwise. H is defined by the sum or difference of strip numbers of the first track hits in the two views arranged so that moving when the intersection of the two strips moves inwards, the number increases and that the same number means the same distance from the edge for all four horizontal/vertical edges. The fall-off starting around $H = 65$ is due to the fiducial cut, which has a variable distance from the edge.

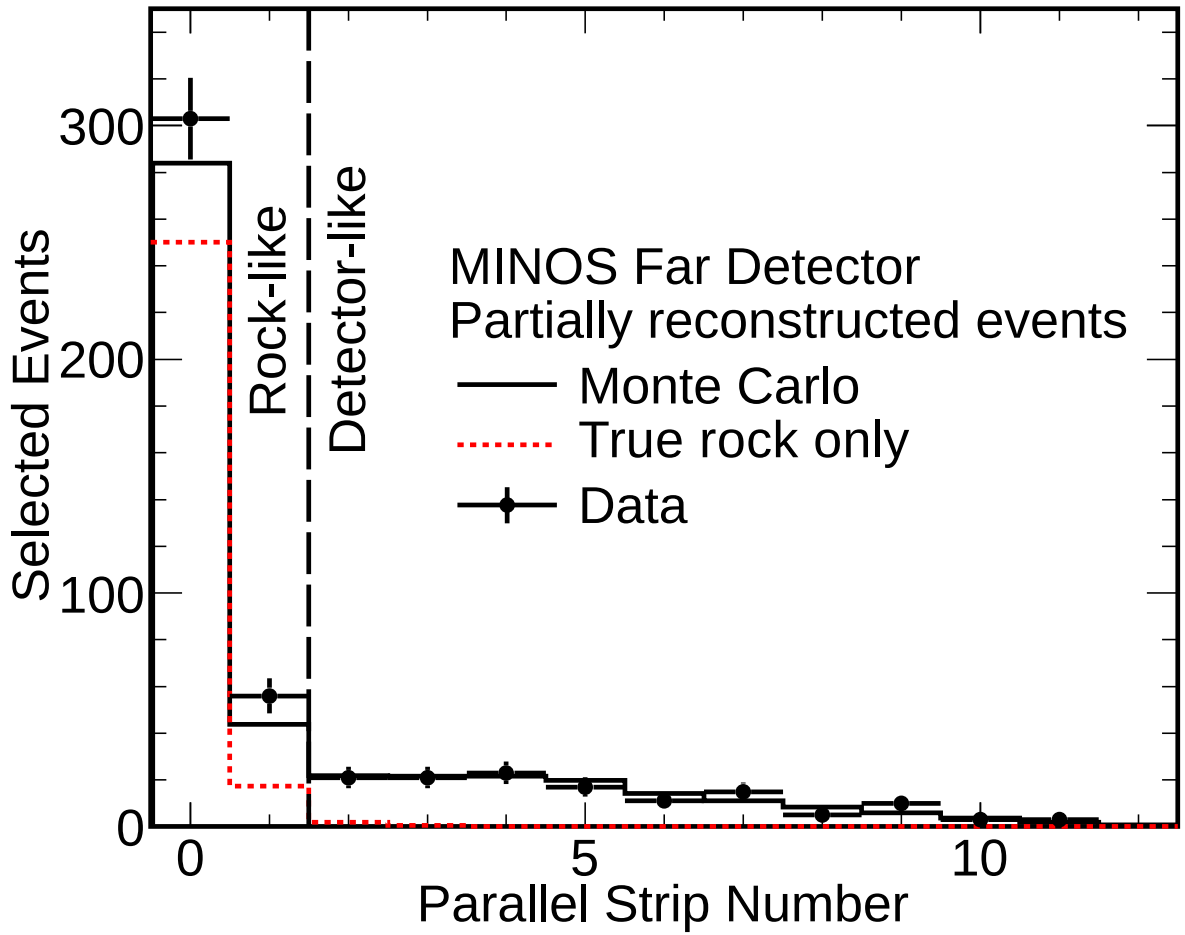

Figure 97: Rock/detector separation on the diagonal edges. The "parallel strip number" is the strip number of the first strip hit in the view having strips parallel to the edge. Here strips are always numbered from the edge starting with zero. Events with a parallel strip number of 0 or 1 are selected as rock-like, and the rest as detector-like. Note that events with a parallel strip number of 1 are more likely to be detector events, but better sensitivity is gotten by putting them in the rock-like category, since the large number of rock events does not then contaminate the higher-quality detector-like category. The fall-off starting around 5 is due to the fiducial cut, which has a variable distance from the edge.

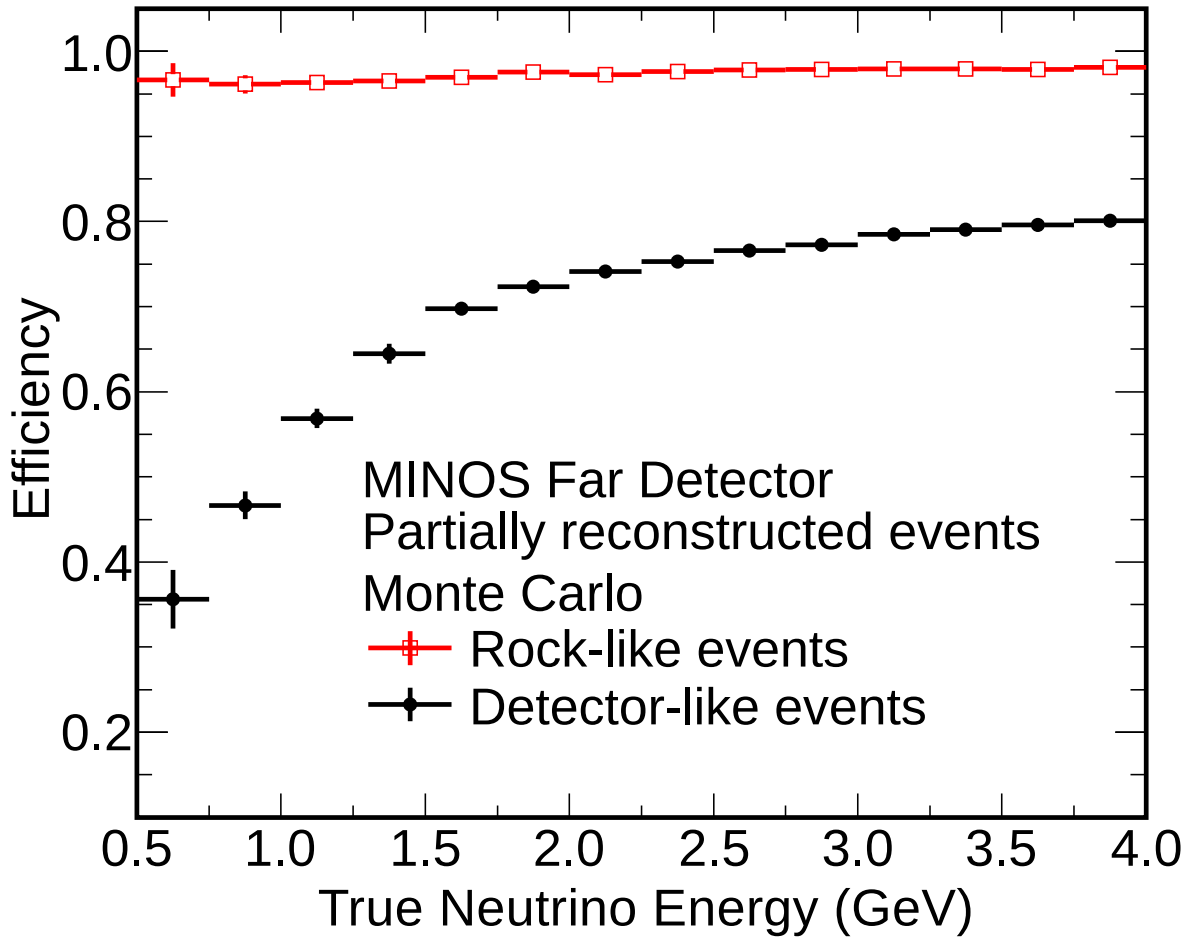

Figure 98: Efficiency at accepting true $\nu_\mu/\bar{\nu}_\mu$ charged current events as a function of true neutrino energy. In order to be in the denominator of the efficiency, an event must produce a reconstructed track. Rock events have very high efficiency over all energies because background events generally do not make it out of the rock and so the PID cuts are set very loosely.

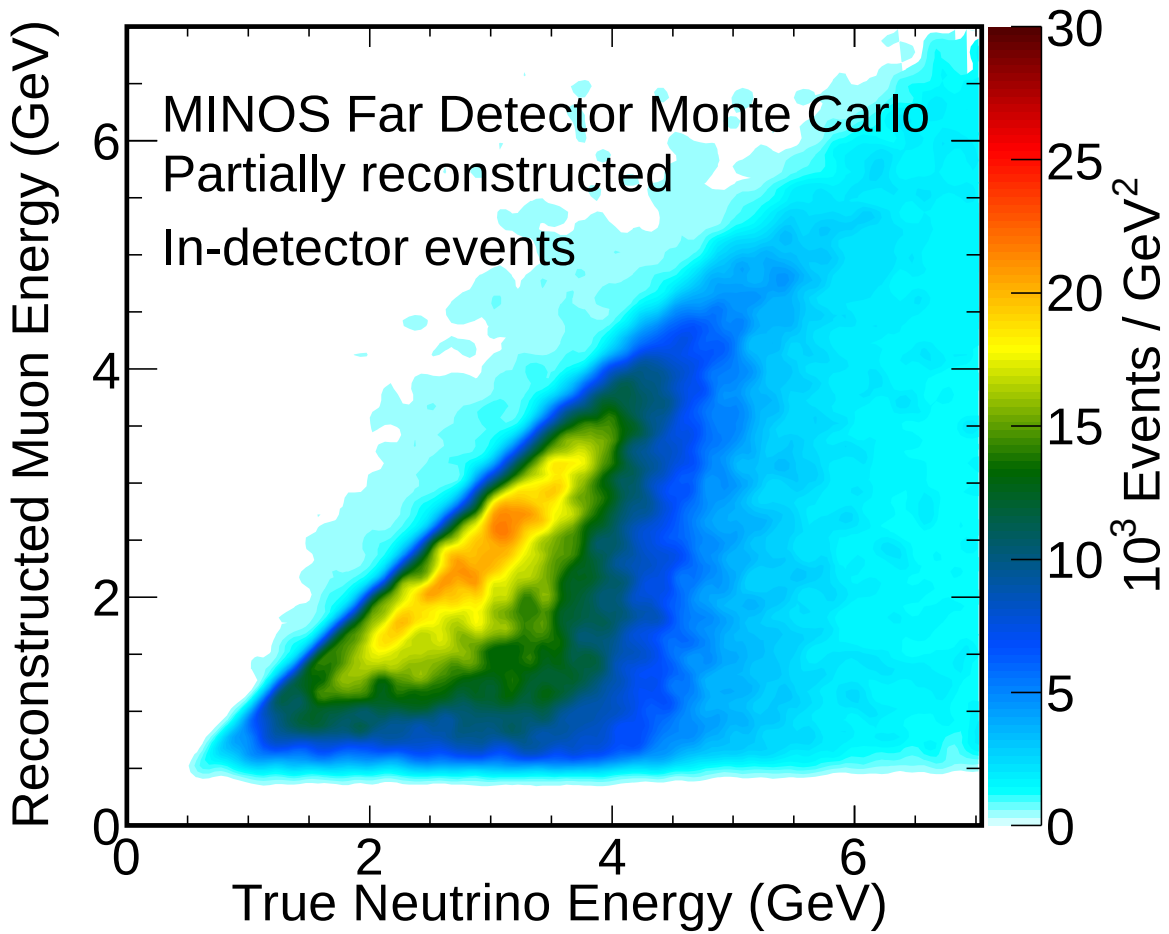

Figure 99: Relationship between neutrino energy and reconstructed muon energy for true detector partially reconstructed events.

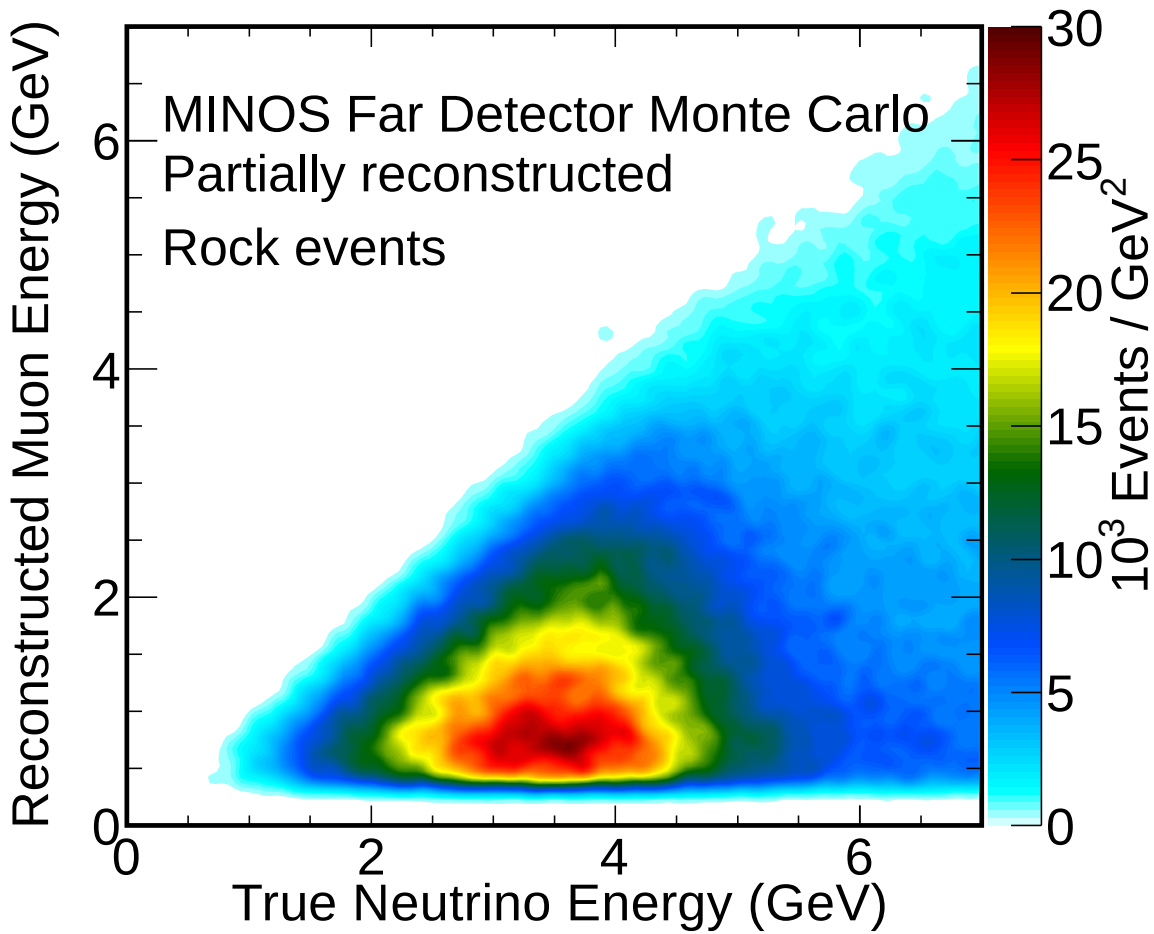

Figure 100: Relationship between neutrino energy and reconstructed muon energy for true rock partially reconstructed events.

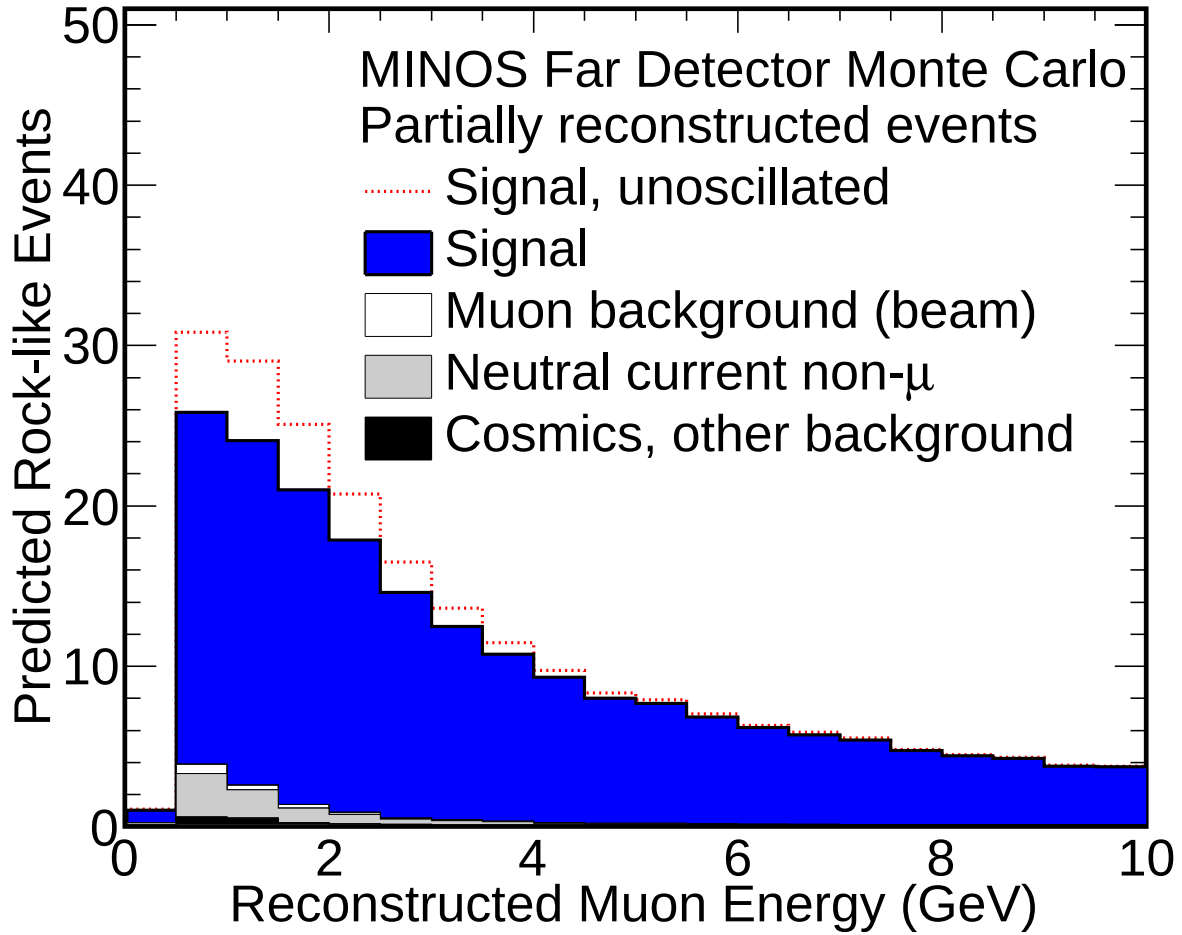

Figure 101: Stacked histogram of Monte Carlo selected rock-like events. Among other things, this highlights the irreducable background of true muons coming out of the rock due to beam events, but not $\nu_\mu/\bar{\nu}_\mu$ charged current events. The legend on this plot is meant to apply to this plot and also the detector-like version of the same thing.

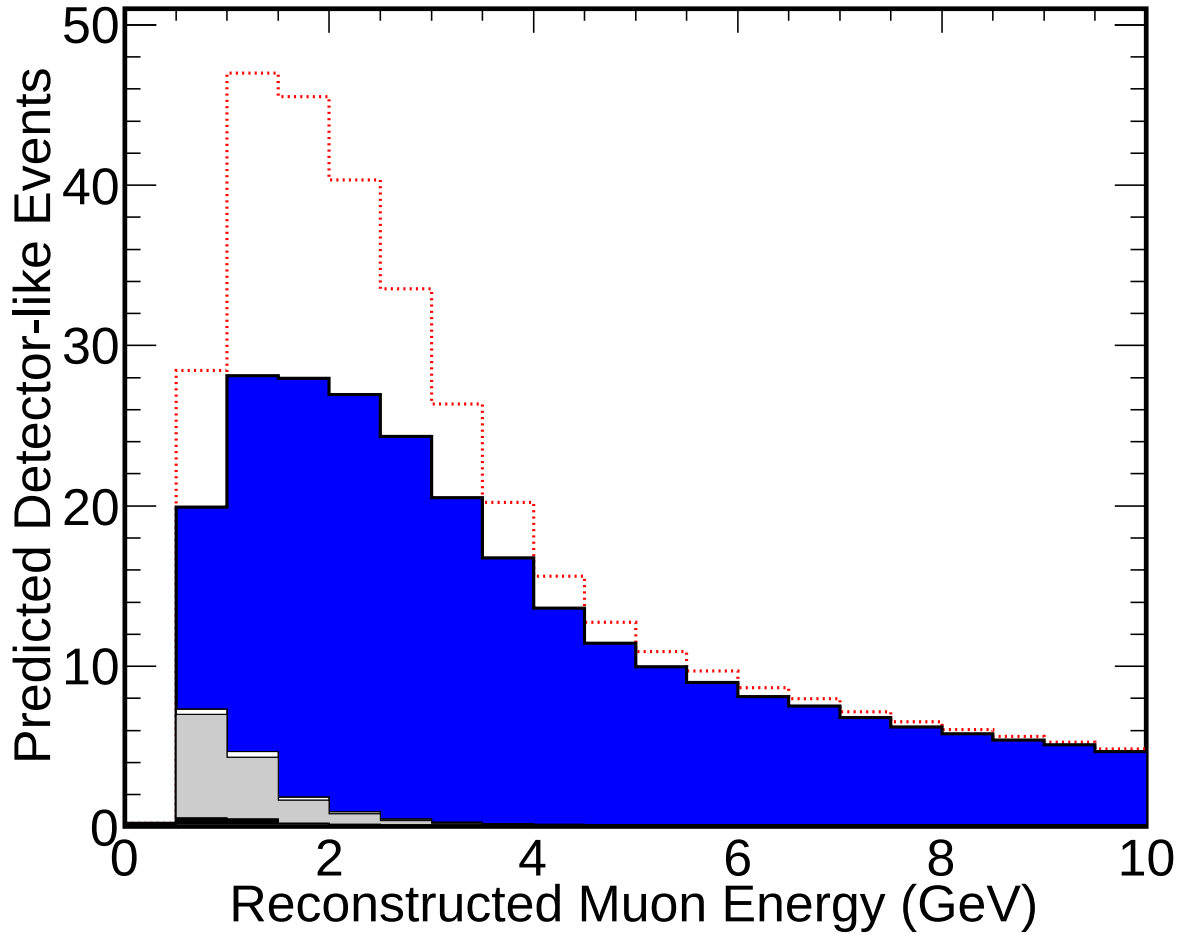

Figure 102: Stacked histogram of of Monte Carlo selected detector-like events. There is no legend since this is exepcted to appear with the rock-like version of the same thing.

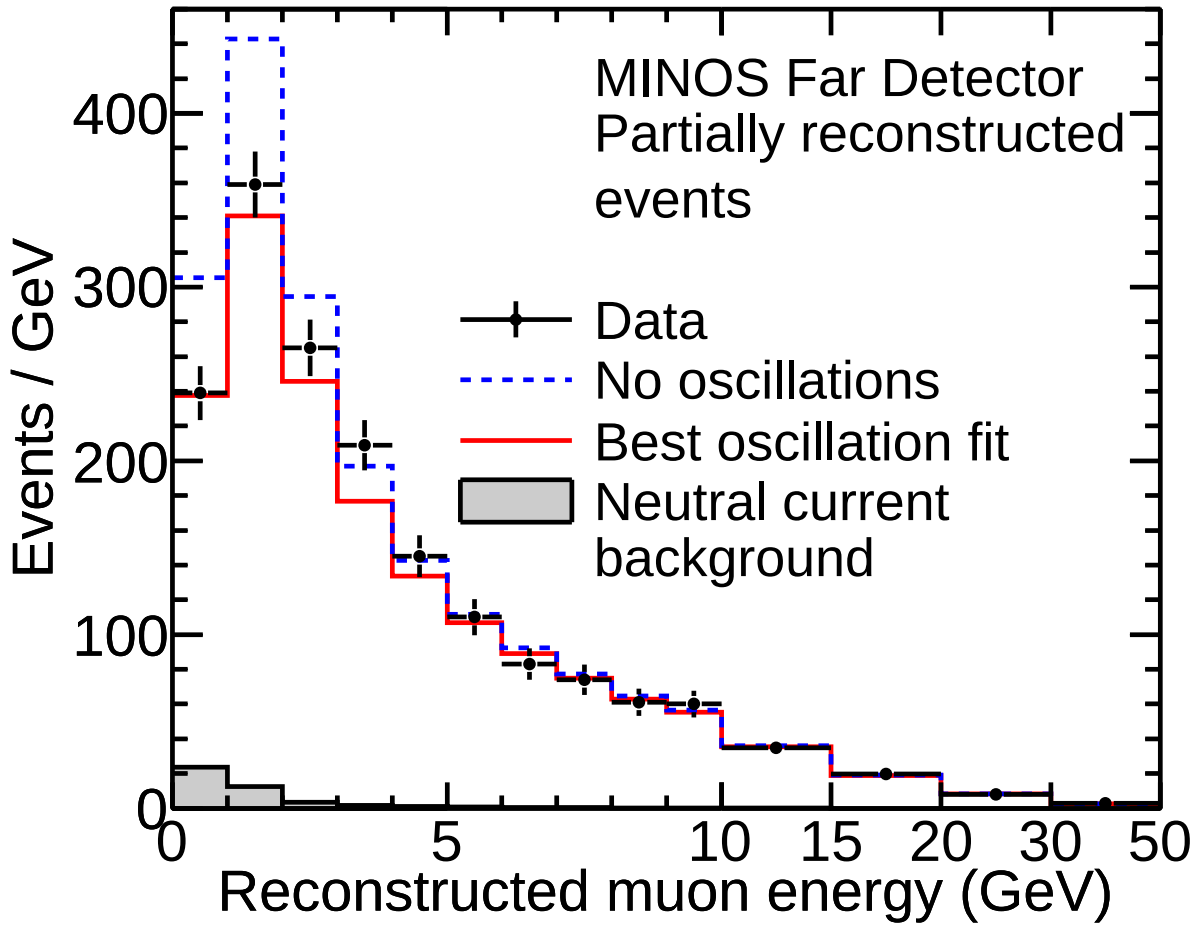

Figure 103: The energy spectra of partially reconstructed events originating in the surrounding rock or outer parts of the Far Detector.

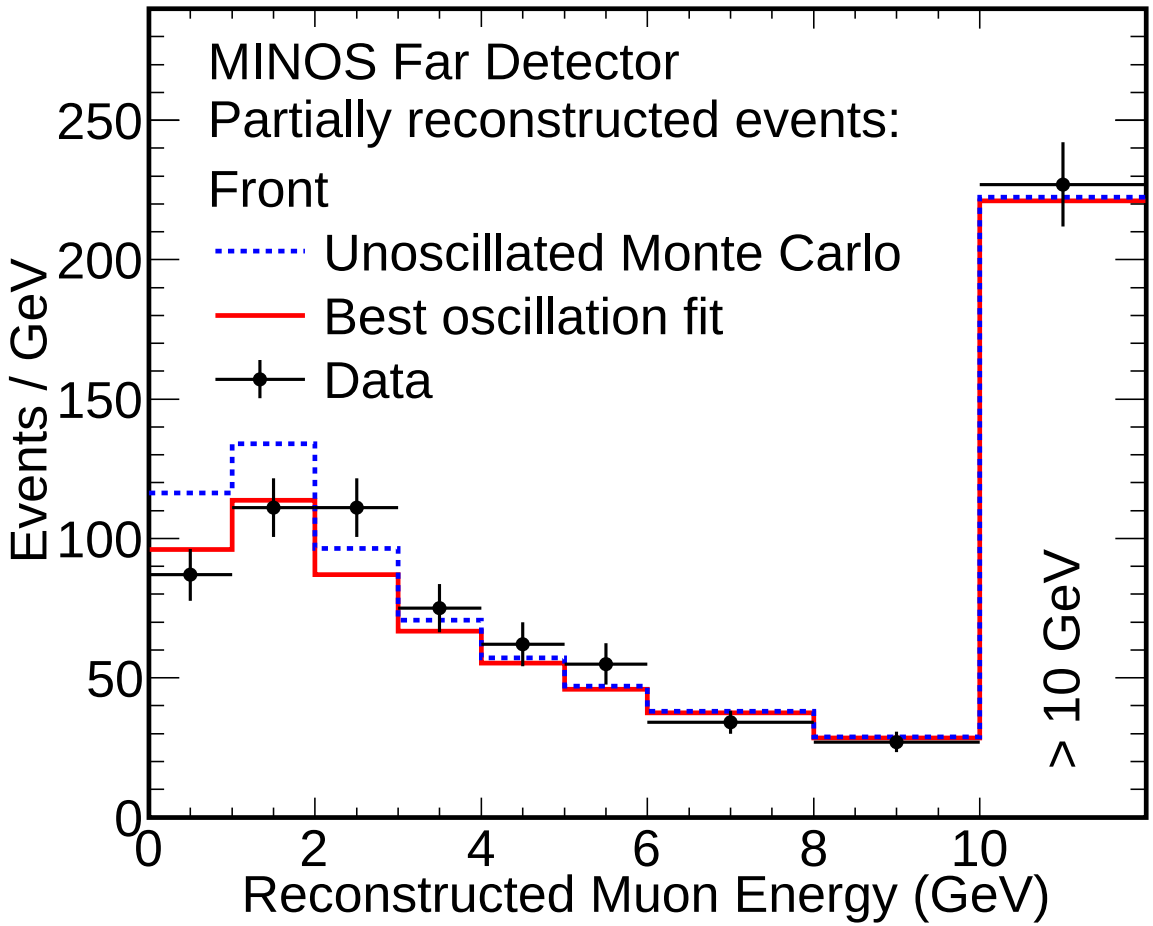

Figure 104: Histogram of front events. This is a display binning. Note excellent agreement in the high energy tail. This histogram has the legend which is meant to apply to it and the other three partially reconstructed event histograms.

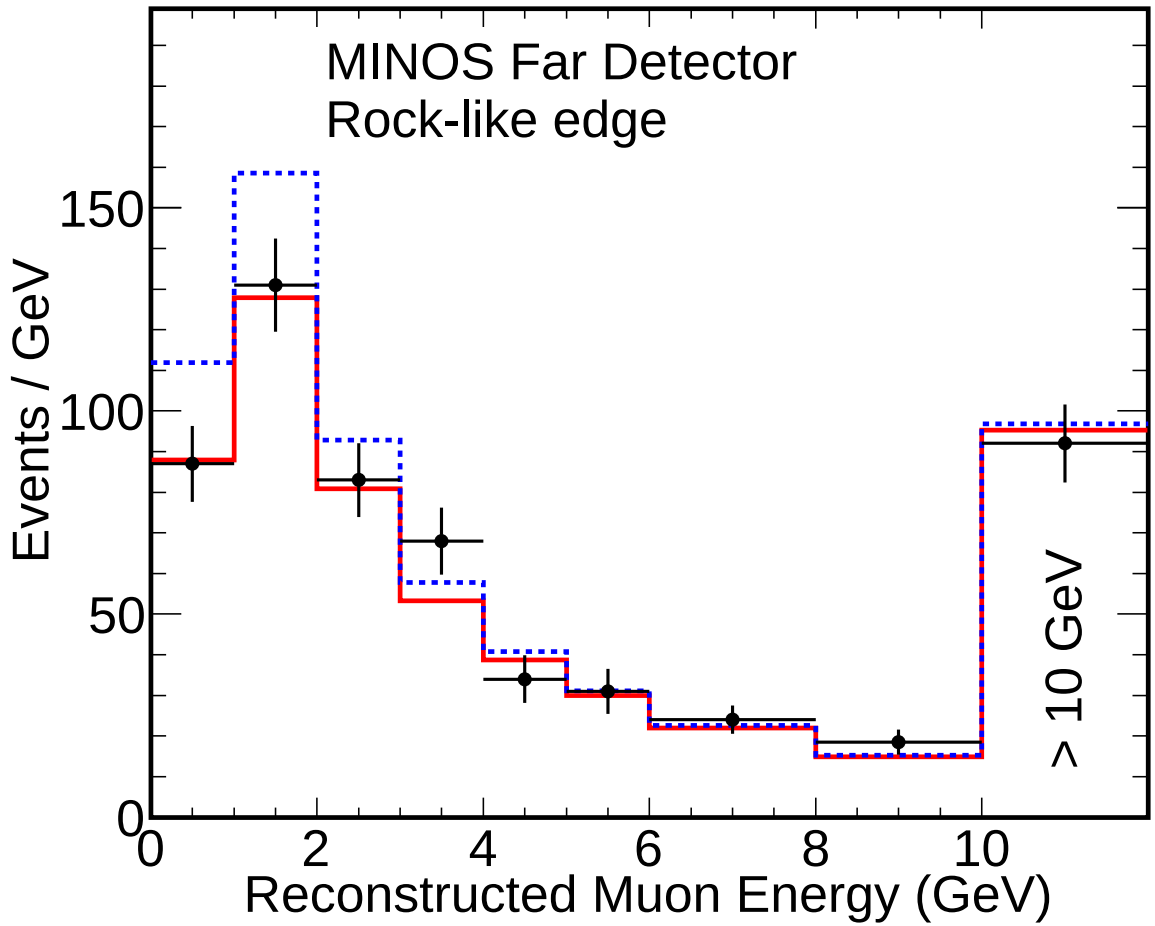

Figure 105: Histogram of events selected as rock-like edge. This is a display binning. Note excellent agreement in the high energy tail. There is no legend since I expect this will only be shown with the front event histogram which uses the same scheme.

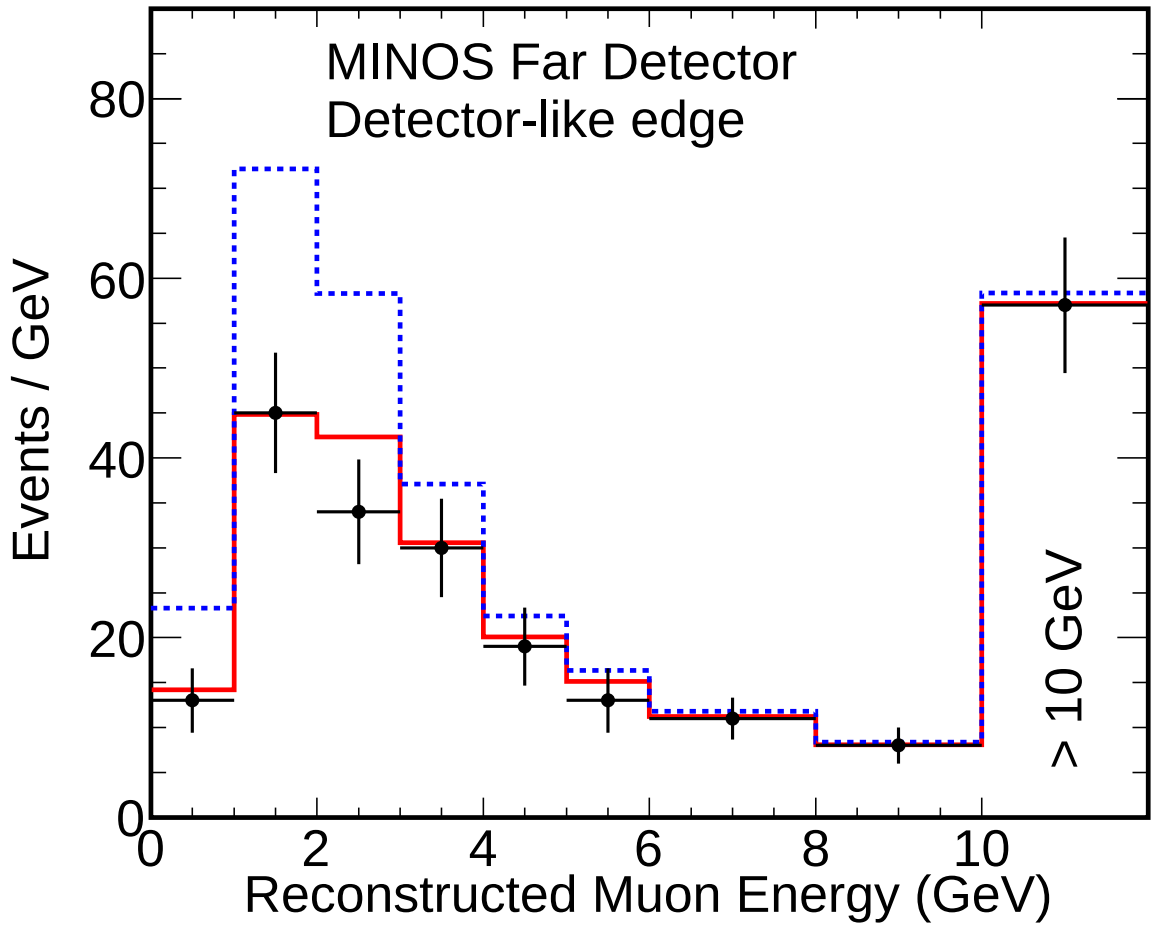

Figure 106: Histogram of events selected as detector-like edge. This is a display binning. Note excellent agreement in the high energy tail. There is no legend since I expect this will only be shown with the front event histogram which uses the same scheme.

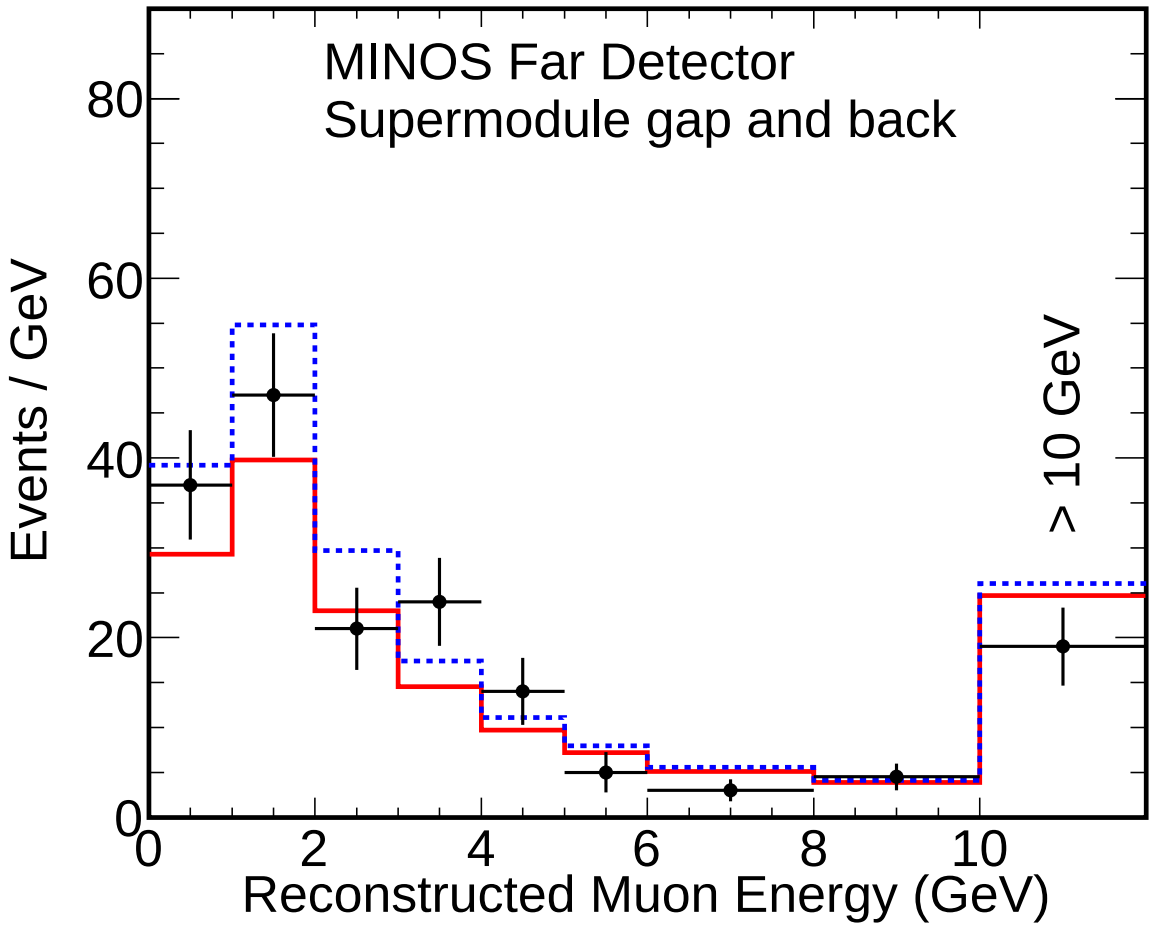

Figure 107: Histogram of back, supermodule gap and supermodule gap edge events. This is a display binning (the events are fit in a different binning and in three histograms). Note good agreement in the high energy tail. There is no legend since I expect this will only be shown with the front event histogram which uses the same scheme.

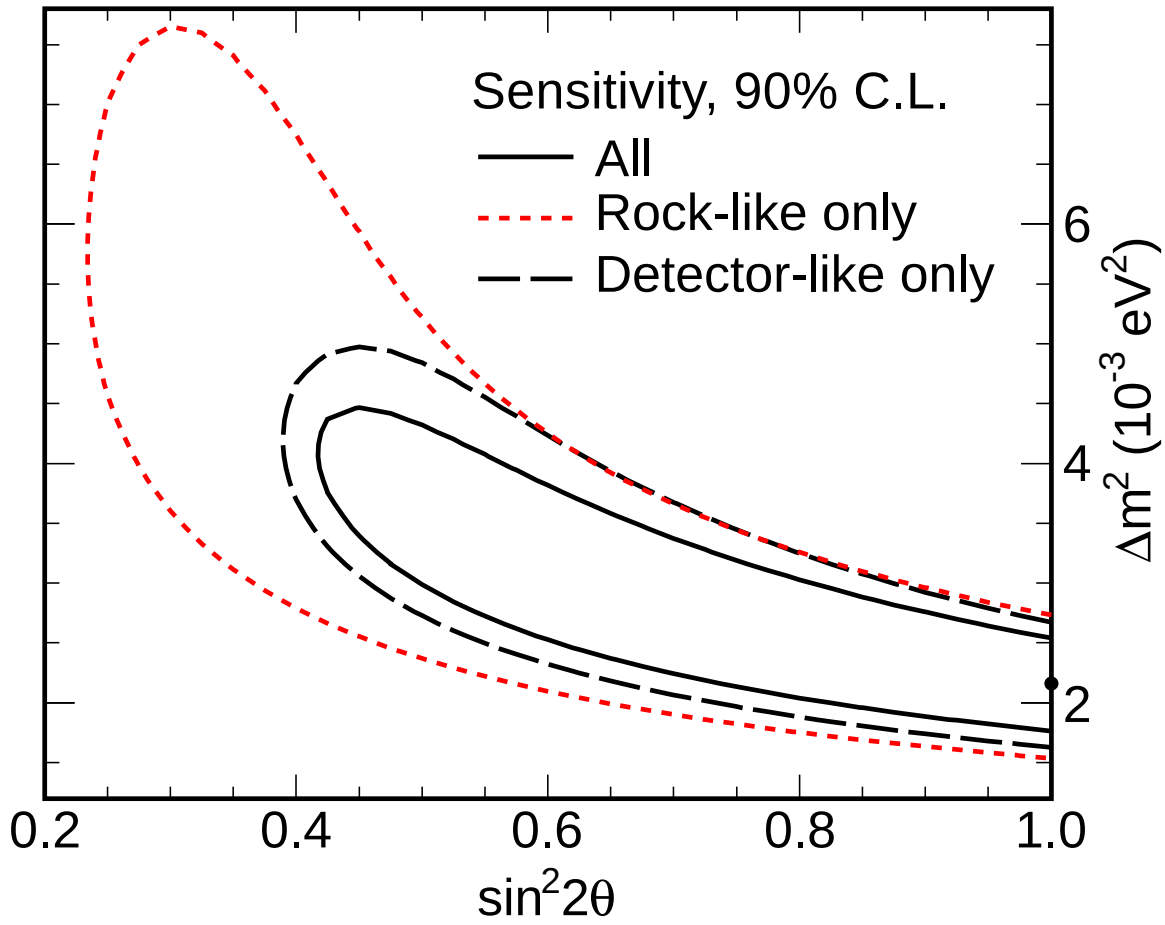

Figure 108: Sensitivity contours for partially reconstructed events with subcontours for the rock-like and detector-like samples alone, evaluated at partially reconstructed event best fit point.

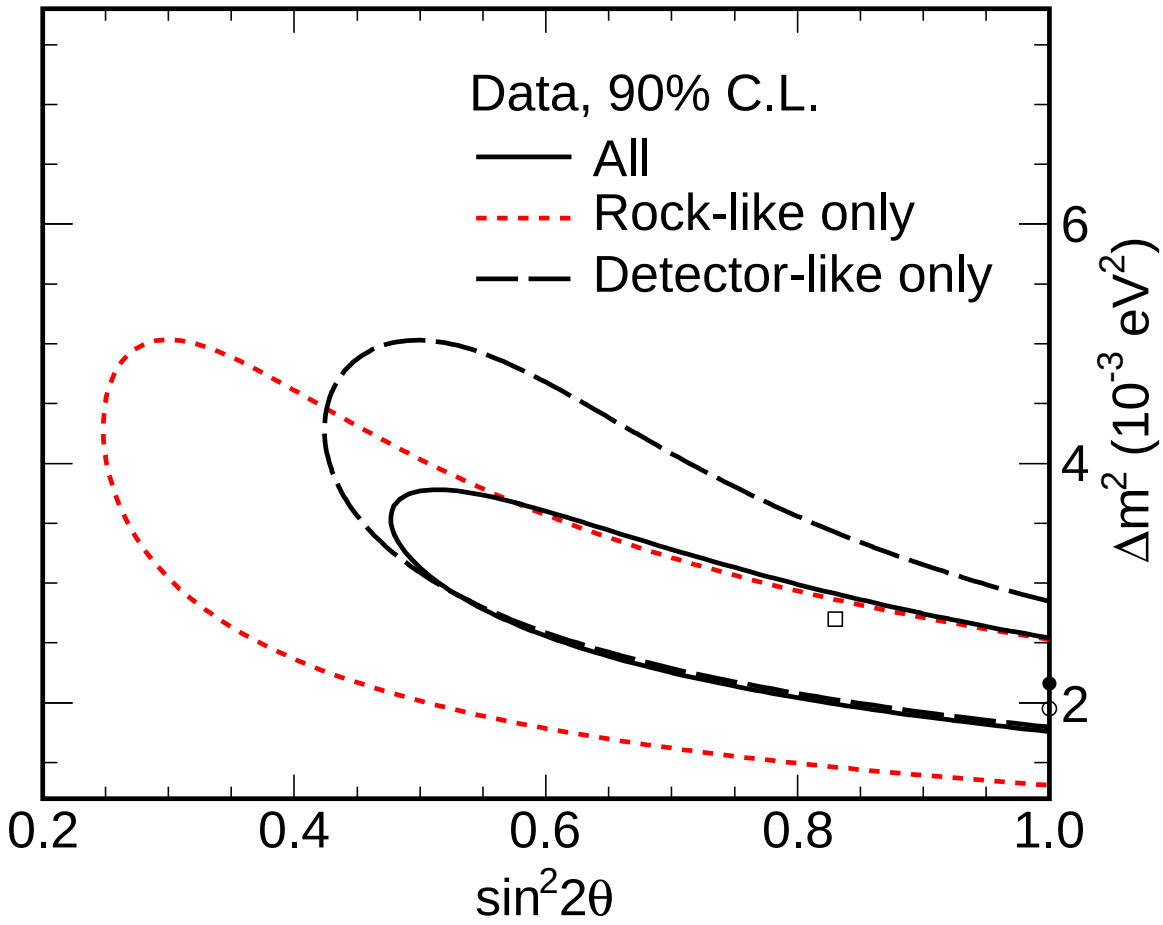

Figure 109: Contours for partially reconstructed events with subcontours for the rock-like and detector-like samples alone. The best fit of detector-like events alone is shown as an open square, of rock-like events alone as an open circle and the overall best fit as a closed square. Note roughly equal contributions from the two subsamples, with the detector-like sample being somewhat more powerful, but the rock-like sample doing better than the sensitivity due to the best fit point being at the physical boundary.

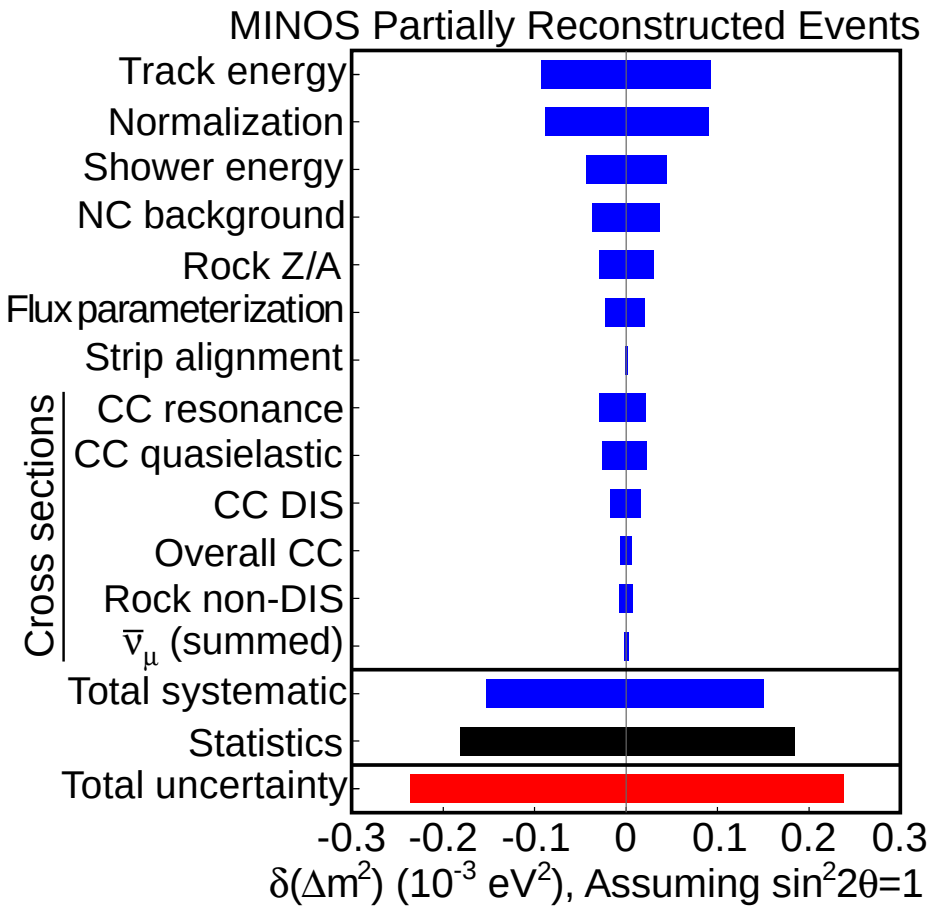

Figure 110: Systematic errors for partially reconstructed events. The total systematic is the output of the nuisance parameter fit with the statsitical error subtracted in quadrature, and then the unfit systematics added in quadrature. The total error is the output of the nuisance parameter fit wit hthe unfit parameters added in quadrature.

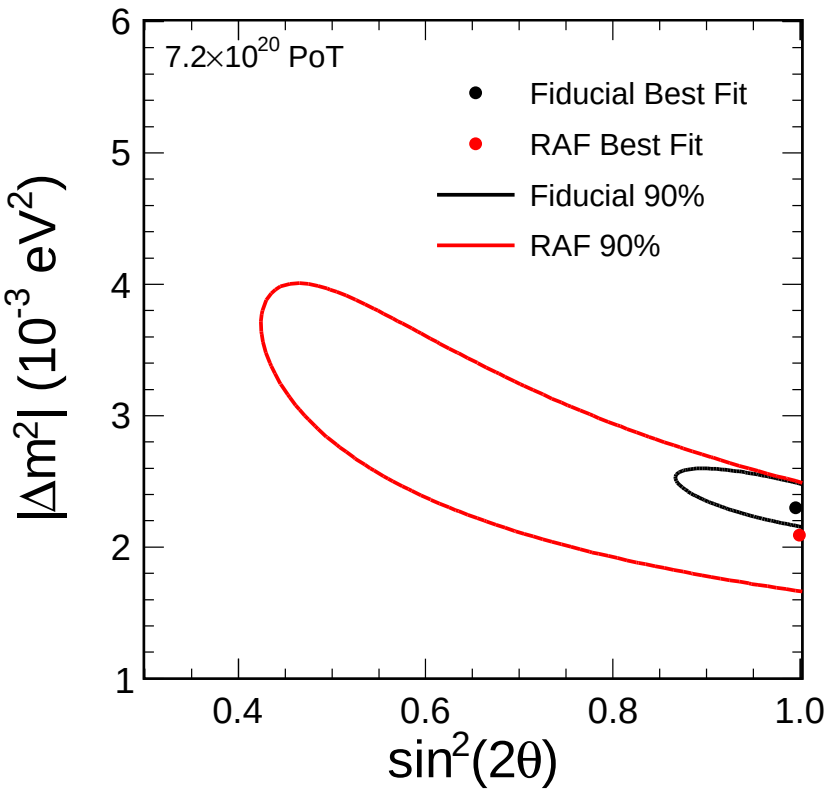

Figure 111: Contours for the oscillation fit; the statistical fit to the Rock and Anti-Fiducial (RAF) events and the statistical fit to the Fiducial events.

PRL Plots

These should be useful for proceedings

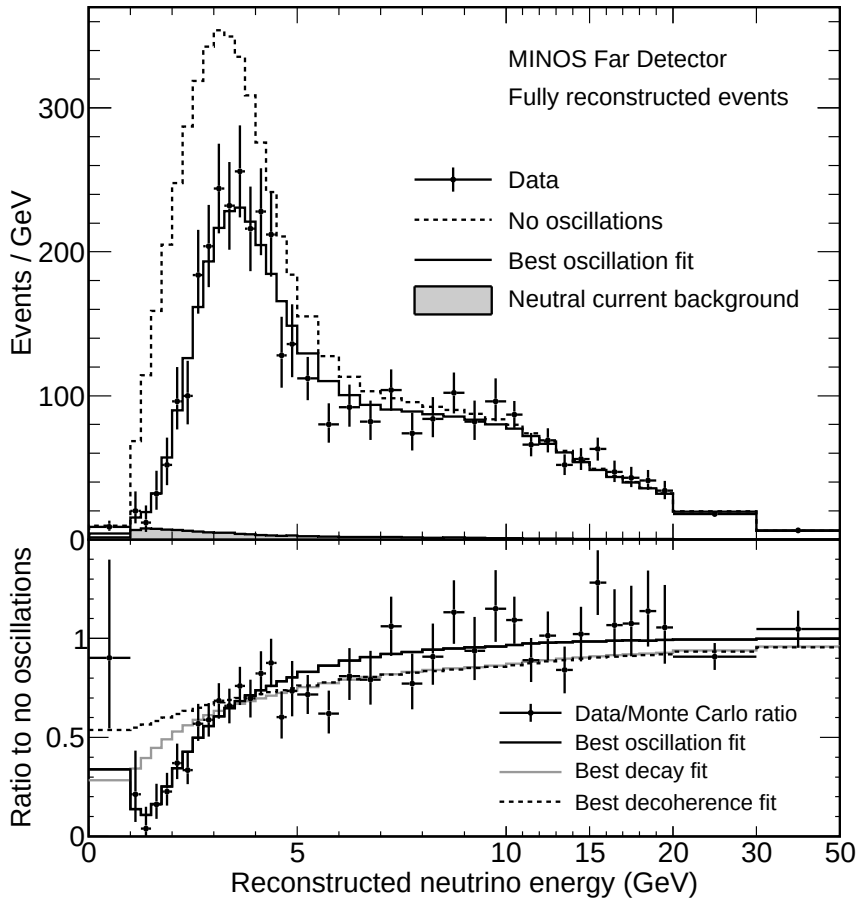

Figure 112: Top: The energy spectra of fully reconstructed events in the Far Detector classified as neutrino charged current interactions. The dashed histogram represents the spectrum predicted from measurements in the Near Detector assuming no oscillations, while the solid histogram reflects the best fit of the oscillation hypothesis (from the fit to all seven event categories). Bottom: The points with error bars are the background-subtracted ratios of data to the no-oscillation hypothesis. Lines show the best fits for the three tested scenarios: oscillations, decay and decoherence.

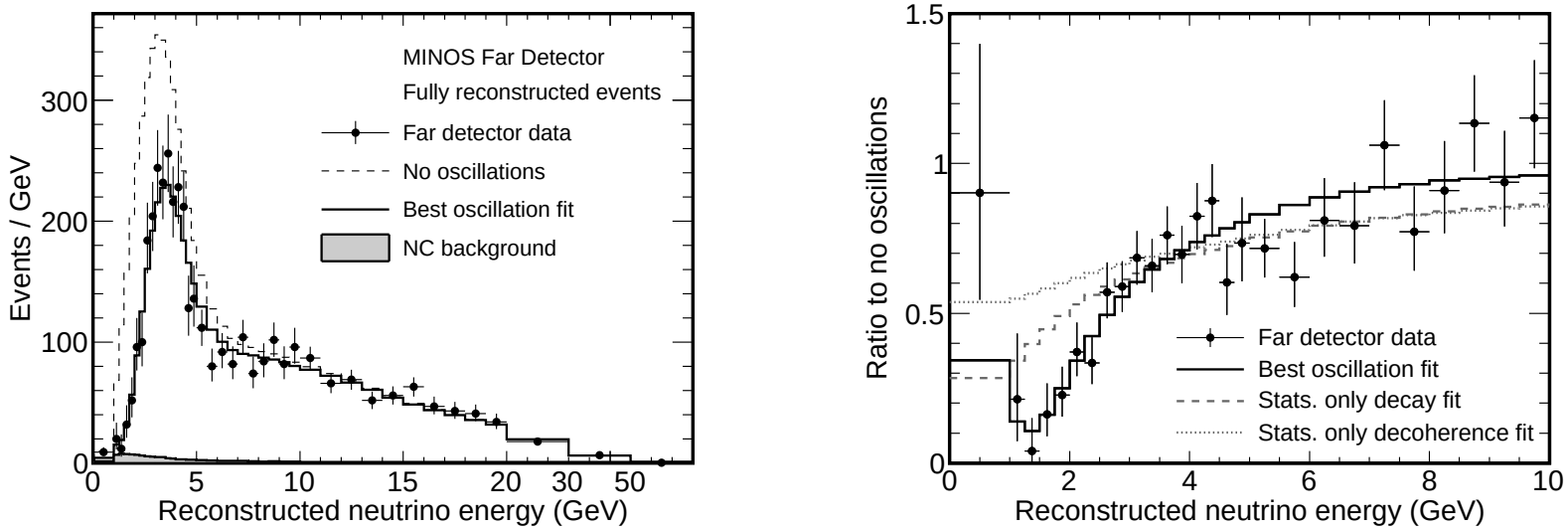

Figure 113: Separate FD energy spectra and ratio plots (the same as the previous slide, just not attached to each other).

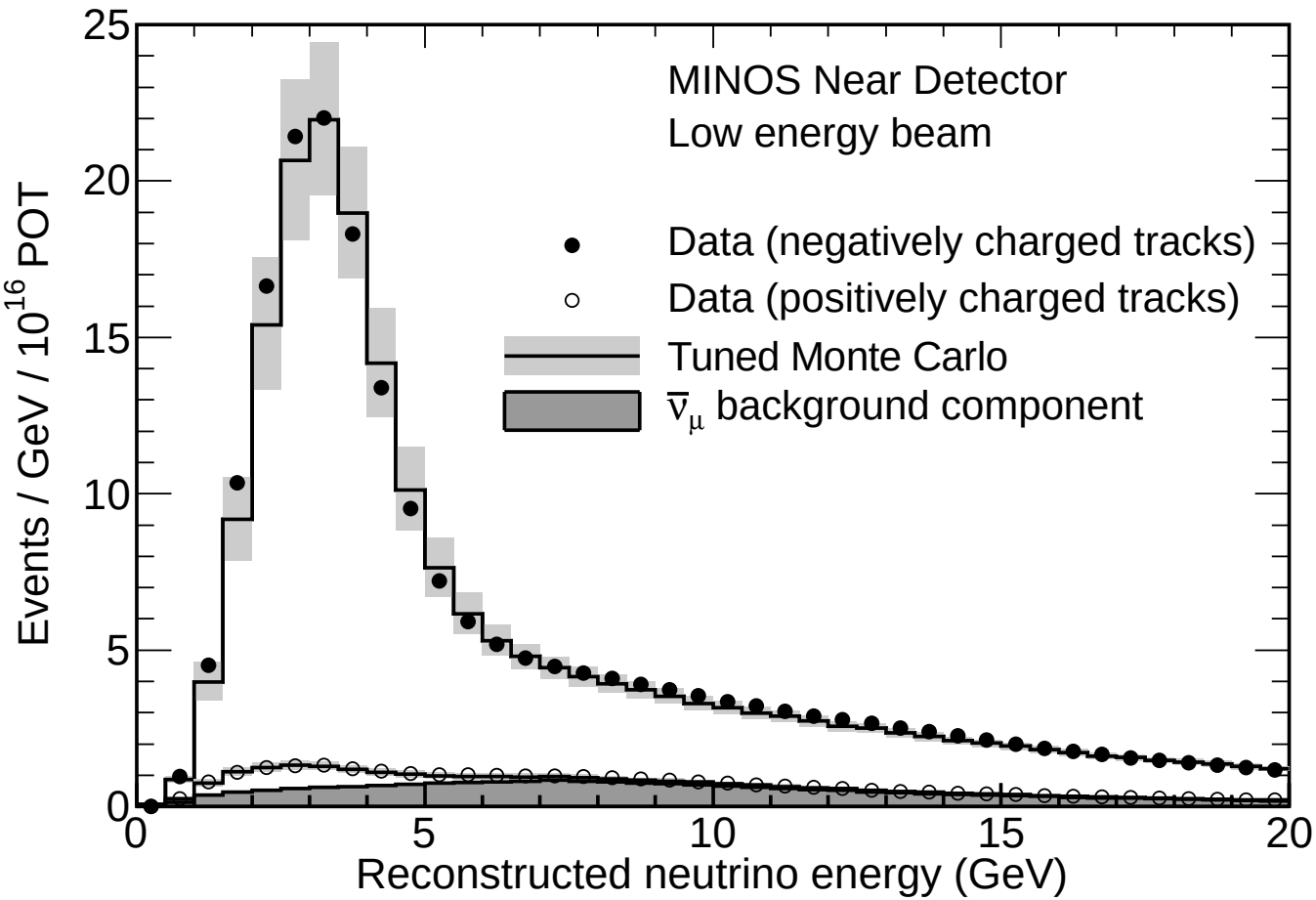

Figure 114: The energy spectra of fully reconstructed events in the Near Detector classified as charged current interactions. The solid and open circles repectively show the data reconstructed with negative or positive track charge from curvature. The solid lines show the tuned Monte Carlo with a shaded error band due to systematic uncertainties; the predicted spectrum for positive tracks lies directly behind the data points. The shaded area at the bottom represents the simulated antineutrino background.

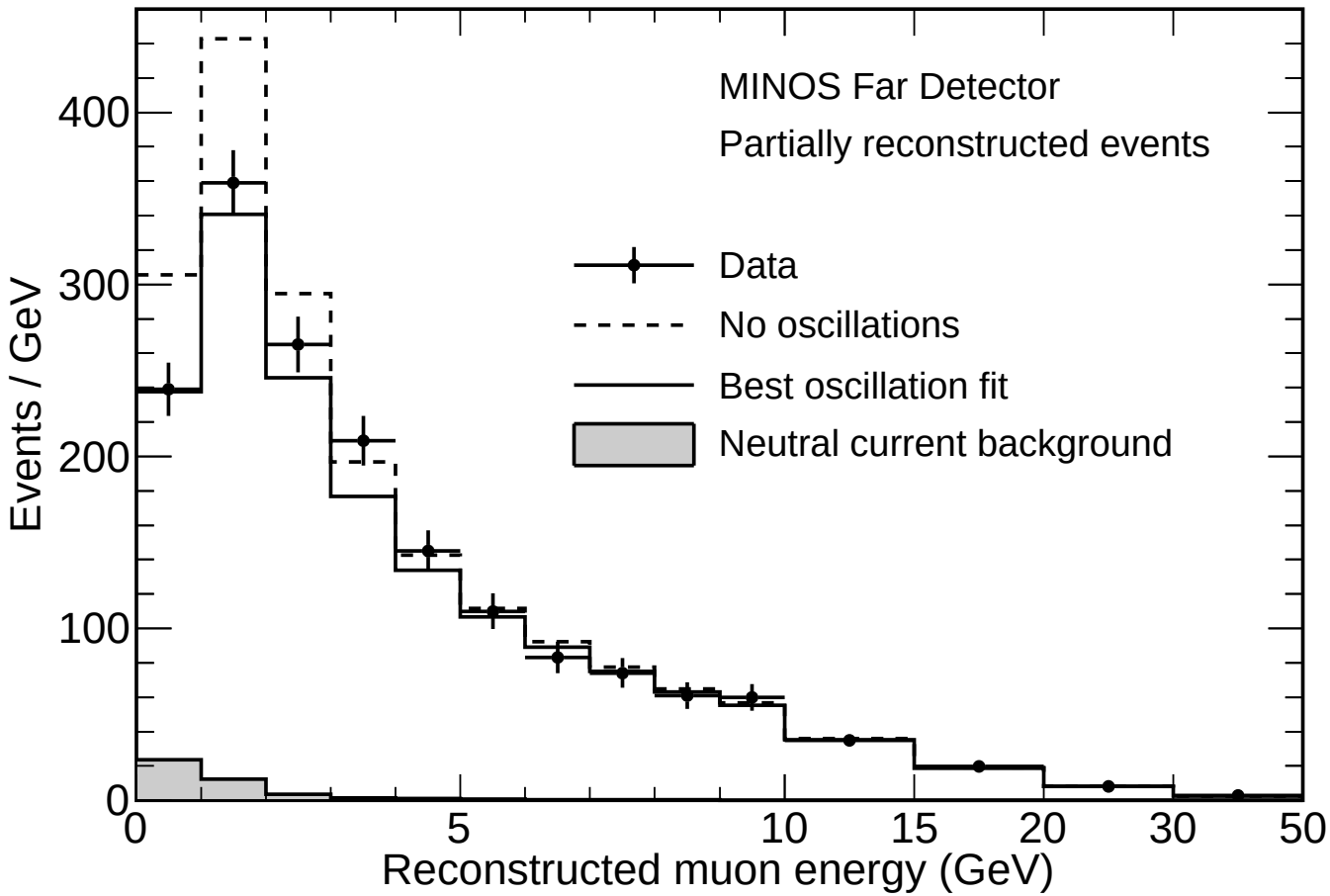

Figure 115: The energy spectra of partially reconstructed events originating in the surrounding rock or outer parts of the Far Detector.

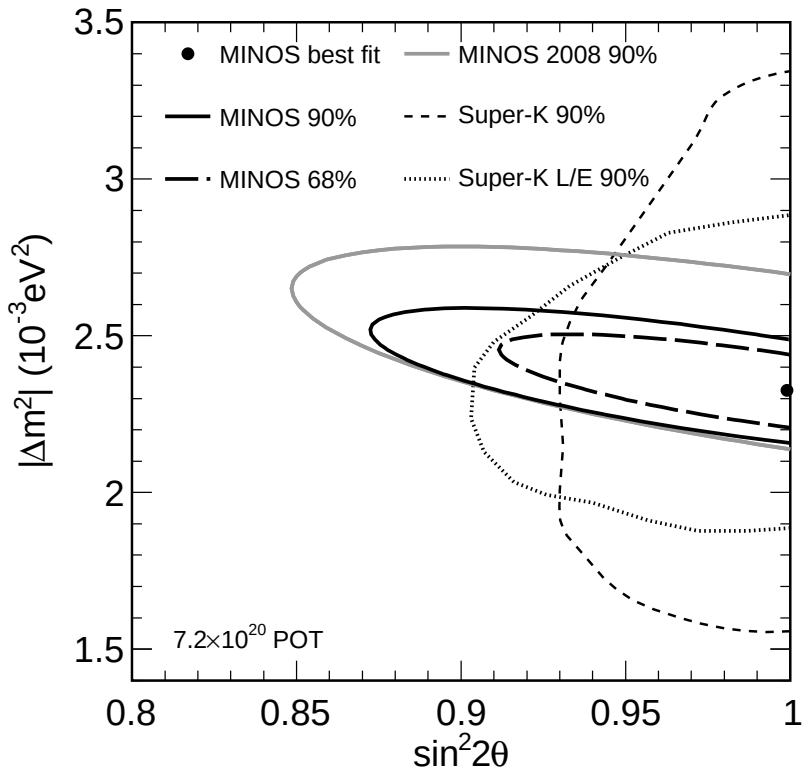

Figure 116: Likelihood contours of 68% and 90% confidence levels around the best fit value for the mass splitting $|\Delta m^2| = 2.32 \times 10^{-3}$ eV^2 and mixing angle $\sin^2(2\theta) = 1.0$. Also shown are contours from previous measurements and our earlier result.